
Comprehensive Pneumology Center / Institute of Lung Biology and Disease
Ludwig-Maximilians-Universität München and Helmholtz Zentrum München



Dissertation
for the awarding of a Doctor of Philosophy
(Ph.D.)
at the Medical Faculty of the
Ludwig-Maximilians-Universität München

Following fibroblast lineages in dermal development and scars

Submitted by :

Pushkar Ramesh

From :

Bengaluru, India

On :

12th November 2020

**Mit freundlicher Genehmigung der
Ludwig-Maximilians-Universität München**

First supervisor: *PD Dr. Claudia Staab-Weijnitz*

Second supervisor: *Dr. Yuval Rinkevich*

Dean: *Prof. Dr. med. dent. Reinhard Hickel*

Date of Oral defense: 08th February 2021



LUDWIG-
MAXIMILIANS-
UNIVERSITÄT
MÜNCHEN

Dean's Office
Medical Faculty



Affidavit

Ramesh, Pushkar

Surname, first name

Germany

Country

I hereby declare, that the submitted thesis entitled:

Following fibroblast lineages in dermal development and scars

is my own work. I have only used the sources indicated and have not made unauthorised use of services of a third party. Where the work of others has been quoted or reproduced, the source is always given.

I further declare that the submitted thesis or parts thereof have not been presented as part of an examination degree to any other university.

Munich, 12/02/2021

Place, date

Pushkar Ramesh

Signature doctoral candidate

Confirmation of congruency between printed and electronic version of the doctoral thesis



Ramesh, Pushkar

Surname, first name

Germany

Country

I hereby declare, that the submitted thesis entitled:

Following fibroblast lineages in dermal development and scars

is congruent with the printed version both in content and format.

Munich, 12/02/2021

Place, date

Pushkar Ramesh

Signature doctoral candidate

Table of contents

Affidavit	4
Confirmation of congruency	4
Table of contents	5
List of abbreviations	6
List of publications	7
Introductory summary	8
Skin and its architecture	8
Classical stages and diversity of wound repair	8
Dermal fibroblast heterogeneity	10
Visualizing fibroblast migration dynamics in dermal development	12
Visualizing fibroblast migration dynamics in wounding: scar development to molecular mechanism.....	13
Thesis summary.....	16
References	17
Publication I	21
Publication II	42
Appendix: Publication III and IV	68
Acknowledgements	88

List of abbreviations

PF	Papillary fibroblast
RF	Reticular fibroblast
DP	Dermal papilla
DWAT	Dermal white adipocyte tissue
ECM	Extra cellular matrix
PDGFR α	Platelet derived growth factor receptor alpha
DLK1	Delta like non-canonical notch ligand
LRIG1	Leucine-rich repeat protein 1
PRRX1	paired related homeobox 1
PPF	Prrx1 positive/past fibroblast
PNF	Prrx1 negative/naïve fibroblast
En1	Engrailed- 1
EPF	En1 positive/past fibroblast
ENF	En1 negative/naïve fibroblast
WPF	Wnt1 positive/past fibroblast
WNF	Wnt1 negative/naïve fibroblast
R26	Rosa26
2/3/4-D	Two/three/four Dimension
CRISPR	Clustered regularly interspaced short palindromic repeats
Cas9	CRISPR associated protein 9
AAV	Adeno associated virus
SCAD	Scar like tissue in a dish
DMSO	Dimethyl sulfoxide
sgRNA	Single guide ribonucleic acid

List of publications

- 2020 Jiang D, Christ S, Correa-Gallegos DC, **Ramesh P** et al. “Injury triggers fascia fibroblast collective cell migration to drive scar formation through N-cadherin”. *Nature Communications* **11**, 5653 (2020).
<https://doi.org/10.1038/s41467-020-19425-1> *joint first-author
- 2020 Fischer A, Koopmans T, **Ramesh P**, et al. “Post-surgical adhesions are triggered by calcium-dependent membrane bridges between mesothelial surfaces. *Nature Communications* **11**, 3068 (2020).
<https://doi.org/10.1038/s41467-020-16893-3>
- 2019 Correa-Gallegos D, Jiang D, Christ S, **Ramesh P** et al. “Patch repair of deep wounds by mobilized fascia”. *Nature* **576**, 287–292 (2019).
<https://doi.org/10.1038/s41586-019-1794-y>
- 2018 Jiang D, Correa-Gallegos D, Christ S, Stefanska A, Liu J, **Ramesh P**, et al.” Two succeeding fibroblastic lineages drive dermal development and the transition from regeneration to scarring”. *Nature Cell Biology* **20**, 422–431 (2018). <https://doi.org/10.1038/s41556-018-0073-8>
- 2018b **Ramesh P** Cover image “Volume 20 Issue 4, April 2018” *Nature Cell Biology* (2018) <https://www.nature.com/ncb/volumes/20/issues/4>

Introductory summary

Skin and its architecture

Skin is the largest organ of the human body. It is composed of three functionally distinct layers: epidermis, dermis and hypodermis. The thickness of these layers vary among species (e.g. mouse and human) and anatomical locations. For instance, palms and soles have thick skin compared to the rest of the body. The topmost layer, the epidermis, is considered to be a highly regenerative layer. Acute injuries limited to epidermis are quickly resolved via migration of keratinocytes. This is aided by immediate recruitment of innate immune cells and subsequent activation and proliferation of keratinocytes (Pastar et al., 2014). The next layer, the dermis, lies directly beneath the epidermis. It is subdivided into an upper papillary dermis and lower reticular dermis. Both layers contain functionally distinct resident fibroblasts such as papillary fibroblasts (PF), reticular fibroblasts (RF), dermal papilla (DP) and dermal white adipocyte tissue (DWAT). In addition, the dermis layer houses appendages and structures such as hair follicles, sweat glands, vascular and lymphatic networks (Atit et al., 2018). The innermost layer of the skin is the hypodermis or subcutaneous fascia layer. This layer connects the dermis to the skeletal muscles. It comprises fibroblasts, fat tissues, macrophages and loosely arranged collagen fibers. Functionally, this layer mainly provides mechanical cushioning and thermal insulation of the body (Driskell et al., 2014). Taken together, skin homeostasis is achieved by constant interaction between the layers and its components.

Classical stages and diversity of wound repair

Wound healing is a complex physiological process. It occurs in four distinct overlapping stages: inflammation, proliferation or epithelialization, maturation and remodeling (Gurtner et al., 2008). The repair process eventually leads to several outcomes ranging from perfect tissue regeneration to exuberant fibrotic scars. This diversity is dependent on the a) phylogeny, i.e. the specific taxon group in the animal kingdom, b) the stage of development at which injury occurred, the c) anatomical site where the injury occurred, and finally the depth of tissue injury (desJardins-Park et al., 2019).

In the context of wound repair among species/class (phylogeny), organisms such as axolotls, planarians, zebrafish, cnidarians and certain amphibians such as salamanders can functionally

regenerate tissues either fully or with minimal scar (in a scarless manner). In contrast to these regeneration-competent organisms, dermal wound healing in mice and humans focusses on quick sealing of breached skin as an external barrier. This is achieved by deposition of a dense plug of fibrous extracellular matrix (ECM) devoid of original primary and secondary dermal appendages. As an intermediate, mammals such as African spiny mice have shown to functionally regenerate the wounds to its original form. The validity of these conserved cellular and molecular mechanisms provides cues that govern regeneration mode of wound healing. Induction and revival of these molecular mechanisms in regeneration-incompetent organisms such as rat, mice and eventually humans plays a significant role in scar free wound healing, and is one of the pinnacle goals of regenerative medicine as a field (Blanchoud et al., 2018; Brant et al., 2019; Erickson and Echeverri, 2018; Maden and Varholick, 2020; Yates et al., 2012).

Wounds caused at a particular developmental stage/ontogeny predicate the repair outcome (Lo et al., 2012). This was first documented close to seven decades ago by Arthur Hess who identified an uncanny resemblance between fetal wound healing of guinea pigs compared to the regeneration-competent “primitive” organisms. He inflicted wounds in young and old fetuses and observed complete healing in less than 6 days (Hess, 1954). About 40 years ago, similar observations were made on 20-week old human fetuses by Ursula Rowlatt. In her experiments, limb amputations caused by amniotic constriction bands were completely devoid of inflammation, granulation tissues and necrotic material at amputation sites (Rowlatt, 1979). In the 1990s, a series of studies by Longaker, Lorenz and others have identified that transition from scarless wound healing to scarring happens after 24 weeks of gestation in humans and gestational days 16.5 to 18.5 in rats. Contrary to the previous thought that sterile, nutrient rich environment enables scarless healing, they proved that it is an intrinsic property of the fetal ECM and fibroblasts (Armstrong and Ferguson, 1995; Lo et al., 2012; Longaker et al., 1994; Lorenz et al., 1992).

The third factor influencing scarring is a combination of anatomical location, etiology/depth of the injury and demographics of an individual. Contrary to head, neck or back skin, wounds on the oral mucosa heal with minimal or no scar (Wong et al., 2009). Studies have shown that heterogeneity in wound healing potential is mainly due to the differences in angiogenesis, injury environment and reduced inflammation between anatomical sites (Boink et al., 2016; Iglesias-Bartolome et al.,

2018; Politis et al., 2016). Etiological studies using high frequency ultrasound analysis have shown that large and deep wounds are more susceptible to scarring. The critical depth for scarring develops if the injury spans for greater than 33.1% of total skin thickness (Dunkin et al., 2007). This indicates that surface injuries to epidermis, papillary dermis, and even partial reticular dermis can repair scarlessly. With demographics, young and darker skinned individuals have higher tendency of keloid and hypertrophic scars in response to deep skin injuries.

In conclusion, the repair process in most adult mammals or higher vertebrates mainly focusses on rapid restoration of wounds as an external barrier. This is often achieved by rapid deposition of ECM or in some cases pathological scars such as keloids and hypertrophic scars (Martin, 1997; Tripathi et al., 2020). Besides the psychological distress and aesthetic implications, scar management and treatments causes a huge financial burden. Despite the increasing number of anti-scarring treatments, medications in the US alone were estimated to be over \$12 billion per year. Chronic wounds in combination with diabetes, obesity, burns, surgical incisions and lacerations pose a substantial economic, clinical and social threat (Griffin et al., 2020; Jiang et al., 2018) . It is therefore essential to understand the biological mechanisms, characterize the dynamics and heterogeneity of cells involved in scar formation.

Dermal fibroblast heterogeneity

As described in the previous section, wound repair is a cell intrinsic process and independent of host microenvironment. Cell fate mapping in mice demonstrate the inherent differences in heterogeneity depends on the anatomical location of the body. In particular, fibroblasts in dorsal dermis originate from the somatic dermo-myotome, which is of mesoderm germ layer origin. Whereas, the fibroblasts in face are derived from neural crest and cephalic mesoderm. In contrast, fibroblasts in ventral dermis and limbs originate from lateral plate mesoderm (Atit et al., 2018; Griffin et al., 2020; Tran et al., 2010). In order to further characterize and understand the heterogeneity of fibroblasts, lineage tracing experiments were performed. Based on anatomical locations of such lineages, three studies are described below. (Driskell et al., 2013; Hu et al., 2018; Rinkevich et al., 2015)

Driskell et al described that heterogeneous fibroblast population arise from a multipotent mesenchymal cell population at E12.5 that expresses PDGFR α , delta like non-canonical Notch

ligand (DLK1) and Leucine-rich repeat protein 1 (LRIG1). Upon differentiation after E15-E16, it gives rise to varieties of subpopulations that differentially express the above markers to commit to either reticular (DLK+) or papillary (LGIG1) fibroblast progenitors, which carry more restricted developmental potential. These populations have the capacity to further differentiate into distinct dermal lineages during further stages of development (Driskell et al., 2014, 2013; Griffin et al., 2020).

Similar observations were made by Longaker, Lorenz and colleagues. They identified heterogeneous cell lineages that are primary contributors of scarring at various sites of injury. This includes, dorsal dermis (origin: dermo-myotome, somatic mesoderm), oral mucosa (origin: neural crest) and ventral dermis (origin: lateral plate mesoderm). In the context of ventral dermis, Hu et al., characterized fibroblast populations based on early embryonic expression of paired related homeobox 1 gene (*Prrx1*). Here, they identified that lineage with *Prrx1* past embryonic gene expression (termed PPFs) is the key contributor for scarring as opposed to the *Prrx1* negative fibroblasts (termed PNFs). This was inferred based on the chromosomal accessibility based on ATAC-seq. To further characterize these populations in the context of scarring, they performed genetic ablation studies of the PPF population and reported a diminished ECM deposition at the injury site (Griffin et al., 2020; Hu et al., 2018). In the context of dorsal dermis, Rinkevich et al. identified functionally distinct lineages using the transgenic mouse line *En1^{Cre}* marked by *Engrailed-1*: *En1* gene expression in early embryonic cells. Using lineage tracing and transplantation studies, they identified fibroblasts with *En1* past expression (termed EPF) and its descendants as the primary contributors of scarring in dorsal skin. In contrast, the fibroblast without *En1* past expression (termed ENF) do not contribute to fibrotic scars (Atit et al., 2018; Griffin et al., 2020; Rinkevich et al., 2015). Analogous to the *Engrailed-1* lineage in dorsal dermis, Rinkevich and colleagues identified heterogeneous fibroblast lineages in neural crest populations in oral mucosa marked by *Wnt1* lineage past expressing cells. Using *Wnt1^{Cre}* transgenic line, Rinkevich and colleagues identified WPFs as a principal scar contributing lineage coexisting with the WNFs. Upon crossing *En1^{Cre}* and *Wnt1^{Cre}* populations with R26^{mTmG} transgenic mice, they isolated EPF and WPF populations based on GFP positivity. These cells were then reciprocally transplanted in oral and dorsal dermis. Subsequently upon wounding, oral dermis containing EPF led to scarring. Conversely, WPF in dorsal dermis were devoid of scars. This validates that scar

formation is cell intrinsic and independent of the host environment (desJardins-Park et al., 2018; Rinkevich et al., 2015).

From these studies, it is clear that from a developmental standpoint, there is a vast heterogeneity of fibroblast lineages. Albeit the morphological similarities in these lineages, they are functionally committed and confined to its respective anatomical locations.

Visualizing fibroblast migration dynamics in dermal development

Localized fibroblast lineages in various anatomical sites clearly contribute to the outcome of wounds. However, little is known about the role and migration dynamics of these lineages in the context of development. This may be due to the technical difficulties in embryo preparation, embryo culture, *in vivo* imaging, computational cell tracking and analysis. In **publication I**, we have established and employed a combination of recently developed state-of-the-art approaches to chart the embryonic EPF and ENF dynamics. These lineages are visualized by crossing $En1^{Cre}$ or $Wnt1^{Cre}$ to the $R26^{mTmG}$ (dual color) or $R26^{VT2/Gk3}$ (four color) transgenic fluorescent reporter mouse lines (Jiang et al., 2018; Rinkevich et al., 2015).

The advancement of fluorescent reporter mouse lines enables us to specifically label the cell / tissue of interest. However, until recently, visualization of these labelled tissues was classically examined on 2-D cell cultures or on histological slices. Cell localization, migration and trajectory studies in a live tissue, organ and organismal context require inspection of samples in along 3-D space and time. From a biological stand point, almost all vertebrates and invertebrates contain high amount of lipids and pigments. From a microscopy/imaging standpoint these substances lead to scattering and impede light penetration, excitation and detection of fluorophores from labelled tissues. Recent advancements in “tissue clearing” enable us to clear these lipids and pigments. As a result, this renders the tissues fully transparent while preserving the tissue morphology and cellular integrity. This can be achieved by applying relevant protocols summarized in Ueda et al., 2020 (Ueda et al., 2020). In **publication I**, we have used organic solvent based “modified 3-DISCO” clearing method described by Ali Ertürk and colleagues. Albeit the advantages of tissue clearing in rendering the tissue transparent, till date, it is important to note that “clearing protocols” can only be applied on fixed tissues. Therefore, EPF localization studies at different developmental

stages (E11.5 to E16.5) were visualized using “3-DISCO” cleared embryos (Ertürk et al., 2012; Jiang et al., 2018; Pan et al., 2016; Ueda et al., 2020).

To chart the migration dynamics of EPFs in dermal development, we performed 3-D time-lapse confocal imaging. Murine dermis at E12.5 embryo contains immature translucent dermis, devoid of strong pigments and secondary appendages. To ensure ideal conditions for live imaging, we equipped the imaging stage with an incubator system. This enables 3-D time-lapse imaging along with adequate *ex-ovo* culture conditions to detect the EPF cell movements (Jiang et al., 2018). To analyze the EPF migration dynamics in these 3-D time-lapse datasets, we performed 3-D cell tracking using ImageJ plugin Trackmate (Tinevez et al., 2017). Resulting 3-D coordinates with its corresponding time points data were analyzed using a custom built R script (Jiang et al., 2018).

In conclusion, above mentioned 3-D and 4-D imaging pipelines allows analysis of EPF and ENF trajectories at a high spatiotemporal and single-cell resolution. Lineage fate mapping studies allows visualization of a) dermal morphogenesis and b) lineage transition from regeneration (ENF predominant) to scar (EPF predominant) populations in developing embryos (Jiang et al., 2018).

Visualizing fibroblast migration dynamics in wounding: scar development to molecular mechanism

The fascia system and its contribution to scar formation in the dermis largely remain unexplored. As opposed to superficial wounds, scar formation in mammals is a consequence of large-deep wounds. Previously, etiological studies by Dunkin et al. demonstrate that scarring is formed if the injury spans for > 33% of total tissue thickness (Dunkin et al., 2007). This corresponds to the injuries that spans beyond deep reticular dermis and subcutaneous fascia. Our recent findings in **publication III** suggest that scarring is caused by perturbation of subcutaneous fascia. Dermal injuries that extends to the fascia layer leads to quick steering of provisional fascial scar matrix that seal large-open wounds (Correa-Gallegos et al., 2019). However, fascial EPF dynamics and key molecular players that drive the fascial mobilization remain unknown.

As a follow-up study in **publication II**, we aimed to chart fascial EPF migration dynamics and a molecular mechanism that drives fascia mobilization (Jiang et al., 2020). To summarize, in this paper we:

- a) Developed a relevant *ex-situ* model that emulates fascial EPF dynamics in the context of scar development.
- b) Charted live fascial EPF migration dynamics and entire scar development in dermal explants using multiphoton microscopy, single cell tracking, and trajectory analysis.
- c) Screened and identified key adhesion molecules involved in scar development.
- d) Validated the role of promising adhesion molecule in murine *in-vivo* models and human explants using CRISPR-Cas9 mediated knockout and adeno associated viral (AAV) approaches.

Previously explored dermal explant models used to study wound healing were performed in a) non-native environment or b) devoid of one or more components of dermis. Further, due to the unknown role of fascia in scar formation, application of these models were limited to study epidermal wound closure (Abd et al., 2016; Li et al., 2020). In order to visualize the entire scarring process, we developed a novel dermal *ex-vivo* model termed “scar-like tissue in a dish” (termed SCAD). SCAD assay was performed by excising 2mm full thickness skin (inclusive of epidermis, dermis, and subcutaneous fascia) and cultured in a serum supplemented DMSO media with fascia facing upwards. Using our $En1^{Cre}$ combined with previously described fluorescent reporter, we visualized the entire scarring process using a multiphoton microscope. These modalities enable high tissue penetration of light which are achieved using infrared lasers (wavelength: 800-1300nm). This allows excitation and detection of deep tissue fluorophores at a single cell resolution with minimal light scattering. Further, multiphoton modality offers optimal long term imaging due to low phototoxicity and photobleaching. In dermis, this ranges from fascia (top imaging plane) up to the reticular or papillary dermis (bottom imaging plane). To emulate ideal tissue culture conditions, we equipped imaging stage with a suitable incubator (37°C, 5% CO₂). 3-D time-lapse data indicate that fascial EPFs within 24 hours form multiple small clusters of 4-6 cell aggregates and start invading the inner circle. By day 3, these aggregates coalesce into 4-5 distinct EPF swarms. Finally by day 4 and 5, these swarms eventually merge into one or two large swarms consisting of hundreds of fibroblasts that migrate collectively and uniformly, to the epidermis.

Collective migrations of EPFs clearly indicate that cell swarming is caused by upregulation of adhesion molecules between adjacent fibroblastic cells. Upon screening an array of cell adhesion

molecules, at early and late stage SCADs, we identified that swarms are driven by N-cadherin upregulation. We further observed that SCADs devoid of fascia and SCADs isolated from non-scar forming tissues (e.g. oral mucosa) do not generate cell swarms and lack upregulation of N-cadherin (Jiang et al., 2020).

In order to validate the above findings, we generated AAVs expressing CRISPR-N-cadherin-sgRNA constructs to specifically knockdown N-cadherin junctions. Injection of these viral particles to fascia of full body Cas9 expressing (R26^{Cas9}) mice showed significant reduction in scar area. We further validated the role of N-cadherin and scarring in human SCAD models generated from various anatomical locations. Results showed similar patterns of expression from our murine SCAD and *in-vivo* experiments (Jiang et al., 2020).

In conclusion, considering our recent findings of the involvement of fascia in scar formation, we developed an *ex-vivo* SCAD model to study the entire process of scar development. Inclusion of all the layers of murine dermis (epidermis, reticular and papillary dermis, *panniculus carnosus* and subcutaneous fascia) aided in generation of *bona fide* murine scars. Using this model in combination with novel imaging and image-analysis pipelines, we charted the full spectrum of EPF migration and scarring dynamics. Next, we aimed to identify cell-cell junction, N-Cadherin, in fascia that orchestrated scarring process in mammals. Using N-Cadherin targeted CRISPR knockout in combination with viral delivery approaches, we validated the role of N-Cadherin as a primary adhesion molecule involved in fascia mobilization. Finally, we demonstrated the relevance of above model in human dermal explants and *in-vivo* murine scars (Jiang et al., 2020).

Thesis summary

Fibroblast heterogeneity studies have shown that it vastly influences the outcome of wound repair (Griffin et al., 2020; Rinkevich et al., 2015). We aimed to characterize the origins of these heterogeneous populations in **publication I**. Here we have shown that during dermal development there is an inherent inversion of fibroblast populations from abundant regenerative fibroblasts (ENFs) at early fetal stages of development, to abundant scar-producing fibroblasts (EPFs) during perinatal and adult life. Using novel imaging and analysis approaches, we have charted the dermal maturation dynamics of EPFs during the transition from scar-less (E12) to scarring stages (E16.5) of development. We then followed up on the role of scar-forming fibroblasts in postnatal and adult stages. In **publication III**, we identified the subcutaneous fascia as the main anatomical contributor of scars upon deep skin injury. Next, we followed the role of fascial scar producing cells, EPFs, and its contribution to scar formation in **publication II**. Here, we developed a relevant *ex-vivo* model called “scar like tissue in a dish”- termed SCAD. We show that scars on SCADs emulate the *bona fide in-vivo* scar phenotype. Using this model, we visualize and chart live migration dynamics of EPFs at all stages of scar development. Further, using antibody screening and CRISPR-Cas9 based genetic approaches, we identified that N-Cadherin is the adhesion molecular that orchestrates EPF and fascial response to scarring. Finally, to check the clinical relevance, we validated our N-cadherin mechanistic findings in human skin biopsies from various anatomical locations. These findings provide a range of therapeutic avenues in modulating subcutaneous fascial response and prevention of pathological scars.

References

- Abd, E., Yousuf, S.A., Pastore, M.N., Telaprolu, K., Mohammed, Y.H., Namjoshi, S., Grice, J.E., and Roberts, M.S. (2016). Skin models for the testing of transdermal drugs (Dove Press).
- Armstrong, J.R., and Ferguson, M.W.J. (1995). Ontogeny of the Skin and the Transition from Scar-Free to Scarring Phenotype during Wound Healing in the Pouch Young of a Marsupial, *Monodelphis domestica*. *Dev. Biol.* *169*, 242–260.
- Atit, R., Thulabandu, V., and Chen, D. (2018). Dermal fibroblast in cutaneous development and healing. *Wiley Interdiscip. Rev. Dev. Biol.* *7*.
- Blanchoud, S., Rinkevich, B., and Wilson, M.J. (2018). Whole-Body Regeneration in the Colonial Tunicate *Botrylloides leachii*. *Results Probl. Cell Differ.* *65*, 337–355.
- Boink, M.A., van den Broek, L.J., Roffel, S., Nazmi, K., Bolscher, J.G.M., Gefen, A., Veerman, E.C.I., and Gibbs, S. (2016). Different wound healing properties of dermis, adipose, and gingiva mesenchymal stromal cells. *Wound Repair Regen. Off. Publ. Wound Heal. Soc. Eur. Tissue Repair Soc.* *24*, 100–109.
- Brant, J.O., Boatwright, J.L., Davenport, R., Sandoval, A.G.W., Maden, M., and Barbazuk, W.B. (2019). Comparative transcriptomic analysis of dermal wound healing reveals de novo skeletal muscle regeneration in *Acomys cahirinus*. *PLOS ONE* *14*, e0216228.
- Correa-Gallegos, D., Jiang, D., Christ, S., Ramesh, P., Ye, H., Wannemacher, J., Kalgudde Gopal, S., Yu, Q., Aichler, M., Walch, A., et al. (2019). Patch repair of deep wounds by mobilized fascia. *Nature* *576*, 287–292.
- Driskell, R., Jahoda, C.A.B., Chuong, C.-M., Watt, F., and Horsley, V. (2014). Defining dermal adipose tissue. *Exp. Dermatol.* *23*, 629–631.
- Driskell, R.R., Lichtenberger, B.M., Hoste, E., Kretzschmar, K., Simons, B.D., Charalambous, M., Ferron, S.R., Herault, Y., Pavlovic, G., Ferguson-Smith, A.C., et al. (2013). Distinct fibroblast lineages determine dermal architecture in skin development and repair. *Nature* *504*, 277–281.
- Dunkin, C., Pleat, J., Gillespie, P., Tyler, M., Roberts, A., and McGrouther, D. (2007). Scarring Occurs at a Critical Depth of Skin Injury: Precise Measurement in a Graduated Dermal Scratch in Human Volunteers. *Plast. Reconstr. Surg.* *119*, 1722–1732.
- Erickson, J.R., and Echeverri, K. (2018). Learning from regeneration research organisms: The circuitous road to scar free wound healing. *Dev. Biol.* *433*, 144–154.

- Ertürk, A., Becker, K., Jährling, N., Mauch, C.P., Hojer, C.D., Egen, J.G., Hellal, F., Bradke, F., Sheng, M., and Dodt, H.-U. (2012). Three-dimensional imaging of solvent-cleared organs using 3DISCO. *Nat. Protoc.* 7, 1983–1995.
- Griffin, M.F., desJardins-Park, H.E., Mascharak, S., Borrelli, M.R., and Longaker, M.T. (2020). Understanding the impact of fibroblast heterogeneity on skin fibrosis. *Dis. Model. Mech.* 13.
- Gurtner, G.C., Werner, S., Barrandon, Y., and Longaker, M.T. (2008). Wound repair and regeneration. *Nature* 453, 314–321.
- Hess, A. (1954). Reactions of mammalian fetal tissues to injury. II. Skin. *Anat. Rec.* 119, 435–447.
- Hu, M.S., Leavitt, T., Garcia, J.T., Ransom, R.C., Litzenburger, U.M., Walmsley, G.G., Marshall, C.D., Moore, A.L., Mascharak, S., Chan, C.K.F., et al. (2018). Abstract 43: Embryonic Expression of Prrx1 Identifies the Fibroblast Responsible for Scarring in the Mouse Ventral Dermis. *Plast. Reconstr. Surg. Glob. Open* 6.
- Iglesias-Bartolome, R., Uchiyama, A., Molinolo, A.A., Abusleme, L., Brooks, S.R., Callejas-Valera, J.L., Edwards, D., Doci, C., Asselin-Labat, M.-L., Onaitis, M.W., et al. (2018). Transcriptional signature primes human oral mucosa for rapid wound healing. *Sci. Transl. Med.* 10.
- Jiang, D., Correa-Gallegos, D., Christ, S., Stefanska, A., Liu, J., Ramesh, P., Rajendran, V., De Santis, M.M., Wagner, D.E., and Rinkevich, Y. (2018). Two succeeding fibroblastic lineages drive dermal development and the transition from regeneration to scarring. *Nat. Cell Biol.* 20, 422–431.
- Jiang, D., Christ, S., Correa-Gallegos, D., Ramesh, P., Kalgudde Gopal, S., Wannemacher, J., Mayr, C.H., Lupperger, V., Yu, Q., Ye, H., et al. (2020). Injury triggers fascia fibroblast collective cell migration to drive scar formation through N-cadherin. *Nat. Commun.* 11, 5653.
- Li, J., Wang, J., Wang, Z., Xia, Y., Zhou, M., Zhong, A., and Sun, J. (2020). Experimental models for cutaneous hypertrophic scar research. *Wound Repair Regen.* 28, 126–144.
- Lo, D.D., Zimmermann, A.S., Nauta, A., Longaker, M.T., and Lorenz, H.P. (2012). Scarless fetal skin wound healing update. *Birth Defects Res. Part C Embryo Today Rev.* 96, 237–247.
- Longaker, M.T., Whitby, D.J., Ferguson, M.W., Lorenz, H.P., Harrison, M.R., and Adzick, N.S. (1994). Adult skin wounds in the fetal environment heal with scar formation. *Ann. Surg.* 219, 65–72.
- Lorenz, H.P., Longaker, M.T., Perkocha, L.A., Jennings, R.W., Harrison, M.R., and Adzick, N.S. (1992). Scarless wound repair: a human fetal skin model. *Development* 114, 253–259.

- Maden, M., and Varholick, J.A. (2020). Model systems for regeneration: the spiny mouse, *Acomys cahirinus*. *Development* *147*.
- Martin, P. (1997). Wound Healing--Aiming for Perfect Skin Regeneration. *Science* *276*, 75–81.
- Pan, C., Cai, R., Quacquarelli, F.P., Ghasemigharagoz, A., Loubopoulos, A., Matryba, P., Plesnila, N., Dichgans, M., Hellal, F., and Ertürk, A. (2016). Shrinkage-mediated imaging of entire organs and organisms using uDISCO. *Nat. Methods* *13*, 859–867.
- desJardins-Park, H.E., Foster, D.S., and Longaker, M.T. (2018). Fibroblasts and wound healing: an update. *Regen. Med.* *13*, 491–495.
- desJardins-Park, H.E., Mascharak, S., Chinta, M.S., Wan, D.C., and Longaker, M.T. (2019). The Spectrum of Scarring in Craniofacial Wound Repair. *Front. Physiol.* *10*.
- Pastar, I., Stojadinovic, O., Yin, N.C., Ramirez, H., Nusbaum, A.G., Sawaya, A., Patel, S.B., Khalid, L., Isseroff, R.R., and Tomic-Canic, M. (2014). Epithelialization in Wound Healing: A Comprehensive Review. *Adv. Wound Care* *3*, 445–464.
- Politis, C., Schoenaers, J., Jacobs, R., and Agbaje, J.O. (2016). Wound Healing Problems in the Mouth. *Front. Physiol.* *7*.
- Rinkevich, Y., Walmsley, G.G., Hu, M.S., Maan, Z.N., Newman, A.M., Drukker, M., Januszkyk, M., Krampitz, G.W., Gurtner, G.C., Lorenz, H.P., et al. (2015). Identification and isolation of a dermal lineage with intrinsic fibrogenic potential. *Science* *348*, aaa2151.
- Rowlatt, U. (1979). Intrauterine wound healing in a 20 week human fetus. *Virchows Arch. A Pathol. Anat. Histol.* *381*, 353–361.
- Tinevez, J.-Y., Perry, N., Schindelin, J., Hoopes, G.M., Reynolds, G.D., Laplantine, E., Bednarek, S.Y., Shorte, S.L., and Eliceiri, K.W. (2017). TrackMate: An open and extensible platform for single-particle tracking. *Methods* *115*, 80–90.
- Tran, T.H., Jarrell, A., Zentner, G.E., Welsh, A., Brownell, I., Scacheri, P.C., and Atit, R. (2010). Role of canonical Wnt signaling/ β -catenin via Dermo1 in cranial dermal cell development. *Dev. Camb. Engl.* *137*, 3973–3984.
- Tripathi, S., Soni, K., Agrawal, P., Gour, V., Mondal, R., and Soni, V. (2020). Hypertrophic scars and keloids: a review and current treatment modalities. *Biomed. Dermatol.* *4*, 11.
- Ueda, H.R., Ertürk, A., Chung, K., Gradinaru, V., Chédotal, A., Tomancak, P., and Keller, P.J. (2020). Tissue clearing and its applications in neuroscience. *Nat. Rev. Neurosci.* *21*, 61–79.

Wong, J.W., Gallant-Behm, C., Wiebe, C., Mak, K., Hart, D.A., Larjava, H., and Häkkinen, L. (2009). Wound healing in oral mucosa results in reduced scar formation as compared with skin: evidence from the red Duroc pig model and humans. *Wound Repair Regen. Off. Publ. Wound Heal. Soc. Eur. Tissue Repair Soc.* *17*, 717–729.

Yates, C.C., Hebda, P., and Wells, A. (2012). Skin wound healing and scarring: fetal wounds and regenerative restitution. *Birth Defects Res. Part C Embryo Today Rev.* *96*, 325–333.

Publication I

Jiang D, Correa-Gallegos D, Christ S, Stefanska A, Liu J, **Ramesh P**, Rajendran V, De Santis MM, Wagner DE, Rinkevich Y. Two succeeding fibroblastic lineages drive dermal development and the transition from regeneration to scarring. *Nature Cell Biology* **20**, 422–431 (2018). <https://doi.org/10.1038/s41556-018-0073-8>

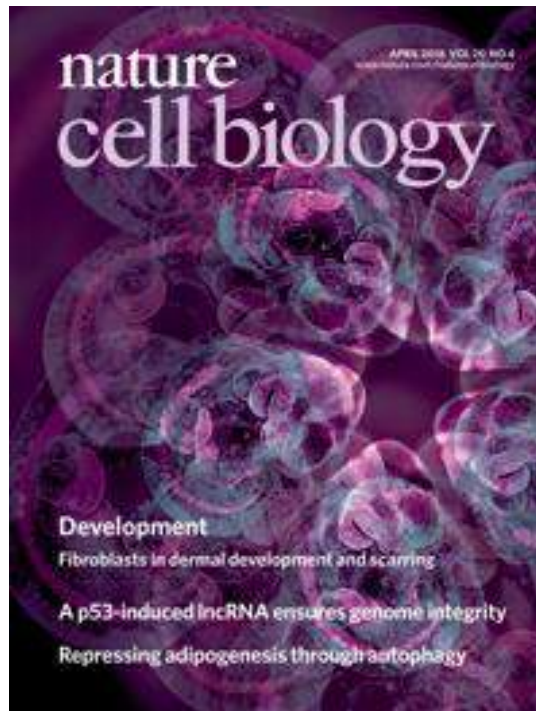
In this work, my contributions include:

Establishing relevant imaging modalities and analysis pipelines to chart the embryonic EPF and ENF dynamics. This was performed by isolating embryos followed by a) “3-DISCO” embryo clearing, 3-D confocal imaging, b) 4-D confocal imaging followed by computational cell tracking and image analysis.

I further provided relevant texts and figures for the manuscript along with the cover image for *Nature Cell Biology*- April 2018 issue.

In particular:

- a) Figure 2 f, f' and f'': Embryo isolation, tissue clearing and 3D confocal imaging
- b) Figure 3 a, b, c, d, e and f: Live embryo imaging, Computational cell tracking , generation of R script and 3D interactive graphs for data visualization
- c) Supplementary figure 4:live embryo imaging
- d) *Nature Cell Biology* cover image: <https://www.nature.com/ncb/volumes/20/issues/4>



Two succeeding fibroblastic lineages drive dermal development and the transition from regeneration to scarring

Dongsheng Jiang^{1,5}, Donovan Correa-Gallegos^{1,5}, Simon Christ^{1,5}, Ania Stefanska¹, Juan Liu¹, Pushkar Ramesh¹, Vijayanand Rajendran¹, Martina M. De Santis^{1,2,3}, Darcy E. Wagner^{1,2,3,4} and Yuval Rinkevich^{1,4*}

During fetal development, mammalian back-skin undergoes a natural transition in response to injury, from scarless regeneration to skin scarring. Here, we characterize dermal morphogenesis and follow two distinct embryonic fibroblast lineages, based on their history of expression of the engrailed 1 gene. We use single-cell fate-mapping, live three dimensional confocal imaging and in silico analysis coupled with immunolabelling to reveal unanticipated structural and regional complexity and dynamics within the dermis. We show that dermal development and regeneration are driven by engrailed 1-history-naive fibroblasts, whose numbers subsequently decline. Conversely, engrailed 1-history-positive fibroblasts possess scarring abilities at this early stage and their expansion later on drives scar emergence. The transition can be reversed, locally, by transplanting engrailed 1-naive cells. Thus, fibroblastic lineage replacement couples the decline of regeneration with the emergence of scarring and creates potential clinical avenues to reduce scarring.

Skin develops in the fetus when dermal fibroblasts establish a porous, ‘basket-weave’ scaffold, providing the tensile strength and extensibility needed for the structural integrity and for protective and sensing functions. Injuries to the skin commonly lead to loss of these frameworks and replacement by scar tissues, which have greatly limited functions. Scar tissue is rarely observed in lower vertebrates, where the normal response to injury is a complete regeneration of the original dermal structure. However, mammals have evolved to heal with scar tissue and undergo a regeneration-to-scar phenotypic transition during fetal life^{1,2}. This transition has been documented in the back-skin of all mammalian embryos studied to date including humans^{3–7}.

Previous studies into the fetal commencement of scarring have focused on a multitude of environmental differences between early and late fetal stages, including inflammatory responses to injury, expressions of morphogenetic proteins, growth factors and extracellular matrix (ECM) components such as hyaluronic acid⁸. In the early 1990s, the influence of the environment on the commencement of scarring was addressed by performing fetal/adult heterochronic transplantations of back-skin tissues in sheep⁹. The study found that donor back-skin tissues respond to injury (scar/regenerate) independent of the host microenvironment or the developmental stage. Thus, the authors concluded that the determining factor (or factors) of the commencement of scarring is probably intrinsic to the transplanted back-skin graft, most likely its fibroblasts, the tissue’s primary secretors of the ECM^{9,10}.

More recently, we have discovered that functionally diverse lineages of fibroblasts coexist in the mouse back-skin and oral cavity¹¹. Embryonic cells that have expressed engrailed 1 (*En1*), termed *En1*-lineage-past fibroblasts (EPFs), are the primary contributors to

scarring in various models of pathological scars. Conversely, *En1*-lineage-naive fibroblasts (ENFs) do not participate in scar production. By transplanting adult ENFs or EPFs in different anatomical locations, we determined that the difference in the capacity of EPFs and ENFs to form a scar in vivo is cell intrinsic and permanent¹¹.

Here, we followed the fates of EPF and ENF progenitors. We used genetic fate-mapping approaches at single-cell and lineage levels, live three-dimensional (3D) confocal imaging of lineage-specific cellular migrations and immunolabelling coupled with in silico approaches to determine how the dermal structure in the back-skin develops. We find that ENFs form the sculptures of the dermal lattice and that their cell lineage declines during development, concurrent with a surge in EPF numbers that predisposes back-skin to scarring.

Results

ENFs are replaced by EPFs during back-skin development. The *En1* gene is expressed in a small subset of early embryonic cells and switched off permanently later in embryogenesis¹¹. To distinguish *En1*-expressing cells and to follow their fibroblastic descendants in the developing back-skin, we used a transgenic mouse system where *En1* expression drives genetic rearrangements (*En1*^{Cre}). Crossing *En1*^{Cre} with a reporter mouse system (*R26*^{mTmG}), generated offspring where the genetic rearrangement replaced membrane-bound tomato red protein (RFP) expression with membrane-bound green fluorescence protein (GFP) expression¹² (Fig. 1a). The permanent replacement of RFP with GFP in all descendant cells allowed purification schemes of EPFs and ENFs based on GFP⁺RFP⁻Lin⁻ and GFP⁻RFP⁺Lin⁻, respectively.

Thus, we performed flow cytometric analysis of EPFs and ENFs from the total fibroblast population (Lin⁻, see Methods) in early fetal

¹Comprehensive Pneumology Centre/Institute of Lung Biology and Disease, Helmholtz Zentrum München, Munich, Germany. ²Department of Experimental Medical Sciences, Lund University, Lund, Sweden. ³Wallenberg Centre for Molecular Medicine, Lund University, Lund, Sweden.

⁴Member of the German Centre for Lung Research (DZL), Munich, Germany. ⁵These authors contributed equally: Dongsheng Jiang, Donovan Correa-Gallegos and Simon Christ. *e-mail: yuval.rinkevich@helmholtz-muenchen.de

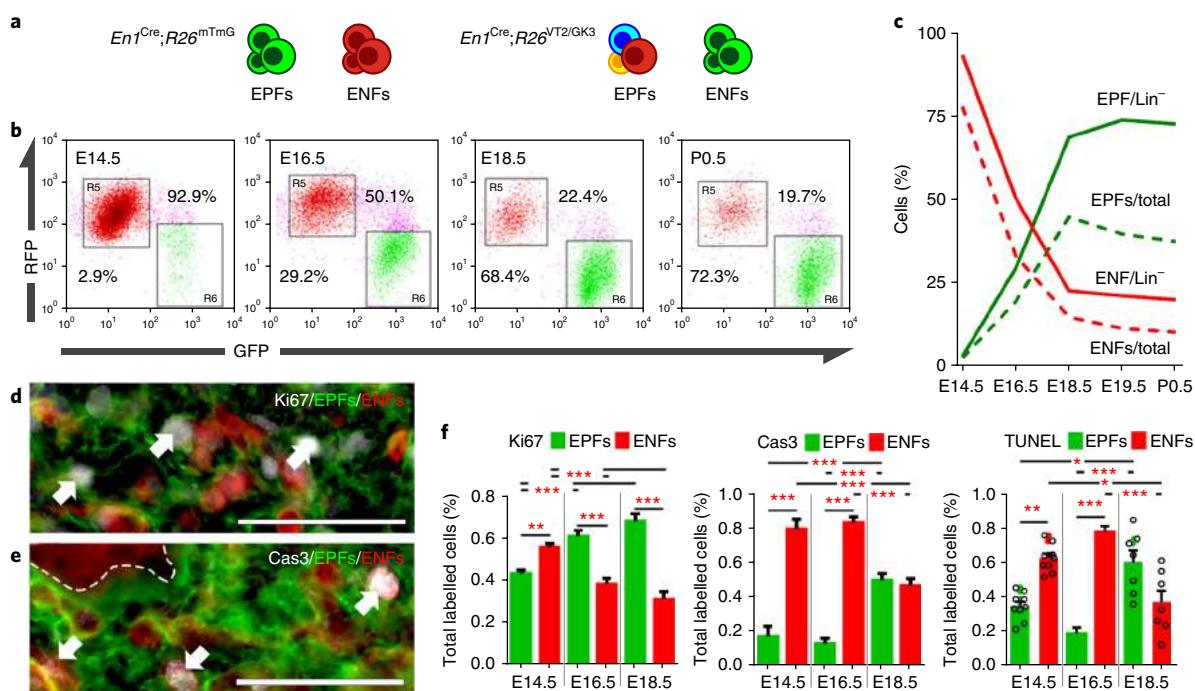


Fig. 1 | EPFs replace ENFs during mouse back-skin development. **a**, Genetic-labelling systems used ‘colour-coded’ cells. **b**, Representative flow cytometry plots of ENFs and EPFs from *En1^{Cre};R26^{mTmG}* embryos at different developmental stages. All Cre⁺ embryos (ranging from 3 to 6 embryos) from an entire litter were pooled together for a single analysis. GFP intensity (x axis) is plotted against RFP intensity (y axis). **c**, EPFs and ENFs percentages of Lin⁻ (solid lines) or total live cells (dashed lines). **d, e**, Representative immunofluorescence images of Ki67 (**d**) or Cas3 (**e**) in E18.5 *En1^{Cre};R26^{mTmG}* embryos; arrows indicate Ki67-positive or Cas3-positive cells, respectively. Scale bars, 50 μ m. **f**, EPFs and ENFs positive for Ki67, Cas3 or TUNEL. *n* = optical fields analysed from sections of three E14.5 embryos, two E16.5 embryos and one E18.5 embryo stained for Ki67 (*n* = 24, 28 and 16, respectively), Cas3 (*n* = 20, 15 and 14, respectively) and TUNEL (*n* = 9, 28 and 7, respectively). Mean \pm s.e.m. ANOVA, Tukey test, **P* < 0.05, ***P* < 0.01, ****P* < 0.001. Additional adjusted *P* values are listed in Supplementary Table 1.

back-skin. Dermal fibroblasts were mostly ENFs early on and their numbers declined slowly during subsequent development, followed by a steep decline between embryonic day 14.5 (E14.5) and E18.5 (~90% down to ~20%; Fig. 1b,c). The drop in ENF numbers was proportional to total dermal cells (including haematopoietic, endothelial and lymphatic) and to dermal fibroblasts alone (Lin⁻), indicating a clonal disadvantage to ENFs compared to all other dermal progenitors. Conversely, EPF numbers increased from ~2% of dermal cells at E14.5 (EPF/ENF ratio = 1/33) to ~72% at postnatal day 0 (P0) (EPF/ENF ratio = 4/1) (Fig. 1b,c) and in proportion to all other dermal progenitors (Fig. 1c). We then placed ENF and EPF lineages in relation to previously described adult mesenchymal cell populations based on the expression of surface markers (Supplementary Fig. 1). About 3% of Lin⁻ cells expressed fibro/adipogenic progenitor (FAP) markers^{13–15} (Lin⁻integrin α 7-Sca1⁺PDGFR α ⁺) that were enriched in EPFs (Supplementary Fig. 1c,f,g), whereas pericyte markers¹⁶ (Lin⁻CD146⁺) comprised 5% of total Lin⁻ cells and were enriched in ENFs (Supplementary Fig. 1d,f,g). Mesenchymal stem cell markers¹⁷ (Lin⁻CD29⁺CD105⁺) were abundant in both ENFs and EPFs (Supplementary Fig. 1e–g). Immunolabelling on *En1^{Cre};R26^{VT2/GK3}* (see Methods) neonate sections showed that adipocytes (fatty acid-binding protein 4 (FABP4)) or preadipocytes¹⁸ (proten delta homologue 1 (Dlk1) and stem cells antigen 1 (Sca1)) were more abundant in EPFs (Supplementary Fig. 2a–c). Similarly, the smooth muscle marker α -smooth muscle actin (α -SMA) was enriched in EPFs compared to ENFs (Supplementary Fig. 2d). Immunostaining of reticular and papillary dermis markers (Dlk1, tenascin-C (TNC) and CD26) showed that their expression was not exclusive to either lineage (Supplementary Fig. 2b,e,f), indicating that EPFs and ENFs do not preferentially allocate to either anatomical location.

To determine whether the decline in ENF numbers is due to programmed cell death or a decrease in proliferation, we performed TdT-mediated dUTP nick end labelling (TUNEL) staining and immunolabelling of cleaved caspase 3 (Cas3) and the proliferation marker Ki67 on sections of E14.5, E16.5 and E18.5 *En1^{Cre};R26^{mTmG}* embryos. ENFs underwent significantly more apoptosis than EPFs at E14.5 and E16.5 (Fig. 1e,f). Conversely, the number of proliferating EPFs steadily increased from E14.5 to E18.5, whereas ENF proliferation significantly decreased (Fig. 1d,f). Together, our results show that the decay in the ENF population is primarily due to a clonal disadvantage.

To study the clonal dynamics of ENF-to-EPF replacements in situ at single-cell levels, we used a transgenic ‘Rainbow’ reporter system (*En1^{Cre};R26^{VT2/GK3}*)¹⁹. From the moment of *En1* expression, individual EPF progenitors were genetically marked with one out of three alternate fluorescent colours (yellow fluorescent protein (YFP), RFP or cyan fluorescent protein (CFP)), whereas ENFs expressed GFP. EPF progenitors were absent in the dermis at E9.5 and first appeared at E10.5 (Fig. 2a–d). Coronal sections at E10.5 showed that single EPFs and monoclonal cells developed in close association with the ectoderm and then extend from the most anterior regions (neck level) down to half of the trunk (Fig. 2b,c). EPFs remained absent in most posterior regions (including hindlimbs) at this stage. At E11.5, EPFs formed two parallel mid-lateral lines that covered the entire back (Fig. 2e). 3D reconstruction of E12.5 embryos showed that EPFs arrange themselves in an arc across the back-skin, with migration ‘protrusions’ at anterior sites (Fig. 2f and Supplementary Video 1).

We next performed immunolabelling of ECM proteins on histological sections of *En1^{Cre};R26^{VT2/GK3}* early-developing dermis.

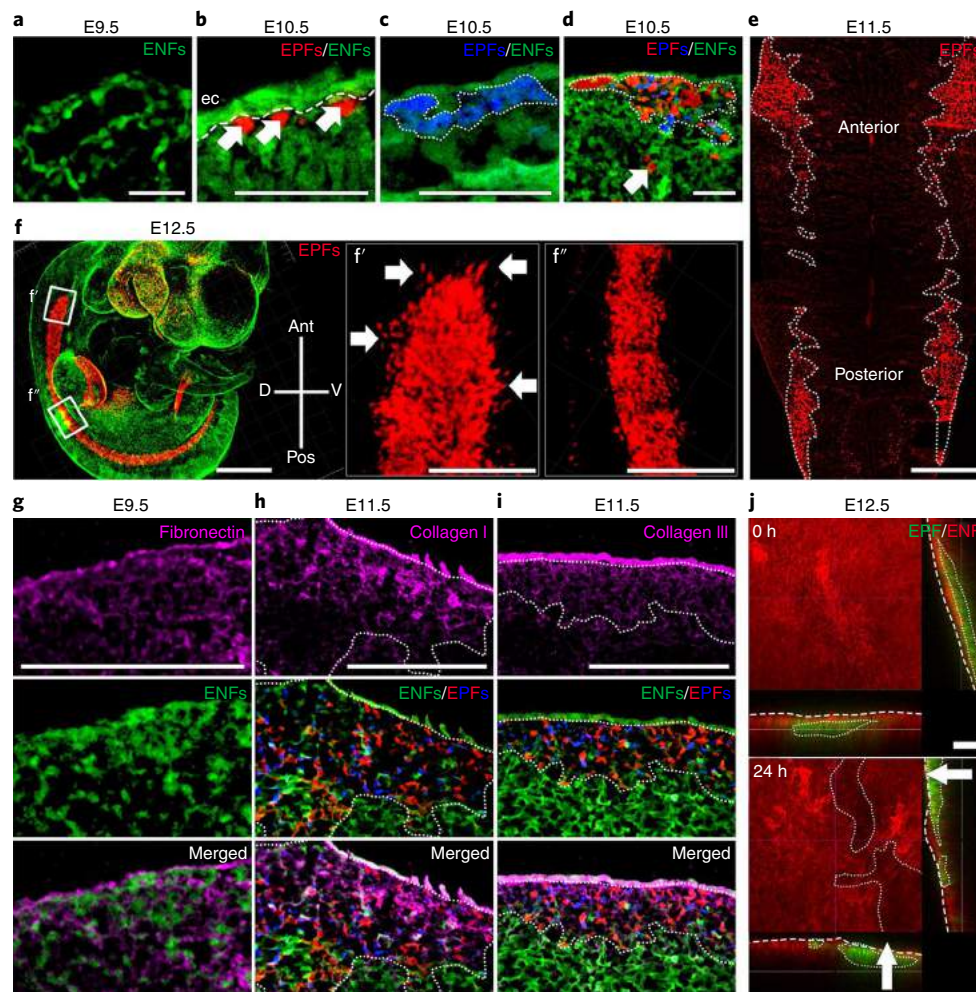


Fig. 2 | EPFs direct dermis development. **a–e**, Coronal sections of E9.5–E11.5 *En1^{Cre};R26^{VT2/GK3}* embryos. Arrows indicate single EPFs (**b,d**). Dashed line indicates the ectoderm (ec) border (**b**). Dotted lines delimitate EPFs clones (**c–e**). **f**, E12.5 *En1^{Cre};R26^{VT2/GK3}* embryo showing that EPFs arc across the back-skin. **f'** and **f''** indicate high magnification from boxes in **f**. Arrows indicate migrating EPFs. The cross indicates the embryonic axes. Ant, anterior; D, dorsal; Pos, posterior; V, ventral. **g–i**, Immunofluorescence for fibronectin (**g**), collagen I (**h**) or collagen III (**i**) in coronal sections of E9.5 or E11.5 *En1^{Cre};R26^{VT2/GK3}* embryos. Dotted lines delimitate EPFs. **j**, Orthogonal view from time-lapse images (0 h and 24 h) from the anterior region of an E12.5 *En1^{Cre};R26^{mTmG}* embryo. Dotted lines in the x–y frame delimitate the EPF-induced ENF gap. The green channel (EPFs) was omitted in x–y frames for clarity. Dotted lines from x–z and y–z delimitate EPFs. Dashed lines mark the dorsal surface. Arrows indicate the movement direction of EPFs. Scale bars, 50 μm (**a–d**), 500 μm (**e,f**), 200 μm (**f',f'',g–i**) and 100 μm (**j**). Images in **a–j** are representative of three experiments.

Unexpectedly, we found that ENFs deposited fibronectin fibres, but not collagen I and collagen III (Fig. 2g), indicating that ENFs generate a provisional matrix. At anterior sites, collagen I and collagen III fibres were visible within the dermal matrix in association with EPF clones, indicating that EPFs form a ‘mature’ dermis (Fig. 2h,i). Indeed, at later stages, collagen I expression was associated with EPFs (Supplementary Fig 3). To view the dynamics of ENF-to-EPF replacement, we performed live 3D confocal imaging of the developing back-skin of *En1^{Cre};R26^{mTmG}* embryos (E12.5) at the anterior margin of the EPF arc (Supplementary Fig. 4). We found that the ENF cytological structure is displaced to create open gaps into which EPFs migrated (Fig. 2j, Supplementary Fig. 4 and Supplementary Video 2). EPFs colonized the provisional dermis, through both dorsal and lateral trajectories (arrows in Fig. 2j). This local dynamic displacement of ENF-to-EPF cytological structures was completed within 24 hours.

We then analysed the migration behaviours of single cells in 3D by automatically tracking the migration paths of EPFs at 15-min intervals. We obtained 144 high-quality tracks of fibroblasts across an area of $\sim 170\ \mu\text{m}^2$ and $\sim 100\ \mu\text{m}$ deep (Fig. 3a). From a coronal plane of view, we observed characteristic reticular patterns in which

EPFs follow seemingly collective behaviours (Fig. 3b). The EPFs migrated in vertical columns along the dorsal–ventral axis (Fig. 3c,d). Anterior tracks had more dispersed points along the dorsal–ventral axis than posterior tracks, indicating that anterior EPFs migrated faster than posterior EPFs (Fig. 3e,f).

Unexpectedly, EPFs migrated uniformly and in three distinctive ways: (1) ‘converging’ migration to a fixed space (Fig. 3b), (2) ‘localized’ migration where EPFs move in a limited space without directly contacting each other (Fig. 3g) or (3) ‘diverging’ migration of several EPFs from a space unit (Fig. 3h). These three migration types occurred in clusters of 3–6 fibroblasts that shared common behaviours. Sequences of several units with varied migration behaviours could be detected even along a relative short distance of 170 μm , indicating that EPF movements in situ are directed locally by micro-environmental cues. These observations are in contrast to observations from fibroblast migration assays in 2D and demonstrate that EPFs exhibit intricate migration repertoires in vivo.

Dermal lattice development follows *En1* lineage replacement. Having documented the cellular conversion from ENFs to EPFs,

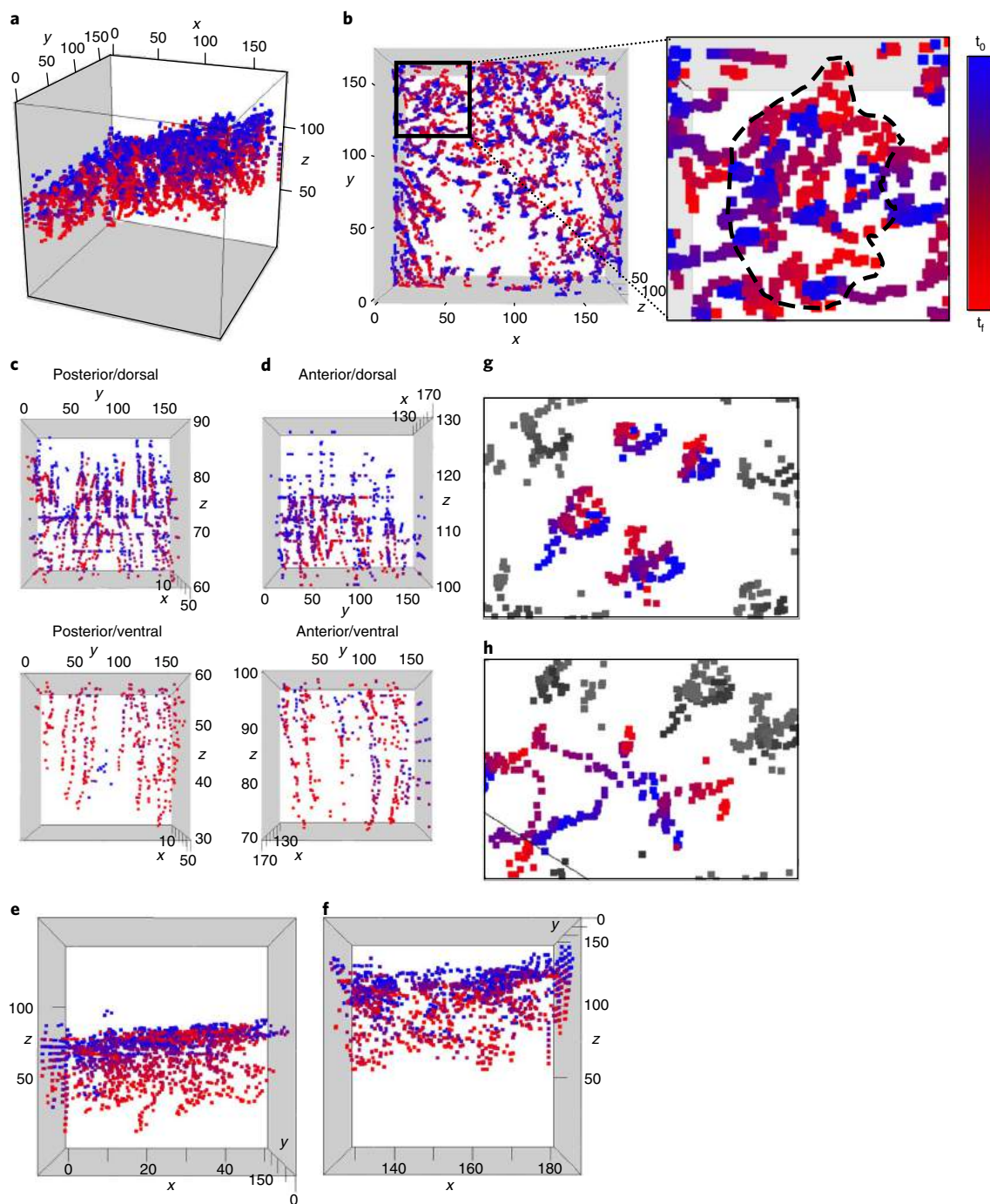


Fig. 3 | EPFs exhibit three migration behaviours in vivo. **a**, 4D scatter plot of individual tracks; the colour ramp indicates time (blue, first time point; red, last time point). **b**, Top x - y view showing the reticular patterns of migration. Dashed lines in the zoomed view (right panel) delimitate 'converging' track points. **c,d**, Lateral y - z views of posterior (**c**) or anterior (**d**) tracks split into dorsal (up) and ventral (down) regions. **e,f**, Frontal x - z views of posterior (**e**) or anterior (**f**) tracks. **g,h**, Amplified view of single tracks showing 'localized' (**g**) or 'diverging' (**h**) migrations. Colour ramps of tracks of no interest (**g,h**) were changed to greyscale for clarity. Axes units, μm . The 144 cell tracks were derived from one representative video.

we went on to describe dermal lattice development. As the dermal structure is too complex to be analysed with simple Euclidean geometry parameters, we turned to fractal analysis to measure the complexity of cellular and ECM fibre arrangements. In this analysis, the fractal dimensions (FD) and lacunarity (L) values quantitatively assess the complexity and porosity of 2D shapes (Supplementary Fig. 5a). The complex arrangements (for example, blood vessels and tumours^{20–22}) score higher FD values than simpler arrangements (for example, geometrical shapes). Porous structures

(for example, sponges) score higher L values than smooth surfaces (for example, scales).

We first resolved the cellular organization during dermal morphogenesis using histological sections of *En1*^{Cre}; *R26*^{VT2/GK3} embryos. Early (E11.5–E12.5) ENF regions were smoother and more complex, whereas later stages (E14.5–E16.5) became simpler and more porous (Supplementary Fig. 5b,c). This indicates a drift from a compact mesenchymal arrangement to a more interspaced cellular organization of a mature dermis. Anterior ENF arrangements

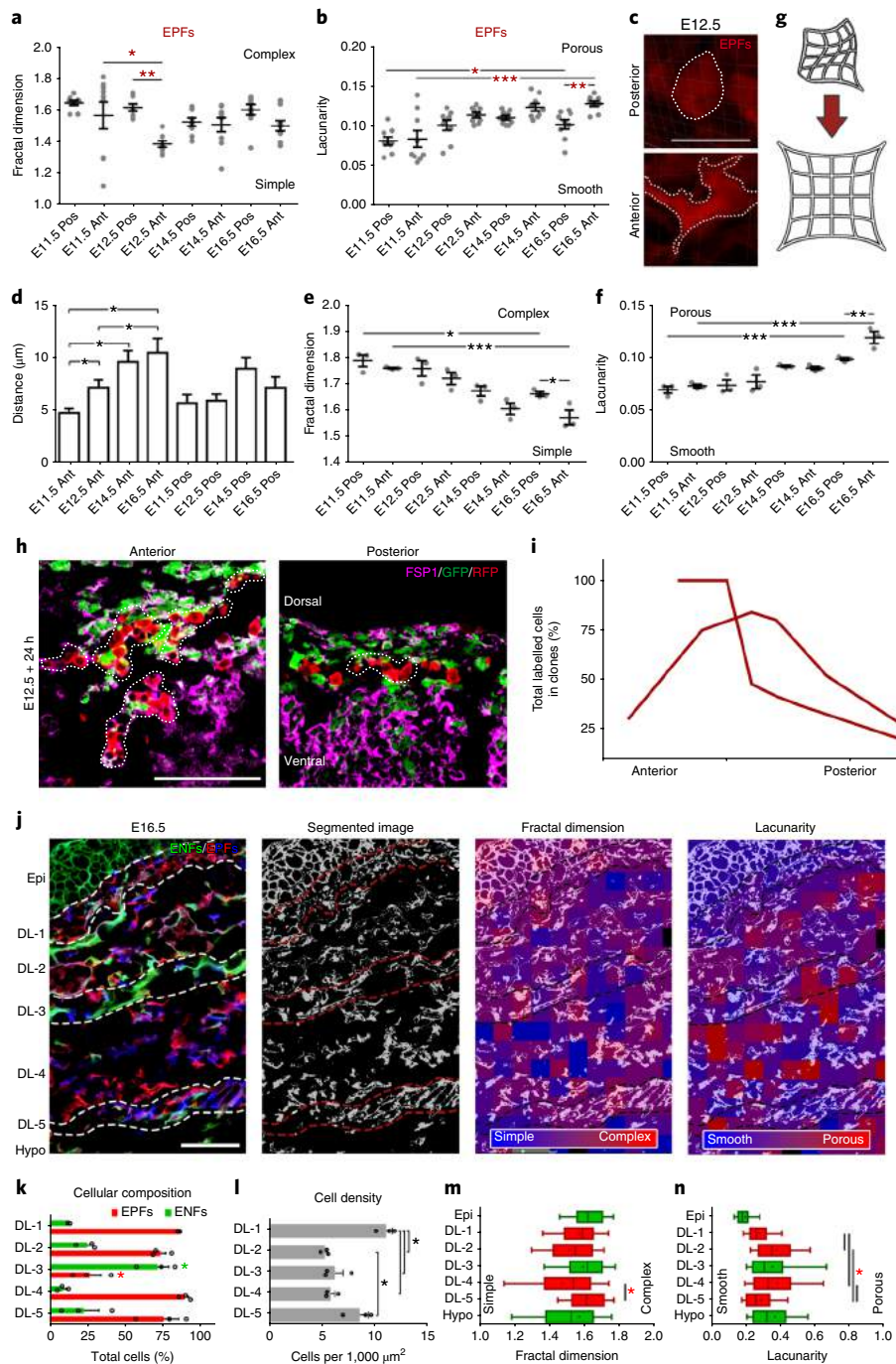


Fig. 4 | Dermal lattice is actively changing during development. **a, b**, Fractal dimension (FD) values (**a**) and lacunarity (L) values (**b**) derived from images of EPFs from different regions and developmental stages. Mean \pm s.e.m. Repeated measures ANOVA, Newman-Keuls test, $n = 9$ optical fields of anterior or posterior regions at E11.5, E12.5, E14.5 and E16.5. * $P < 0.05$, ** $P < 0.01$ and *** $P < 0.001$. **c**, 3D reconstructions of posterior and anterior *En1^{Cre};R26^{VT2/GK3}* EPFs. **d**, Distances (μm) between fibronectin fibres calculated from linear profiles of three confocal images of fibronectin-immunolabelled sections (Supplementary Fig. 6; $n = 184$ (E11.5 anterior), 138 (E11.5 posterior), 135 (E12.5 anterior), 155 (E12.5 posterior), 98 (E14.5 anterior), 105 (E14.5 posterior), 91 (E16.5 anterior), 128 (E16.5 posterior) measurements), mean \pm s.e.m., ANOVA, Holm-Sidak test, * $P < 0.05$. **e, f**, FD values (**e**) and L values (**f**) derived from fibronectin stainings from different regions and developmental stages. Mean \pm s.e.m. Repeated measures ANOVA, Newman-Keuls test, $n = 3$ optical fields of anterior or posterior regions at E11.5, E12.5, E14.5 and E16.5. * $P < 0.05$, ** $P < 0.01$ and *** $P < 0.001$. **g**, Fibronectin matrix changes from a relaxed framework to a rigid matrix. **h**, FSP1 expression in anterior (left) or posterior (right) regions of E12.5 *Actin^{Cre-ER};R26^{VT2/GK3}* embryos after 24 h of 1 nM 4-hydroxytamoxifen exposure. Dotted lines delimitate single clones. **i**, Percentage of labelled cells in clones from two independent embryos. **j**, Local (subsampled) fractal analysis of a E16.5 *En1^{Cre};R26^{VT2/GK3}* dermis. Dashed lines delimitate dermal layers. **k**, Percentages \pm s.e.m. of EPFs and ENFs in each layer; $n = 3$ optical fields. Two-way ANOVA, * $P < 0.05$, Tukey test. **l**, Mean \pm s.e.m. number of cells per $1,000 \mu\text{m}^2$ of each layer; $n = 3$ optical fields. One-way ANOVA, * $P < 0.05$, Tukey test. **m, n**, FD values (**m**) and L values (**n**) derived from different dermal layers; n for FD and L, respectively = 58 and 58 (epidermis), 65 and 65 (DL-1), 198 and 199 (DL-2), 62 and 62 (DL-3), 274 and 281 (DL-4), 92 and 92 (DL-5), and 87 and 91 (hypodermis) subsampled values pooled from 3 confocal images. Box and whiskers plots with minimum, lower quartile, median, upper quartile and maximum. One-way ANOVA, * $P < 0.05$, Tukey test. Scale bars, $20 \mu\text{m}$ (**c**), $200 \mu\text{m}$ (**h**) and $50 \mu\text{m}$ (**j**). P values are listed in Supplementary Table 1.

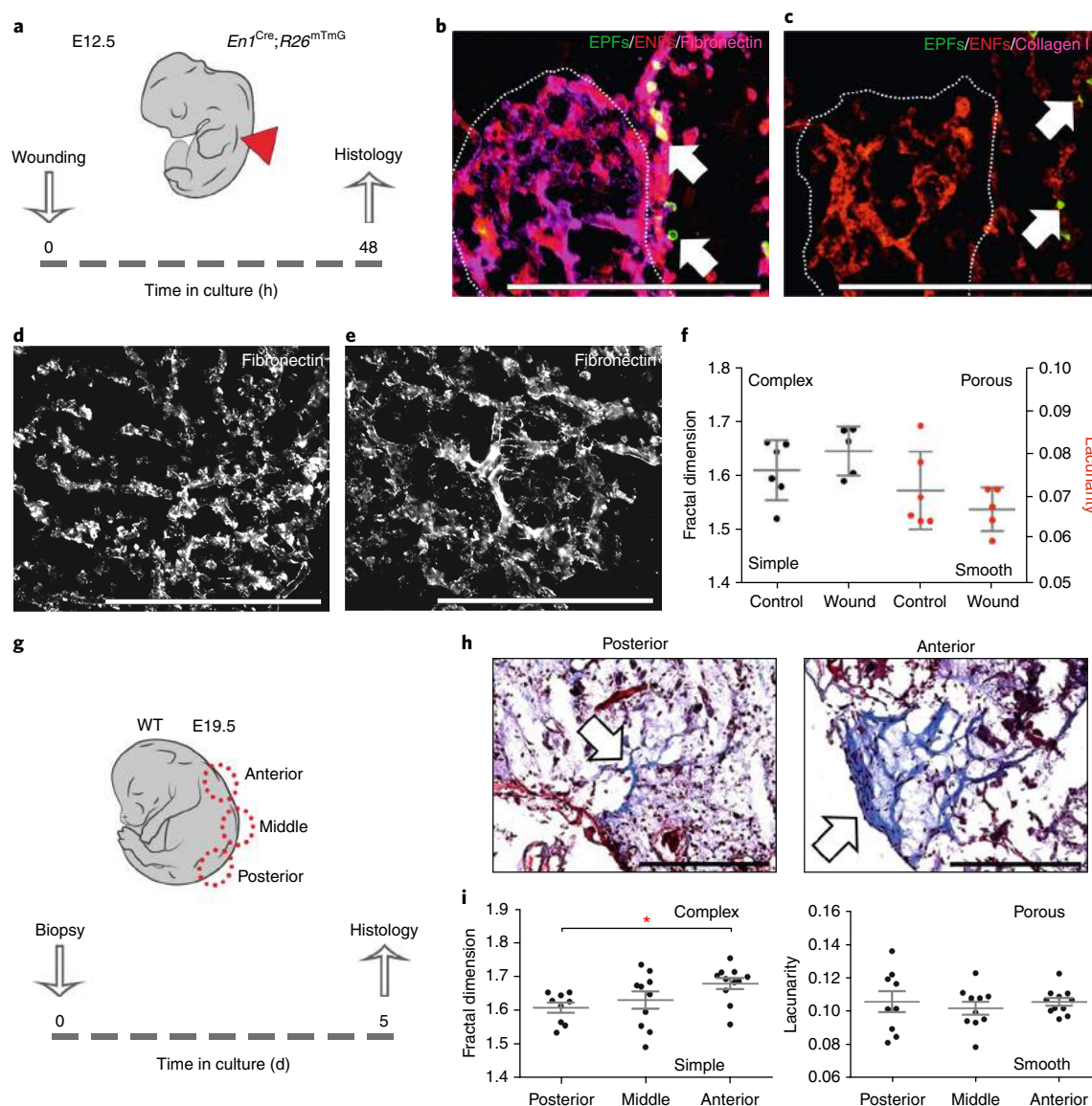


Fig. 5 | Regeneration-to-scar transition is coupled to EPFs development. **a**, E12.5 *En1^{Cre};R26^{mTmG}* embryos were collected, wounded on the back-skin and kept in culture for 48 h. **b,c**, Immunofluorescence for fibronectin (**b**) or collagen I (**c**). Dotted lines delimitate the lesion site. Arrows indicate EPFs. **d,e**, Representative immunofluorescence images of fibronectin staining at adjacent fetal skin (control) (**d**) and the wounded site (**e**) at 48 h post-wounding. **f**, FD values (left) and L values (right) derived from fibronectin staining at adjacent fetal skin (control) and the wounded site at 24 h and 48 h after wounding. $n=6$ optical fields of control skins and $n=5$ optical fields of wounds from two embryos. Mean \pm s.e.m. Two-tailed unpaired Student's *t*-test. **g**, Skin biopsies were taken from anterior, middle and posterior regions of E19.5 WT embryos and cultured for 5 days. **h**, Masson's trichrome-stained sections of posterior or anterior biopsies. Arrows indicate the scar-like deposition of the ECM. **i**, FD values (left) and L values (right) derived from the cyan channel of Masson's trichrome-stained biopsies. Anterior: $n=11$, middle: $n=10$ and posterior: $n=9$. Mean \pm s.e.m. One-way ANOVA, Tukey test, $*P=0.0436$. Scale bars, 200 μ m.

at E12.5 were more complex and smoother than posterior cells (Supplementary Fig. 5c), indicating that, at E12.5, anterior and posterior regions have different cellular organizations.

Conversely, EPFs underwent two major cellular rearrangements during development: (1) early EPFs (E10.5–E11.5) cluster tightly in complex patterns, with individual cells having smooth shapes; and (2) after E12.5, these clusters split into individual cells with increasing complex arrangements (Fig. 4a,b). At E12.5, anterior EPFs decreased in FD value, whereas posterior EPFs retained similar complexity to their earlier stage. 3D-rendered pictures of single EPFs revealed that posterior EPFs were morphologically simpler than anterior EPFs (Fig. 4c). A sudden increase in complexity of anterior EPFs in E12.5 embryos correlated in time with the migration of EPFs (Figs. 2f,j and 3, Supplementary Fig. 4 and

Supplementary Videos 1 and 2), suggesting that changes in EPF morphology cause or are caused by migrations. Together, our fractal analysis characterizes dynamic spatiotemporal changes in dermal lattice development and link dermal maturation steps to distinct embryonic fibroblastic lineages.

To determine whether dermal lattice organization is changed following the expansion of EPFs, we analysed matrix fibre alignment at different stages in dermal regions that do or do not contain EPFs. As collagen precludes the earlier stages of development where EPFs initially seed the back-skin, we used fibronectin to study the patterns of dermal lattice development. The distance between fibres increased progressively from E11.5 to E16.5 (Fig. 4d and Supplementary Fig. 6), concurrent with EPF development. At the same time, there was a progressive decrease in complexity and an increase in porosity

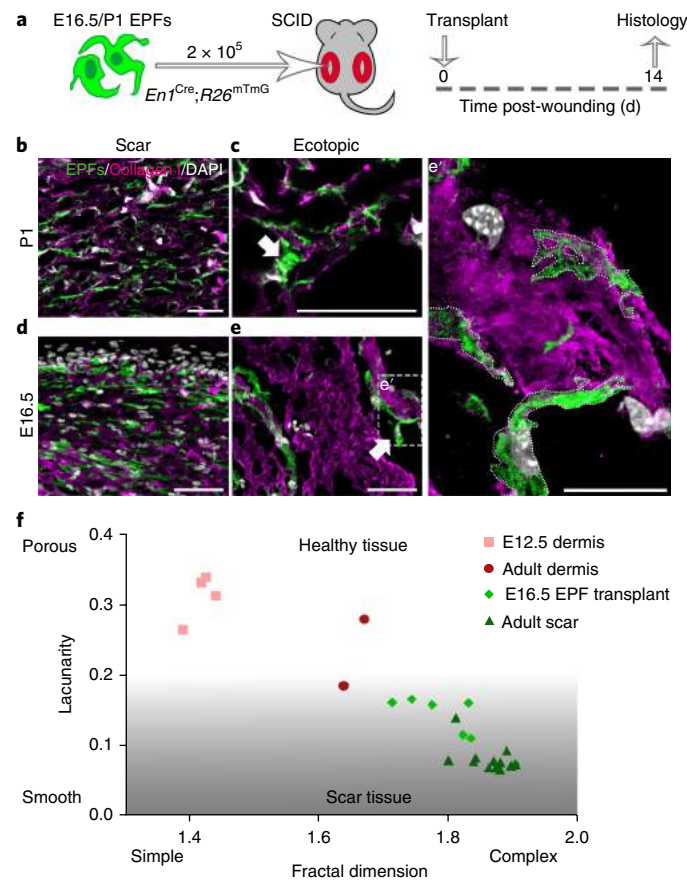


Fig. 6 | EPFs are a mature scar-matrix-depositing population. **a**, E16.5 or P1 $En1^{Cre};R26^{mTmG}$ EPFs were sorted and transplanted (2×10^5) into fresh splinted wounds of adult $Rag2^{-/-}$ mice (SCID) and the tissue was collected 14 days later. **b–e**, Immunofluorescence for collagen I of scars (**b,d**) or ectopic uninjured sites (**c,e**) containing transplanted EPFs from P1 mice (**b,c**) or E16.5 embryos (**d,e**). **e'** is a high-magnification image of a collagen I-attached EPF. Dotted lines delimitate the cell bodies of EPFs. **f**, Collagen I FD and L scatter plot of E12.5 and adult normal dermis, adult scars and scars derived from E16.5 EPF transplants. Scale bars, 50 μ m (**b–e**) and 20 μ m (**e'**). Images represent one out of three experiments.

(Fig. 4e,f). This demonstrates that a gradual transformation of the dermal fibronectin matrix occurs, from a relaxed and disorganized framework towards a more stretched conformation (Fig. 4g). Our fractal analysis of EPF's cellular arrangements stresses that E12.5 is a pivotal time-point when anterior regions are actively changing while posterior regions are still dormant. The co-occurrence of fibronectin framework transformation and EPF morphological changes links ECM arrangements with distinct cell-migration behaviours during development. To directly prove this link, we used an inducible-Cre labelling system to follow single fibroblastic cells (either ENFs or EPFs) and their sibling cells during back-skin development, and compared behaviours between anterior and posterior sites. Fibroblastic clone size increased and clone expansion extended across the dorsal–ventral axis in the most anterior locations, whereas singly labelled cells and small clones remained close to the ectoderm in posterior regions (Fig. 4h,i). These experiments show that the dynamics of structural changes across the anterior–posterior dermal axis influence both the cell division rate of fibroblastic precursors and the migration trajectories of their clonal colonies.

Next, we aimed to detect in more detail discrete cellular arrangements at later stages, when fibroblast clones are too widespread and intermixed. We generated a tissue-level description of dermal cellular organization by calculating local FD and L values from E16.5 $En1^{Cre};R26^{VT2/GK3}$ embryos. Low-power images showed that more-compact tissues, such as the epidermis, hypodermis, muscle and cartilage, had higher FD values than the dermis (Supplementary Fig. 5d,e), indicating the validity of the fractal analysis. From the

high-power images, we could identify five distinct dermal layers (DL-1–DL-5) organized in parallel sheets across the back-skin (Fig. 4j–n). DL-1 and DL-5 were in direct contact with the epidermis and the hypodermis, respectively, and were more complex and smoother, and were composed of densely packed EPFs (~85% and ~75%, respectively). DL-2 and DL-4 were simpler and porous, and were composed predominantly of EPFs (~75% and ~90%, respectively). DL-3 was complex and porous and was composed primarily of elongated ENFs (~75%). Thus, the cellular organization of the dermis at E16.5 has a mirrored pattern with outer flanking dense dermal layers that are in direct contact with the epidermis and the hypodermis, and two intermediate porous layers, which are separated by a middle layer devoid of EPFs. Critically, within each internal layer there are microdomains with distinct complexity values across the anterior–posterior axes. Tissue structure complexity and porosity does not vary linearly across these microdomains. In fact, in several places, the deep dermis is abruptly interspersed with distinct cellular arrangements (right panels in Fig. 4j), which might result from local migration patterns at earlier stages of development.

Scarring transition follows an anterior-to-posterior sequence.

We showed above that EPFs increase within the back-skin from an anterior-to-posterior sequence. We previously showed that adult EPFs produce scars¹. Thus, we speculated that the fetal regeneration-to-scar transition is linked to engrailed lineage replacement and could be due to the gradual increase in EPF abundance during dermal development. If this is correct, we would expect that wounds

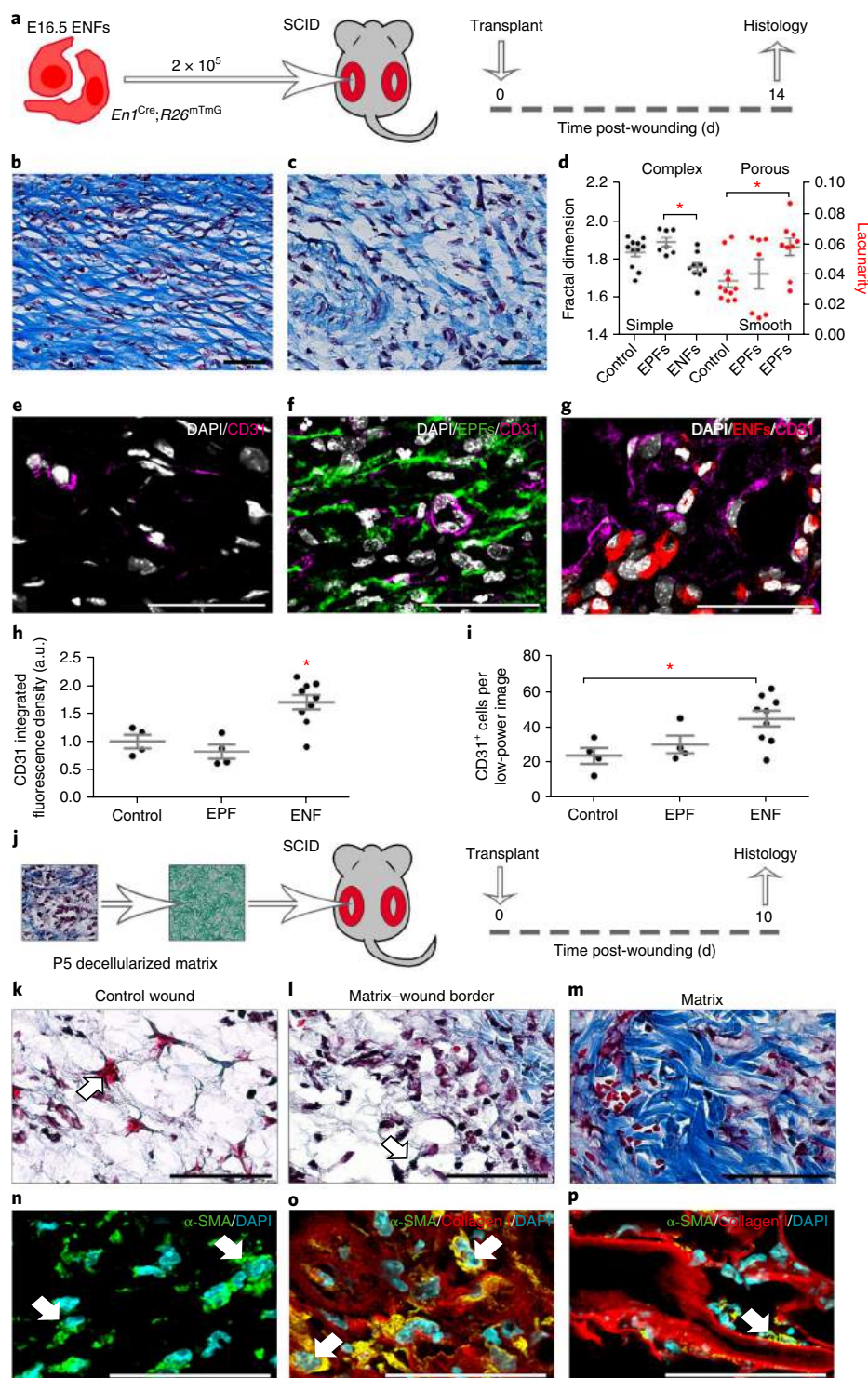


Fig. 7 | ENF and ECM transplantations improve scar outcomes. **a**, E16.5 *En1^{Cre};R26^{mTmG}* EPFs were sorted and transplanted (2×10^5) into fresh splinted wounds of adult *Rag2^{-/-}* mice and the tissue was collected 2 weeks later. **b,c**, Masson's trichrome staining of the EPF-transplanted scar (**b**) and the ENF-transplanted scar (**c**). **d**, FD values (left) and L values (right) derived from the cyan channel of Masson's trichrome-stained sections. Mean \pm s.e.m. $n = 11$ optical fields of control, $n = 7$ optical fields of EPF transplants and $n = 9$ optical fields of ENF transplants. One-way ANOVA, $*P < 0.05$, Tukey test. **e-g**, Representative immunofluorescence images of CD31 staining on mock-transplant scars (control) (**e**), EPF-transplant scars (**f**) or ENF-transplant scars (**g**). **h,i**, Quantification of CD31 integrated fluorescence density (**h**) and CD31⁺ cells per low-power ($\times 20$) image (**i**) of mock-transplant, EPF-transplant and ENF-transplant scars. Mean \pm s.e.m. $n = 4$ optical fields of control, $n = 4$ optical fields of EPF-transplant scars and $n = 9$ optical fields of ENF-transplant scars, pooled from two independent experiments. One-way ANOVA, $*P < 0.05$, Tukey test. a.u., arbitrary unit. **j**, Decellularized matrix transplantation experiment. Back-skin explants from P5 WT mice were decellularized and transplanted into fresh splinted wounds of adult *Rag2^{-/-}* mice and the tissue was collected 10 days later. **k-m**, Masson's trichrome-stained (**k-m**) or α -SMA-stained and collagen I-stained (**n-p**) control wounds (**k,n**), the border between the transplanted matrix and the wound (**l,o**) or within the transplanted matrix (**m,p**). Scale bars, 50 μ m. Images in panels **b,c**, **e-g** and **k-p** represent one out of two experiments. The exact P values are listed in Supplementary Table 1.

inflicted at early fetal stages would regenerate from ENFs and that the transition from regeneration-to-scarring would take on an anterior-to-posterior sequence.

To test our first hypothesis, we generated wounds in the back-skin of *En1^{Cre};R26^{mTmG}* E12.5 embryos and analysed both lineage compositions and ECM depositions (Fig. 5a). At 48 hours post-wounding, ENFs had migrated into wound beds, where a provisional fibronectin-rich matrix had been generated, virtually absent of EPFs or collagen I fibres (Fig. 5b,c). Fractal analysis of fetal wounds indicated that lattice arrangement at the injury site was not different from that of the adjacent fetal skin (Fig. 5d–f). Thus, during fetal skin regeneration, ENFs sculpt the wound-bed matrix without the intervention of EPFs.

To test our second hypothesis, we cultured skin biopsies from different anterior–posterior regions of E19.5 wild-type (WT) embryos (Fig. 5g). Anterior biopsies deposited significantly more collagen-rich scars (right panel in Fig. 5h) than posterior biopsies (left panel in Fig. 5h). Fractal analysis revealed that the posterior matrix was significantly simpler than the anterior matrix (Fig. 5i), suggesting that, at this stage, anterior fibroblasts are more fitted to create a scar than are posterior fibroblasts. Collectively, these experiments demonstrate that the fetal regeneration-to-scar transition follows the increase in EPF abundance during dermal development.

***En1* lineage replacement drives regeneration-to-scar transition.**

We next asked whether EPFs from early stages possess scarring capacities or whether, alternatively, they undergo a developmental maturation, whereby they acquire scar-producing abilities over time. To test this idea, we purified EPFs from the back-skin of *En1^{Cre};R26^{mTmG}* embryos/neonates at regenerating (E16.5) or scarring (P1) stages and intradermally transplanted them in equal number (2×10^6) around the edges of fresh splinted wounds on the back-skin of adult immunodeficient (*Rag2^{-/-}*) mice. We then assessed the contribution of EPFs from different ages to scar formation 14 days after transplantation/wounding (Fig. 6a). Transplanted EPFs from P1 that migrated into the wounds deposited collagen I extensively within host wound beds (Fig. 6b). Some EPFs deposited ectopic collagen I at their original transplanted location (Fig. 6c). Strikingly, transplanted EPFs from E16.5 embryos had the same scarring capacities as P1 EPFs, depositing collagen I both within wounds and at ectopic uninjured sites (Fig. 6d,e). EPFs from both E16.5 and P1 had pathologically active cell morphologies, with membrane protrusions that span across and intermingle with the collagen I fibres (Fig. 6e). Fractal analysis showed that collagen I arrangements were more complex and smoother in EPF-transplanted regions (day 14 post-wounding) and in adult scars (day 21 post-wounding) than in non-injured adult and fetal dermis, which were simpler and more porous (Fig. 6f). Our results demonstrate that fetal EPFs are capable of producing and organizing a scar tissue, just as well as newborn EPFs, and that the absence of scar formation in early fetal skin is due to scarcity of EPFs, rather than their developmental immaturity. Together, the mechanism behind the dynamic transition from regeneration to scarring in fetus is *En1* lineage replacement during back-skin development.

ENFs or native lattice reduce scarring in adult wounds. As we found that ENF abundance in the dermis was associated with regenerative outcomes at early stages and as we also showed that ENFs sculpted a provisional lattice during development, we asked whether transplantation of ENFs alone would regenerate adult dermal wounds. To test this hypothesis, we transplanted fetal (E16.5) ENFs into back-skin wounds of adult *Rag2^{-/-}* mice and allowed wounds to heal for 14 days (Fig. 7a). As expected, sites of ENF transplantations had a more reticular lattice arrangement than fibrotic lattice arrangements at sites of EPF transplantations (Fig. 7b,c). Fractal analysis indicated that ENF transplantation sites were significantly simpler and more porous in lattice arrangements

than EPF-transplanted sites or mock-transplanted control wounds (Fig. 7d). In line with the reduction of scarring severity, immunolabelling of an endothelial marker, CD31, showed a significantly higher infiltration of blood vessels into the wound beds at sites of ENF transplantations than EPF-transplanted or mock-transplanted wounds (Fig. 7e–i). Many of the transplanted ENFs were closely associated with blood vessels, which were interlaced with one another to generate vascular networks within the transplanted sites (Fig. 7g).

To test whether the ENF-generated lattice itself promotes a regenerative outcome, we transplanted decellularized back-skin from P5 WT mice into back-skin wounds of *Rag2^{-/-}* mice (Fig. 7j). Ten days later, we found that fibroblasts in the control wounds and in the borders between the wound and the transplanted matrix had a typical active morphology with membrane protrusions (Fig. 7k,l). Conversely, resident cells within the transplanted matrix had an inactive morphology with round cytoplasm (Fig. 7m). Immunolabelling of α -SMA revealed that the activated fibroblasts were present in the control wound beds and in the matrix–wound border (Fig. 7n,o) and were mostly devoid from transplanted matrix (Fig. 7p). These experiments show that a ‘healthy’ dermal lattice can be imposed locally in two ways. First, transplanting ENFs expands the existing pool of resident ENFs and allows ENFs to sculpt a provisional matrix. Alternatively, transplantations of decellularized dermal lattice, in essence, mimic dermal development, and in the presence of which EPFs do not promote a pathological scar. Both approaches, if they could be made industrially, provide therapeutic possibilities for a range of dermal pathologies, including patients with large skin burns or wounds.

Discussion

We have previously shown¹¹ that EPFs are the primary cells responsible for fibrotic outcomes in adult settings of wound healing, irradiation fibrosis and melanoma cancer growth. Here, we find that ENFs, not EPFs, are the primary sculptors that drive dermal lattice development and its regeneration in fetal wound-healing settings. We show that transplanted fetal ENFs and EPFs into adult wounds impose regenerative versus scarring outcomes, respectively, and that the phenotypic shift in dermal response to injury (from regeneration to scarring) is driven by *En1* lineage replacement (Supplementary Fig. 7).

Using *in vivo* live imaging, we disclose three distinct migration patterns of dermal fibroblasts during back-skin development: localizing, diverging or converging migrations. To our knowledge, these migration patterns have never been described in 2D or 3D assays to date. We hypothesize that each of the three migration patterns establishes distinct dermal architectures that collectively drive the remarkable architectural complexity that we observe during dermal development. Diverging migration patterns could indicate fibroblastic cell invasiveness, whereas converging migrations indicate collective and interconnected behaviours as opposed to individualistic. As fibroblastic migrations impinge on collagen-bundle alignments, we expect these individual migration patterns, through their distinct molecular programmes, to influence scar tissue severity, as well as fibroblastic invasiveness into tumours.

Our findings have additional developmental, evolutionary and clinical implications outlined below.

Other groups have recently implicated separate fibroblastic lineages in the differentiation of the back-skin epidermis^{18,23,24}. Fetal processes of epidermal development, hair follicle and sebaceous gland differentiation may require specialized stromal signals and cells. The priority for adults is a quick fix of breached skin, which probably requires different stromal signals and cells to produce a scar. These two diverged requirements at different stages of fetal life are maintained through dynamic cellular shuffling of fibroblastic populations, allowing specialized types of fibroblasts to accommodate specific fetal and adult requirements.

We demonstrate here that the ENF-to-EPF switch in the dermis imposes the phenotypic transition from regeneration to scarring in response to injury. In evolutionary terms, this switch provides a model to explain how dermal regeneration was retained in some adult rodent species such as African spiny mice²⁵. We speculate that such species have retained the fibroblastic cell compositions of fetal-stage dermis (ENFs > EPFs), and have resisted the ENF-to-EPF lineage successions.

Here, we describe, and map in detail, a mechanism for the general acquisition of scarring ability in the skin. We believe both the temporal and the spatial dynamics of EPFs, the determinants of scarring, will be widely clinically applicable. Consideration of lineages with engrailed history will outline a favourable time window for surgeons to work in, when scarring outcomes will be predicted to be at a bare minimum, such as during corrective surgery for spina bifida, or equally, it could be applicable to the removal of paediatric malignancies.

Our findings also carry implications for adult scarring. There are no definitive strategies to prevent scar formation, and current clinical practice is focused on scar acceptance rather than its amelioration. We have demonstrated two separate strategies that reduce scar outcomes in adult injured skin. Both ENF transplantation and decellularized dermis transplantation assays provide a proof of concept for a therapeutic option that could be used to treat large wounds, scolds or burns.

Our findings also create opportunities for the intense field of bioengineered autologous dermoepidermal human skin grafts that are currently being tested in phase I and phase II clinical studies. Skin grafts include all fibroblastic lineages within the dermis and are therefore likely to produce scars upon transplantation. We predict it would be advantageous to graft pure human ENFs or ENFs combined with dermoepidermal skin. In essence, this dermal milieu would override the ENF-to-EPF population shift and favour regeneration over scarring.

In summary, we used single-cell clonal analysis, 3D imaging, computational cell tracking and in silico analysis to follow the behaviours of fibroblast lineages in vivo. We document fibroblast-lineage-specific proliferations, migrations and secretions, and demonstrate how such a fundamental process as dermal morphogenesis actually occurs. Our finding of *En1* lineage replacement links dermal morphogenesis with the phenotypic shift in response to dermal injury. We believe our findings open up previously unrecognized opportunities for clinical approaches to ameliorate scar tissues in injured adult skin.

Methods

Methods, including statements of data availability and any associated accession codes and references, are available at <https://doi.org/10.1038/s41556-018-0073-8>.

Received: 22 November 2017; Accepted: 23 February 2018;
Published online: 28 March 2018

References

- Gurtner, G. C., Werner, S., Barrandon, Y. & Longaker, M. T. Wound repair and regeneration. *Nature* **453**, 314–321 (2008).
- Ud-Din, S., Volk, S. W. & Bayat, A. Regenerative healing, scar-free healing and scar formation across the species: current concepts and future perspectives. *Exp. Dermatol.* **23**, 615–619 (2014).
- Armstrong, J. R. & Ferguson, M. W. Ontogeny of the skin and the transition from scar-free to scarring phenotype during wound healing in the pouch young of a marsupial, *Monodelphis domestica*. *Dev. Biol.* **169**, 242–260 (1995).
- Ihara, S., Motobayashi, Y., Nagao, E. & Kistler, A. Ontogenetic transition of wound healing pattern in rat skin occurring at the fetal stage. *Development* **110**, 671–680 (1990).
- Lorenz, H. P., Whitby, D. J., Longaker, M. T. & Adzick, N. S. Fetal wound healing. The ontogeny of scar formation in the non-human primate. *Ann. Surg.* **217**, 391–396 (1993).
- Longaker, M. T., Dodson, T. B. & Kaban, L. B. A rabbit model for fetal cleft lip repair. *J. Oral Maxillofac. Surg.* **48**, 714–719 (1990).
- Kishi, K., Okabe, K., Shimizu, R. & Kubota, Y. Fetal skin possesses the ability to regenerate completely: complete regeneration of skin. *Keio J. Med.* **61**, 101–108 (2012).
- Ferguson, M. W. & O’Kane, S. Scar-free healing: from embryonic mechanisms to adult therapeutic intervention. *Philos. T. Roy. Soc. B* **359**, 839–850 (2004).
- Longaker, M. T. et al. Adult skin wounds in the fetal environment heal with scar formation. *Ann. Surg.* **219**, 65–72 (1994).
- Cass, D. L. et al. Wound size and gestational age modulate scar formation in fetal wound repair. *J. Pediatr. Surg.* **32**, 411–415 (1997).
- Rinkevich, Y. et al. Identification and isolation of a dermal lineage with intrinsic fibrogenic potential. *Science* **348**, aaa2151 (2015).
- Muzumdar, M. D., Tasic, B., Miyamichi, K., Li, L. & Luo, L. A global double-fluorescent Cre reporter mouse. *Genesis* **45**, 593–605 (2007).
- Joe, A. W. et al. Muscle injury activates resident fibro/adipogenic progenitors that facilitate myogenesis. *Nat. Cell Biol.* **12**, 153–163 (2010).
- Uezumi, A., Fukada, S., Yamamoto, N., Takeda, S. & Tsuchida, K. Mesenchymal progenitors distinct from satellite cells contribute to ectopic fat cell formation in skeletal muscle. *Nat. Cell Biol.* **12**, 143–152 (2010).
- Cordani, N., Pisa, V., Pozzi, L., Sciorati, C. & Clementi, E. Nitric oxide controls fat deposition in dystrophic skeletal muscle by regulating fibro-adipogenic precursor differentiation. *Stem Cells* **32**, 874–885 (2014).
- Crisan, M. et al. A perivascular origin for mesenchymal stem cells in multiple human organs. *Cell Stem Cell* **3**, 301–313 (2008).
- Dominici, M. et al. Minimal criteria for defining multipotent mesenchymal stromal cells. The International Society for Cellular Therapy position statement. *Cytotherapy* **8**, 315–317 (2006).
- Driskell, R. R. et al. Distinct fibroblast lineages determine dermal architecture in skin development and repair. *Nature* **504**, 277–281 (2013).
- Rinkevich, Y., Lindau, P., Ueno, H., Longaker, M. T. & Weissman, I. L. Germ-layer and lineage-restricted stem/progenitors regenerate the mouse digit tip. *Nature* **476**, 409–413 (2011).
- Khorasani, H. et al. A quantitative approach to scar analysis. *Am. J. Pathol.* **178**, 621–628 (2011).
- Gould, D. J., Vadakkan, T. J., Poché, R. A. & Dickinson, M. E. Multifractal and lacunarity analysis of microvascular morphology and remodeling. *Microcirculation* **18**, 136–151 (2011).
- Di Ieva, A., Esteban, F. J., Grizzi, F., Klonowski, W. & Martín-Landrove, M. Fractals in the neurosciences, part II: clinical applications and future perspectives. *Neuroscientist* **21**, 30–43 (2015).
- Rognoni, E. et al. Inhibition of β -catenin signalling in dermal fibroblasts enhances hair follicle regeneration during wound healing. *Development* **143**, 2522–2535 (2016).
- Sennett, R. et al. An integrated transcriptome atlas of embryonic hair follicle progenitors, their niche, and the developing skin. *Dev. Cell* **34**, 577–591 (2015).
- Seifert, A. W. et al. Skin shedding and tissue regeneration in African spiny mice (*Acomys*). *Nature* **489**, 561–565 (2012).

Acknowledgements

Y.R. was supported by the Human Frontier Science Program Career Development Award (CDA00017/2016), the German Research Foundation (RI 2787/1-1 AOBJ: 628819) and the Fritz-Thyssen-Stiftung (2016-01277). J.L. was supported by the China Scholarship Council. D.C.-G. was supported by the Consejo Nacional de Ciencia y Tecnología (CONACYT) and the Deutscher Akademischer Austauschdienst (DAAD).

Author contributions

Y.R. outlined and supervised the research narrative and designed all the experiments. D.J. performed the wound-healing studies, the flow cytometric analysis and sorting of EPFs and ENFs, the cell transplantations and decellularized skin transplantations. D.C.-G. and A.S. performed and analysed the clonal analysis studies and generated the confocal images. D.C.-G. performed the fractal analysis. S.C. and P.R. performed live-imaging and cell-tracking analysis. J.L. and V.R. assisted with clonal analysis, confocal imaging and histological sectioning. M.M.D.S. and D.E.W. generated the decellularized dermis. Y.R. wrote the manuscript.

Competing interests

The authors declare no competing interests.

Additional information

Supplementary information is available for this paper at <https://doi.org/10.1038/s41556-018-0073-8>.

Reprints and permissions information is available at www.nature.com/reprints.

Correspondence and requests for materials should be addressed to Y.R.

Publisher’s note: Springer Nature remains neutral with regard to jurisdictional claims in published maps and institutional affiliations.

Methods

Mice strains and genotyping. All mouse strains (C57BL/6J (WT), *En1^{Cre}*, *Actin^{Cre-ER}*, *R26^{VT2/GK3}*, *R26^{mTmG}* and *Rag2^{-/-}*) were either obtained from Jackson laboratories, Charles River, or generated at the Stanford University Research Animal Facility as described previously¹¹, and were housed at the Helmholtz Center Animal Facility. The rooms were maintained at constant temperature and humidity with a 12-h light cycle. Animals were allowed food and water ad libitum. All animal experiments were reviewed and approved by the Government of Upper Bavaria and registered under the project 55.2-1-54-2532-61-2016 and conducted under strict governmental and international guidelines. This study is compliant with all relevant ethical regulations regarding animal research.

Cre-positive (Cre⁺) embryos were identified by detection of relevant fluorescence into the dorsal dermis. Genotyping was performed to distinguish mouse lines containing 200-base pair (bp) Cre fragment (Cre^{+/+}) from the WT (Cre^{-/-}). The genomic DNA from the ear clips was extracted using QuickExtract DNA extraction solution (Epicenter) following the manufacturer's guidelines. DNA extract (1 µl) was added to each 24 µl PCR. The reaction mixture was set up using Taq PCR core kit (Qiagen) containing 1× coral buffer, 10 mM dNTPs, 0.625 units Taq polymerase, 0.5 µM forward primer "Cre_genotype_4F"-5' ATT GCT GTC ACT TGG TCG TGG C-3'" (Sigma) and 0.5 µM reverse primer "Cre_genotype_4R"-5' GGA AAA TGC TTC TGT CCG TTT GC-3'" (Sigma). PCRs were performed with initial denaturation for 10 min at 94°C, amplification for 30 cycles (denaturation for 30 s at 94°C, hybridization for 30 s at 56°C, and elongation for 30 s at 72°C) and final elongation for 8 min at 72°C, and then cooled to 4°C. In every experiment, negative controls (non-template and extraction) and positive controls were included. The reactions were carried out in an Eppendorf master cycler. Reactions were analysed by gel electrophoresis.

Cell harvesting and sorting. Dorsal skin of *En1^{Cre};R26^{mTmG}* embryos, neonates or adult mice were harvested and washed with Hank's balanced salt solution (HBSS). Skin was minced into small pieces with surgical scissors and washed again with HBSS. The cells were resuspended in 2 ml of digestion solution containing 1 mg ml⁻¹ of collagenase I, 0.5 mg ml⁻¹ of hyaluronidase and 25 U ml⁻¹ of DNase I, and incubated in a 37°C water bath for 30 min with agitation. DMEM (10 ml) containing 10% FBS was added to stop the enzymatic reaction, and the suspension was filtered through a 100-µm and then 40-µm cell strainer. After centrifugation at 300g for 5 min, the cell pellet was resuspended in 1 ml of FACS buffer (0.5% FBS in PBS) and incubated with 1 µg of allophycocyanin (APC)-conjugated anti-mouse CD31 (PECAM-1), CD45, Ter119, Tie2 (CD202b) or EpCam (CD326) antibodies (BioLegend) and eFluor660-conjugated anti-mouse Lyve-1 antibody (Thermo Fisher) on ice for 30 min. A small aliquot of cells was incubated with the respective APC-conjugated isotype controls (BioLegend). After washing with 5 ml FACS buffer, the cell pellet were resuspended in 2 ml FACS buffer containing 1 µl of Sytox blue (Thermo Fisher). The cells were sorted on a BD FACSAria III cell sorter with a 100-µm nozzle. The viable (Sytox blue⁻), lineage-negative cells (Lin⁻: CD31⁻, CD45⁻, Ter119⁻, Tie2⁻, EpCam⁻, Lyve-1⁻) were sorted into ENFs (Lin⁻RFP⁺GFP⁻) and EPFs (Lin⁻RFP⁻GFP⁺) based on RFP and GFP fluorescence.

The following cell surface antibodies were used in the flow cytometric analysis: anti-mouse CD105-PE-Vio770 (Miltenyi), CD146-PerCP-Vio700 (Miltenyi), CD140a (pdgfra)-PE-Vio770 (Miltenyi), integrin α -APC (Miltenyi); and anti-mouse Sca1-PerCP-Cy5.5 (eBioscience), CD29-PerCP-eFluor710 (eBioscience).

Splinted wounds on adult mice. Splinting rings were prepared from a 0.5-mm silicone sheet (CWS-S-0.5, Grace Bio-Labs) by cutting rings with an outer diameter of 12 mm and an inner diameter of 6 mm. After washing with detergent and rinsing with water, the splints were sterilized with 70% ethanol for 30 min and air dried in a cell culture hood and kept in a sterile bottle.

Mice were anaesthetized with 100 µl MMF (medetomidine, midazolam and fentanyl). Dorsal hair was removed by a hair clipper (Aesculap Schermaschine Exacta), followed by hair removal cream for 3–5 min. Two full-thickness excisional wounds were created with a 5-mm diameter biopsy punch (Stiefel). One side of a splint was applied with silicone elastomer super glue (Kwik-Sil Adhesive, World Precision Instruments) and placed around the wound. The splint was secured with 5 sutures of 6.0 nylon, and the wound was covered with Tegaderm transparent dressing (3M). Mice were recovered from anaesthesia with an MMF antagonist and were supplied with metamizol (500 mg metamizol/ 250 ml drinking water) as postoperative analgesia.

Cell transplants. Sorted cells were washed with PBS and resuspended in PBS at 4 × 10⁶ cells per ml and mixed with an equal volume of ice-cold Matrigel (growth factor reduced, phenol red free) (356231, Corning) to obtain EPF and ENF suspensions in Matrigel at a final concentration of 2 × 10⁶ cells per ml, and stored on ice until injection for transplantation. The *Rag2^{-/-}* mice at 10–12 weeks of age were used as recipients of transplanted EPFs and ENFs. Two 5-mm diameter full-thickness excisional wounds were created on the back-skin of SCID mice as described above. Then, two injections of 50 µl of prepared EPF–Matrigel or ENF–Matrigel solution at a concentration of 2 × 10⁶ cells per ml were made intradermally around each wound, which resulted in intradermal transplantation of 2 × 10⁶ EPFs or ENFs to each wound. Control wounds received two intradermal

injections of 50 µl PBS. Fifteen minutes after injection, the silicone splints were applied and fixed around the wounds as described above. Scar tissues were harvested 14 days post-wounding and fixed with 2% paraformaldehyde at 4°C overnight. After washing three times with PBS, the tissues were processed for histology as described below.

Transplantation of decellularized skin. The dorsal skin of C57BL/6J mice (age P5) were subjected to decellularization as described previously²⁶. Briefly, the skin tissue was incubated sequentially with: (1) distilled water containing 0.1% Triton X-100 and 5× penicillin/streptomycin at 4°C for 24 h with stirring, (2) distilled water containing 2% sodium deoxycholate at 4°C for 24 h with stirring, (3) distilled water containing 1 M NaCl, 5× penicillin/streptomycin at room temperature for 1 h, and finally, (4) distilled water containing 30 µg ml⁻¹ porcine pancreatic DNase, 1.3 mM MgSO₄, 2 mM CaCl₂ and 5× penicillin/streptomycin at room temperature for 1 h. The decellularized skin was stored in PBS at 4°C until transplantation. Two 5-mm diameter full-thickness excisional wounds were created on the dorsal back of each recipient *Rag2^{-/-}* mouse. A 5-mm diameter biopsy of decellularized donor skin was transplanted to the recipient's wound with silicone elastomer super glue (Kwik-Sil Adhesive, World Precision Instruments). Wounds without a transplant served as control. Subsequently, the wounds were covered with a 12-mm diameter silicone sheet (Grace Bio-Labs), fixed with 5 sutures, and transparent dressing was applied (3M Tegaderm Film). The scar tissues were harvested 10 days post-wounding and processed for histology.

Ex vivo wounding. E12.5 embryos were harvested from *En1^{Cre};R26^{mTmG}* breeding. Cre⁺ embryos were selected based on GFP positivity by observing them under a fluorescence stereomicroscope (Leica M205 FA). Small excisional wounds were created on the dorsal back of embryos by using fine microsurgical scissors (Vannas Spring Scissors, Fine Science Tools) under the stereomicroscope (Leica M50). The embryos were kept in Knockout DMEM (Thermo Fisher) supplemented with 10% KnockOut Serum Replacement (Thermo Fisher), 1% penicillin/streptavidin (Thermo Fisher), 1% GlutaMAX (Thermo Fisher) and 1% Non-Essential Amino Acids solution (Thermo Fisher) in a 37°C, 5% CO₂ incubator. Embryos were fixed with 2% paraformaldehyde at 12 h, 24 h and 48 h after culture and processed for histology.

Ex vivo tamoxifen treatment. E12.5 embryos were harvested from *Actin^{Cre-ER};R26^{VT2/GK3}* breeding. The embryos were kept in Knockout DMEM supplemented with 10% KnockOut Serum Replacement, 1% penicillin/streptavidin, 1% GlutaMAX, 1% Non-Essential Amino Acids solution and 1 nM 4-hydroxytamoxifen (Sigma-Aldrich) in a 37°C, 5% CO₂ incubator. Twenty-four hours later, embryos were fixed overnight with 2% paraformaldehyde at 4°C and processed for histology.

Histology. Tissue samples were fixed overnight with 2% paraformaldehyde in PBS at 4°C. Samples were rinsed three times with PBS, embedded in optimal cutting temperature (OCT) compound (Sakura Finetek) and flash-frozen on dry ice. Six µm sections were made in a Hyrax C50 Zeiss Cryostat.

Masson's trichrome staining was performed with a Sigma-Aldrich Trichrome stain kit, according to the manufacturer's instructions.

For immunostainings, sections were air dried for 5 min followed by fixation with -20°C-chilled Acetone for 20 min. Sections were rinsed three times with PBS and blocked for 1 h at room temperature in PBS plus 5% serum. Then, the sections were incubated with the primary antibody in PBS serum overnight at 4°C or for 90 min at room temperature. Sections were then rinsed three times with PBS and incubated with the secondary antibody in PBS serum for 60 min at room temperature. Finally, sections were rinsed three times in PBS and mounted with fluorescent mounting media with 4,6-diamidino-2-phenylindole (DAPI).

TUNEL (Life technologies) staining was performed prior to immunolabelling according to the manufacturer's recommendations but avoiding proteinase K treatment.

Antibodies used: Ki67 (Abcam), Cas3 (Cell Signaling), collagen I (Rockland), fibronectin (Abcam), FSP1 (Abcam), collagen III (Abcam), collagen VI (Abcam), CD31 (Novus Biologicals), α -SMA (Abcam), CD26 (Abcam), TNC (Abcam), Dlk1 (Abcam), Sca1 (Biolegend), FABP4 (Abcam) and AF647 secondary antibody (Molecular Probes).

Live imaging. Pregnant mice were killed 12.5 d.p.c. (days post-coitum) by cervical dislocation and uteri were excised. Embryos were dissected in ice-cold medium and tested for Cre⁺ fluorescence. Excised Cre⁺ embryos were incubated with SiR-DNA (Spirochrome) for 1 h (at 37°C with 5% CO₂). The embryos were embedded in 35-mm glass bottom dishes (Ibidi) and Matrigel (Corning) and the gel was allowed to solidify for 30 min. Imaging medium (DMEM/F-12; SiR-DNA 1:1,000) was then added. Twenty-four-hour time-lapse imaging was performed using a Zeiss LSM 710, equipped with 488-nm, 515-nm and 633-nm laser lines and a ×20 objective. Temperature control was set to 37°C with 5% CO₂-supplemented air. Three channels (GFP, tdTomato and AF647) were recorded every 15 min as a z-stack of 188-µm thickness. The 4D data were processed with Imapris 9.1.0 (Bitplane) and ImageJ. Contrast and brightness were adjusted for better visibility.

Cell tracking. 3D drift correction was applied on the live-imaging 4D data using the ImageJ's Correct 3D Drift⁷ in reference to the EPF channel. The resultant drift-corrected data sets were subjected to maximum intensity projection and visualized to verify compensation of the apparent drift in reference to the imaging plane. The corrected data sets were subjected to cell migration and cell-tracking analysis using 'Trackmate'. Variables, such as blob diameter, threshold, detector (Laplacian of Gaussian (LoG) segmentation) and the LAP (linear assignment problem) tracker, were adjusted to suit the nature of the data and the samples as described in the plugin workflow²⁷. Filters, such as spots with good quality, mean intensity and uniform colour, were applied and tracked using the LAP Tracker. Individual track information and the coordinates of these data points were exported as an Excel file. Graphical representation and visualization of 4D data sets were performed using a R script in the 'scatterplot3D' package to represent the tracks on a 3D plane. For the fourth dimension of the tracks, colour ramp was applied to the individual tracks as a function of time (blue, first time point; red, last time point of the track). To visualize the data points on a 3D interactive space (360° rotation and zoom function), the R package 'rgl: 3D visualization using OpenGL' was integrated into the script.

3D imaging. Samples were fixed in 2% paraformaldehyde at 4 °C overnight and imaged in a 35-mm glass-bottom dish (Ibidi).

Cleared samples were processed using a modified 3Disco protocol. In short, samples were stained with anti-GFP (Abcam) and anti-RFP (SIGGEN) for 4 days, followed by incubation with AF488 and AF647 secondary antibodies (Molecular Probes) for 2 days. Clearing was performed after dehydration in an ascending tetrahydrofuran (Sigma) series, with 30-min incubation in dichloromethane (Sigma) and eventually with immersion in dibenzyl ether (Sigma). Imaging was performed in dibenzyl ether with an inverted confocal (LSM 710, Zeiss) using a ×10 or ×20 objectives. Stacks were recorded in the green and far-red channels. 3D visualization and recording of movies were performed using Imaris 9.1.0 (Bitplane).

Image analysis. Single ×10 or ×63 images were taken of the EPF-containing anterior and posterior fields, in the same section, using a confocal LSM 710 (Zeiss).

Image processing and analysis were performed with ImageJ (ImageJ 1.47 (ref. 28)). For separating EPF and ENF fluorescent signals, only the red population of EPFs was analysed from sections from 'Rainbow' mouse, as it provided the strongest signal. Channels from the raw images were split, the background was subtracted (rolling ball radius = 50 pixels) and contrast was enhanced (pixel saturation = 0.1, normalized). The 'unsharp mask' and 'median' filters were applied (radius = 10, mask = 0.60; and radius = 1, respectively). The auto-threshold method 'Yen' was used to make binary images except for the immunostaining signal of fibronectin and collagen I, for which 'default' method was used. To avoid the inclusion of background signal into the analysis, the pixels from the ENF signal were subtracted from the EPF signal and vice versa using the image calculator function. For segmentation of the blue colour from trichrome stains, ×10 bright-field images were taken with a vertical Axio scope (Zeiss). Images were transformed into CMYK and only the cyan channel was used for further separation, the background was subtracted (rolling ball radius = 20 pixels) and contrast was enhanced (pixel saturation = 0.1, normalized). The 'unsharp mask' and 'median' filters were applied (radius = 2, mask = 0.60; and radius = 1, respectively). The auto-threshold method 'Moments' was used to make binary images, and the 'despeckle' function was used to avoid the inclusion of the background signal into the analysis.

Fractal analysis was performed using the ImageJ plug-in 'FracLac'²⁹ (FracLac 2015Sep090313a9390). FD values were calculated using the box counting scan (20 slipping and tighten grids at default sampling sizes, minimum pixel density threshold = 0.40). L values were calculated using the sliding box scan (slipping and tighten grid at default sampling sizes, minimum pixel density threshold = 0.40). Local FD and L values were calculated using the subsample scan (1 grid at default sampling size, minimum pixel density threshold = 0.40, subscan in rectangles). Individual values within the discernible distinct dermal layers were manually pooled.

For the collagen I intensity analysis, sections of *En1^{Cre};R26^{VT2/GK3}* embryos at different stages were immunostained for collagen I. ×63 images were segmented as before. Segmented EPF and ENF binary images were further processed (Options: Process_Binary_Fill Holes, and Process_Binary_Close) and a region of interest selection was created to measure the mean grey values from the raw images. The mean grey values from the region of interest were normalized with the general mean grey values of the image. Three images from every condition were analysed.

For the fibronectin fibre distance measurements, sections of *En1^{Cre};R26^{VT2/GK3}* embryos at different stages were immunostained for fibronectin. ×63 images were segmented as before. We used the plot profile function in diagonal lines of fibronectin segmented images, and the distance between the fibres was calculated as the gaps between the signal peaks. Three images from every condition were analysed.

Statistics and reproducibility. Statistical analyses were performed using GraphPad Prism software (version 6.0, GraphPad). Statistical significance was determined using Student's *t*-test or analysis of variance (ANOVA) with Tukey, Holm–Sidak or Newman–Keuls multiple comparison test, as indicated in the corresponding figure legends. All experiments presented in the manuscript were repeated in at least three independent experiments/biological replicates with similar results, unless indicated otherwise in the figure legend. Cell-tracking data shown in Fig. 3 were derived from 144 high-quality tracks of one representative video. Fig. 7 was derived from two independent transplantation experiments of mock control, EPFs, ENFs and decellularized skin.

Reporting Summary. Further information on experimental design is available in the Nature Research Reporting Summary linked to this article.

Data availability. Source data for Figs. 1, 4, 5 and 7 and Supplementary Figs. 3 and 5 have been provided as Supplementary Table 1. All other data supporting the findings of this study are available from the corresponding author on reasonable request.

References

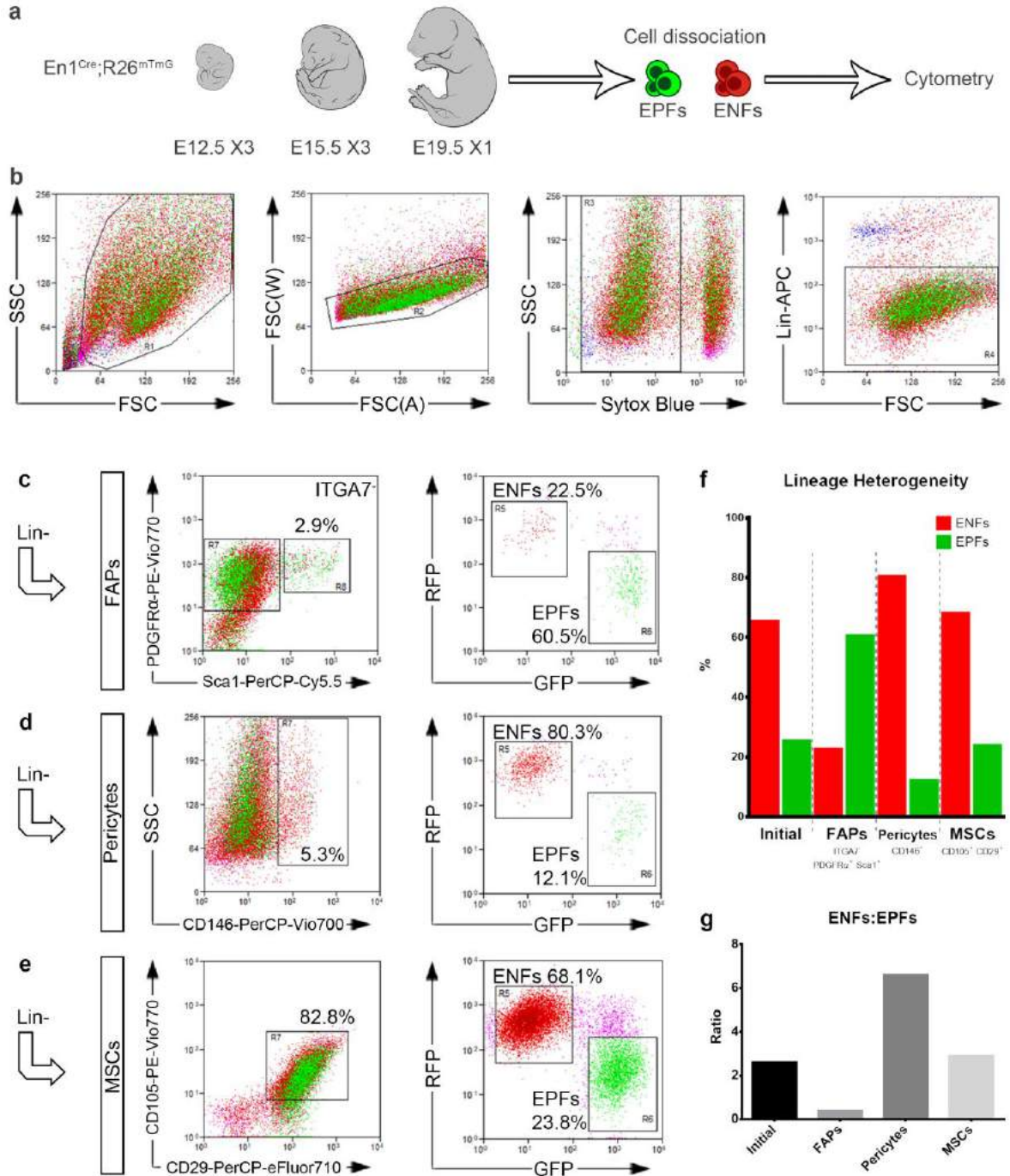
26. Bonenfant, N. R. et al. The effects of storage and sterilization on de-cellularized and re-cellularized whole lung. *Biomaterials* **34**, 3232–3245 (2013).
27. Parslow, A., Cardona, A. & Bryson-Richardson, R. J. Sample drift correction following 4D confocal time-lapse imaging. *J. Vis. Exp.* **86**, 51086 (2014).
28. Schneider, C. A., Rasband, W. S. & Eliceiri, K. W. NIH image to ImageJ: 25 years of image analysis. *Nat. Methods* **9**, 671–675 (2012).
29. Karperien, A. *FracLac for ImageJ*. 1999–2013; <http://rsb.info.nih.gov/ij/plugins/fractal/FLHelp/Introduction.htm>

In the format provided by the authors and unedited.

Two succeeding fibroblastic lineages drive dermal development and the transition from regeneration to scarring

Dongsheng Jiang^{1,5}, Donovan Correa-Gallegos^{1,5}, Simon Christ^{1,5}, Ania Stefanska¹, Juan Liu¹, Pushkar Ramesh¹, Vijayanand Rajendran¹, Martina M. De Santis^{1,2,3}, Darcy E. Wagner^{1,2,3,4} and Yuval Rinkevich^{1,4*}

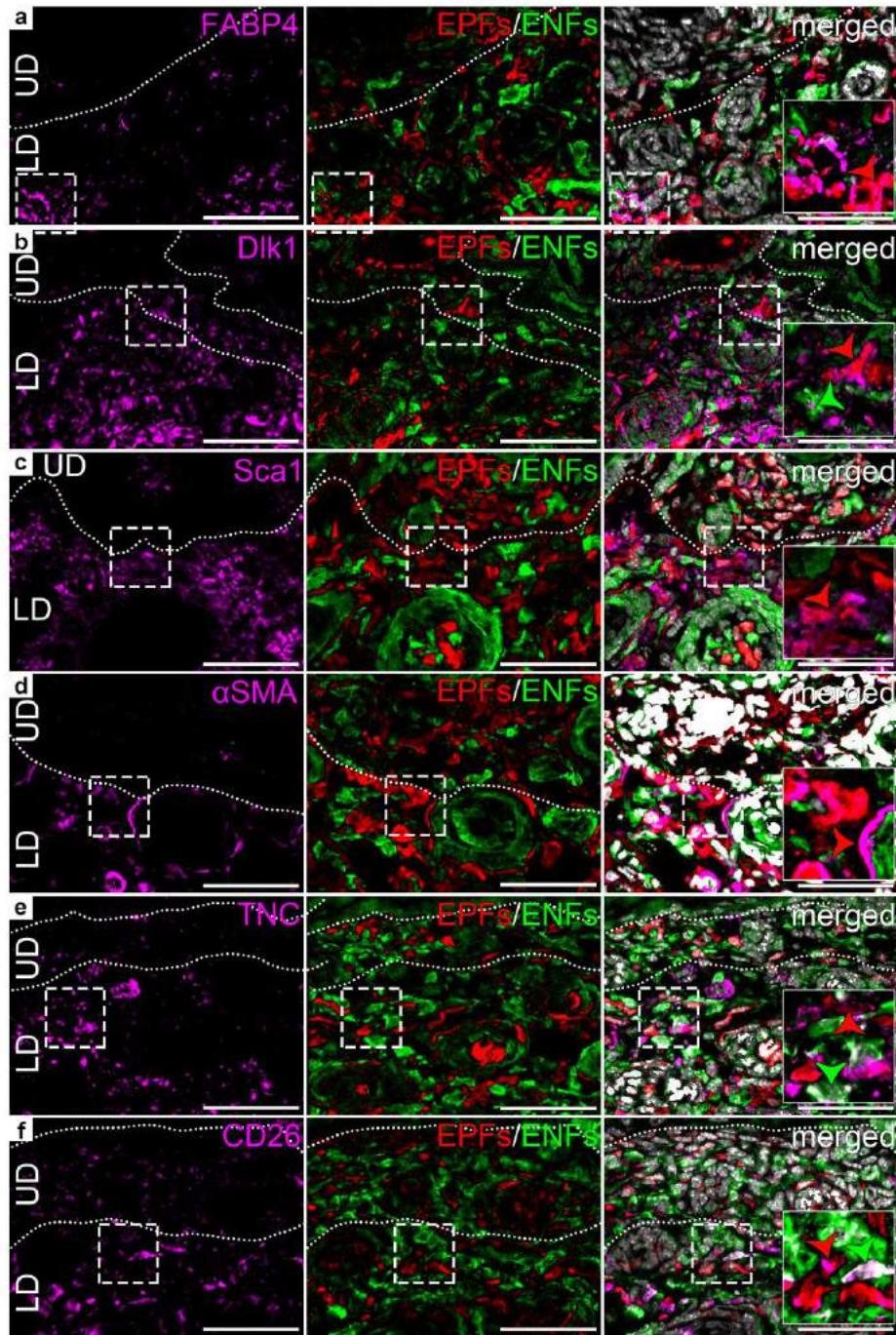
¹Comprehensive Pneumology Centre/Institute of Lung Biology and Disease, Helmholtz Zentrum München, Munich, Germany. ²Department of Experimental Medical Sciences, Lund University, Lund, Sweden. ³Wallenberg Centre for Molecular Medicine, Lund University, Lund, Sweden. ⁴Member of the German Centre for Lung Research (DZL), Munich, Germany. ⁵These authors contributed equally: Dongsheng Jiang, Donovan Correa-Gallegos and Simon Christ. *e-mail: yuval.rinkevich@helmholtz-muenchen.de



Supplementary Figure 1

Flow cytometric analysis of mesenchymal markers on ENFs and EPFs.

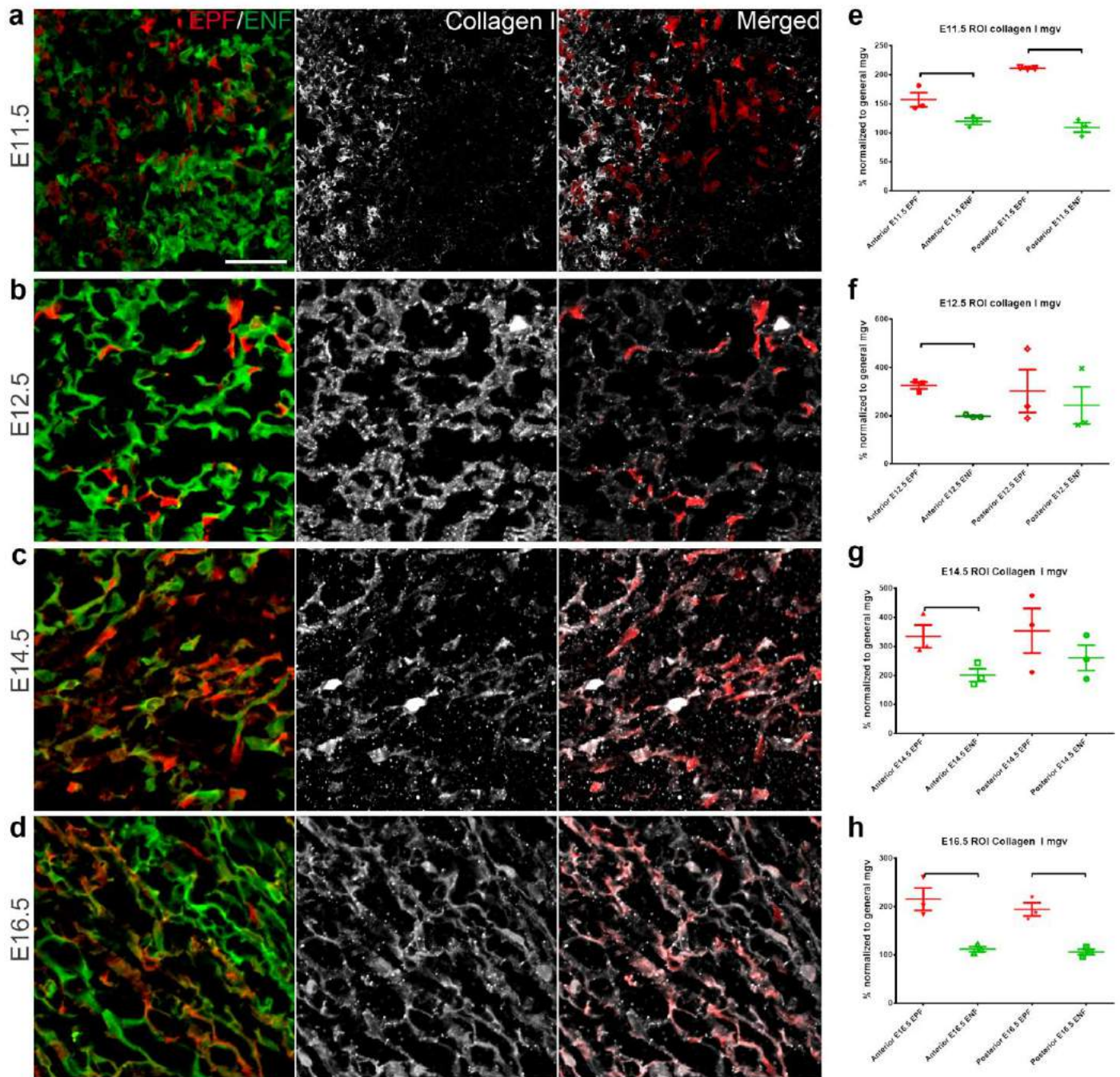
a, single cell suspension was prepared from the pooled back-skin from three E12.5, three E15.5 and one E19.5 *En1^{Cre};R26^{mTmG}* embryos, and subjected to flow cytometric analysis. **b**, Sytox blue was used to exclude dead cells, and APC-conjugated lineage markers (CD45, CD31, Ter119, EpCAM, Tie-2, Lyve-1) were used to exclude non-mesenchymal cells. **c-e**, representative analysis plots of fibro-adipogenic progenitors (FAPs) (Lin⁻ITGA7⁺Sca1⁺PDGFR α ⁺) (c), pericytes (Lin⁻CD146⁺) (d), and mesenchymal stem cells (Lin⁻CD29⁺CD105⁺) (e), and their distributions in ENFs and EPFs. **f-g**, the percentages of ENFs and EPFs (f) and the ratio of ENFs:EPFs (g) within Lin⁻ cells (initial), FAPs, pericytes and MSCs.



Supplementary Figure 2

Expression of mesoderm markers on ENFs and EPFs by immunofluorescence staining.

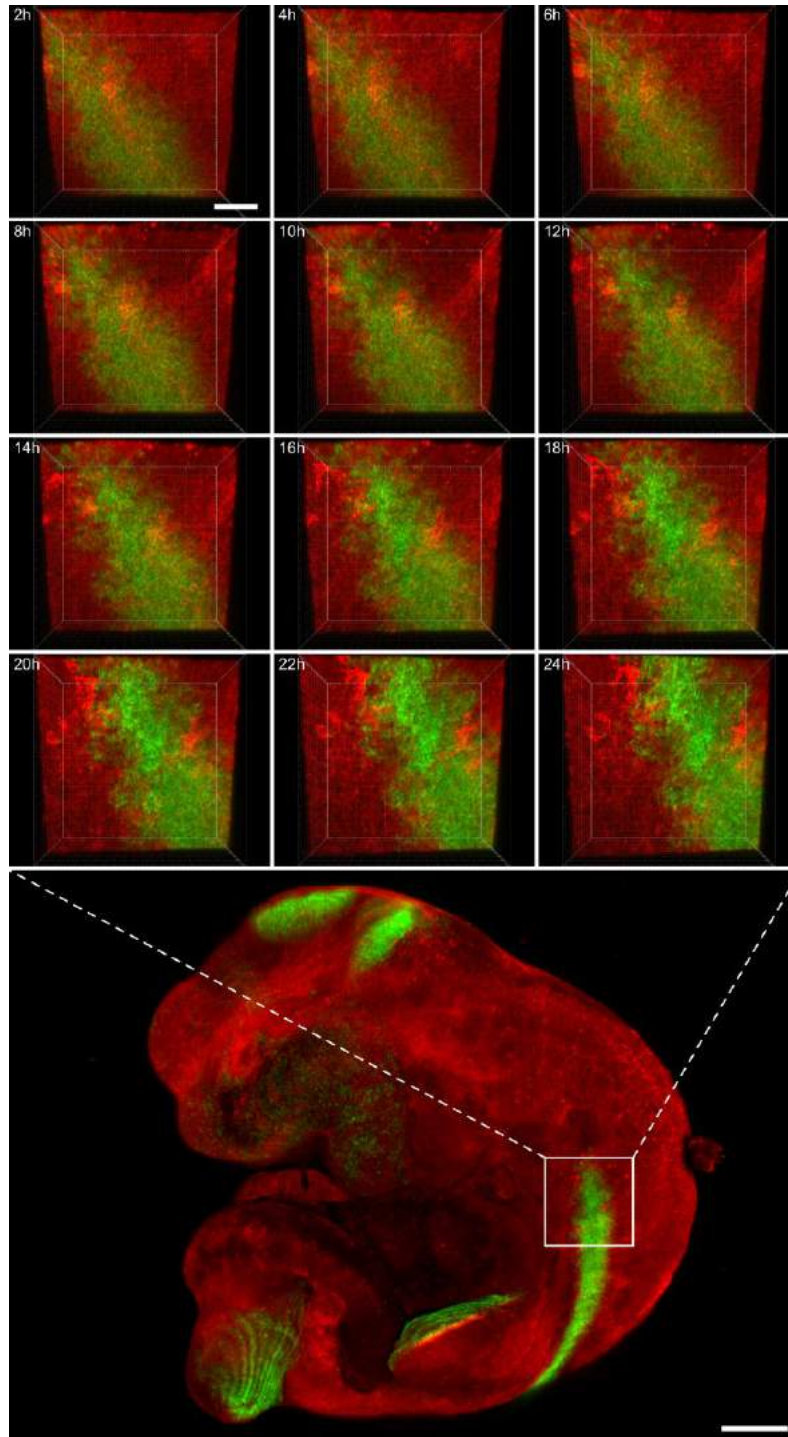
Cryosections were prepared from *En1^{Cre};R26^{VT2/GK3}* neonates (P1), and stained with primary antibodies against mouse FABP4 (a), Dlk1 (b), Sca1 (c), α SMA (d), TNC (e), and CD26 (f), and AF647-conjugated respective secondary antibodies. Depicted are representative high-power images of AF647 channel for antibodies (left), GFP-RFP channels for ENFs-EPFs (middle), and merged channels (right). Dotted lines indicate the border of epidermis and dermis, and the border of upper dermis (UD) and lower dermis (LD). Squares indicate the locations of enlarged inserts in merged images. Scales: 50 μ m. The depicted are representative images of three individual embryos.



Supplementary Figure 3

EPFs associate with Collagen I fibers.

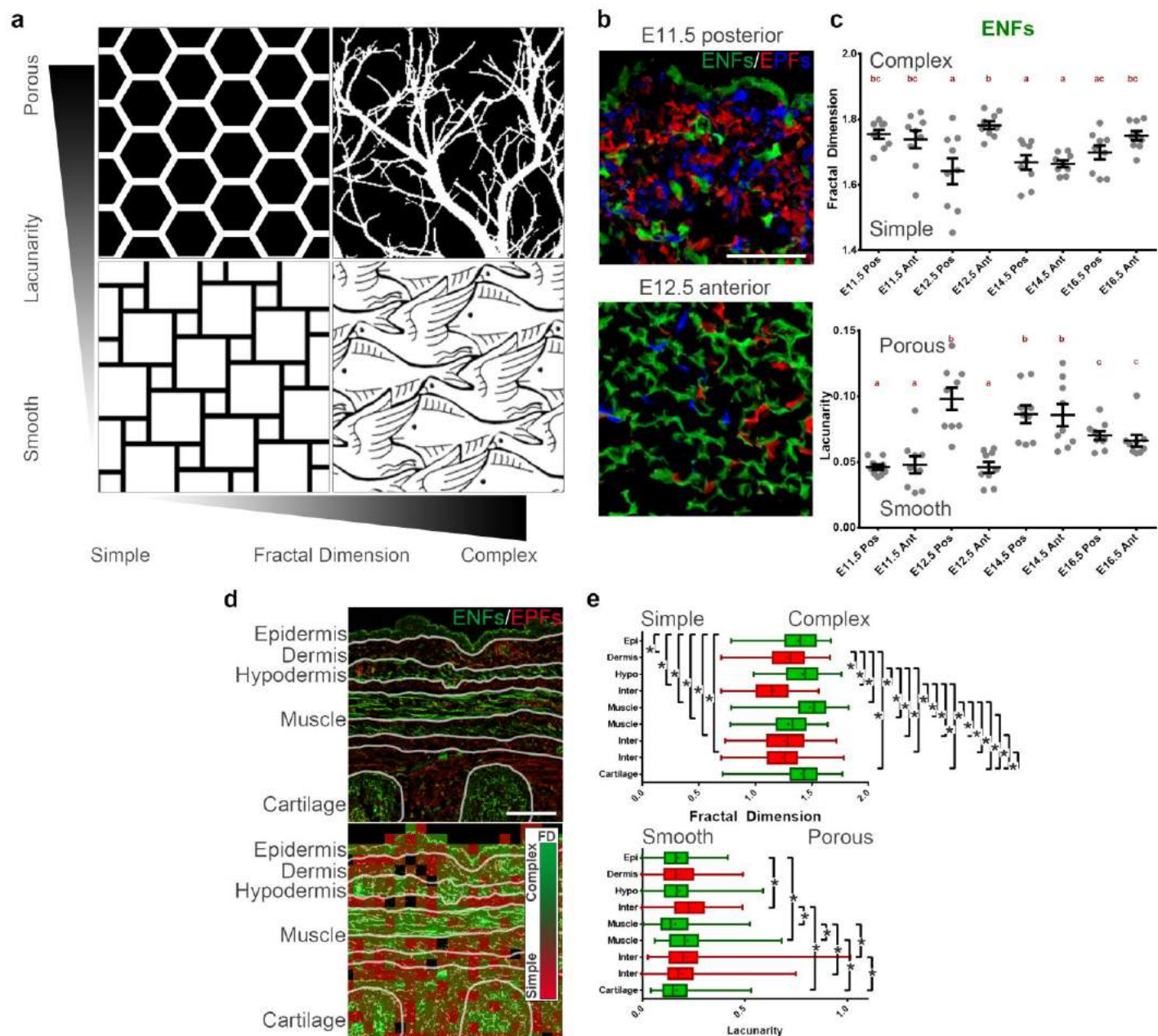
a-d, Immunofluorescence for Collagen I of E11.5 (a), E12.5 (b), E14.5 (c), or E16.5 (d) *En1^{Cre};R26^{VT2/GK3}* embryos. e-h, EPF- or ENF-signal-derived ROI mean grey value (mgv) \pm SEM of the Collagen I signal from anterior or posterior regions of E11.5 (e), E12.5 (f), E14.5 (g), or E16.5 (h) *En1^{Cre};R26^{VT2/GK3}* embryos. n = 3 optical fields of anterior and posterior regions at each development stage. Two-tailed unpaired *t*-test. * $p < 0.05$. Scale: 50 μ m. Images represent 1 out of three optical fields. The exact p values are listed in Supplementary Table 1.



Supplementary Figure 4

EPFs actively displace provisional ENF dermis.

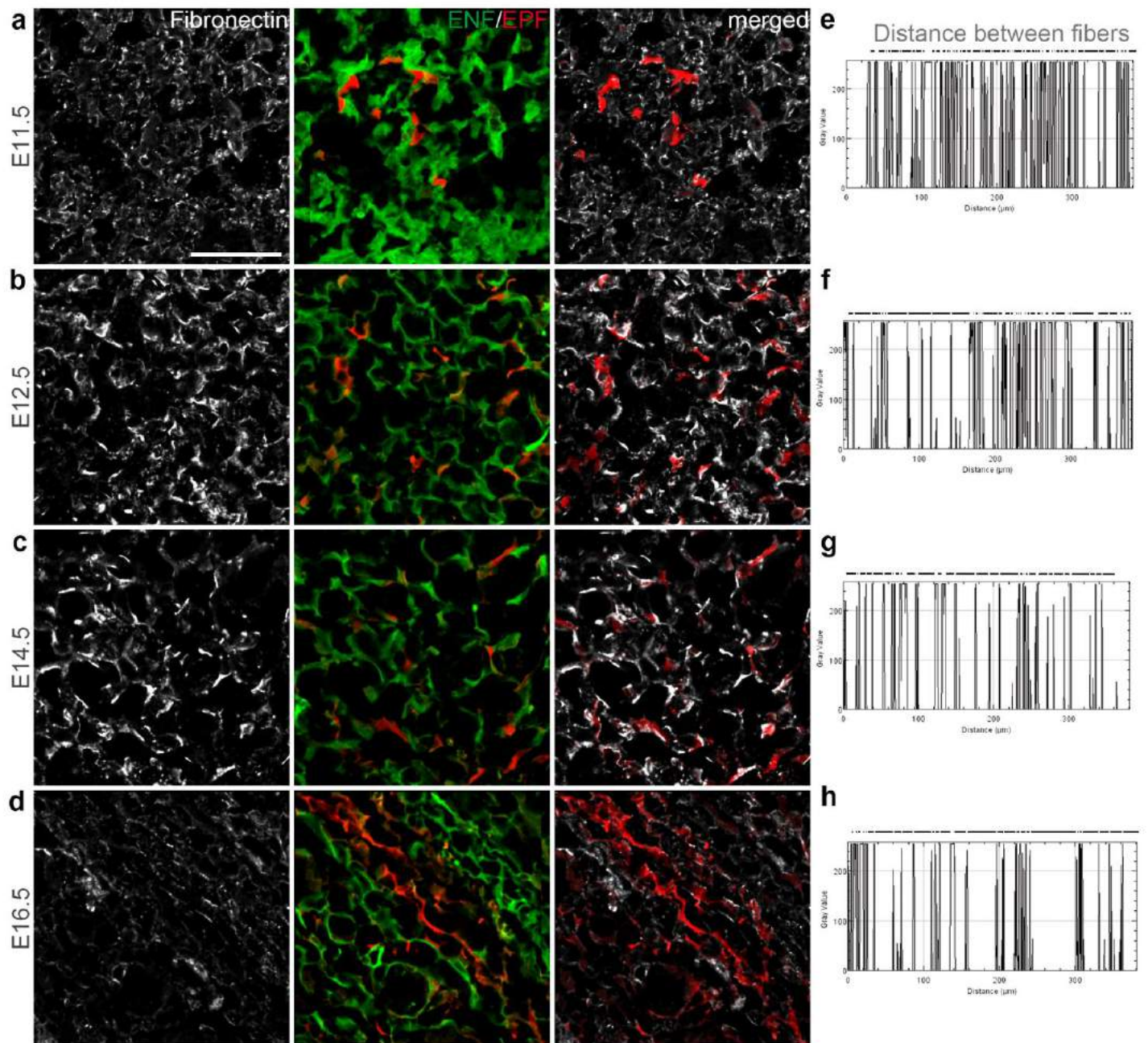
3D representations of 24 h time-lapse images of EPF-positive anterior region in E12.5 *En1^{Cre};R26^{mTmG}* embryo (up). Max projection of whole live embryo showing the area analyzed (down). Scales: 100 μm and 500 μm , respectively. Images are taken from the one representative video used for cell tracking analysis showed in Figure 3.



Supplementary Figure 5

Fractal analysis of ENFs organizations during development. and subsampled fractal analysis.

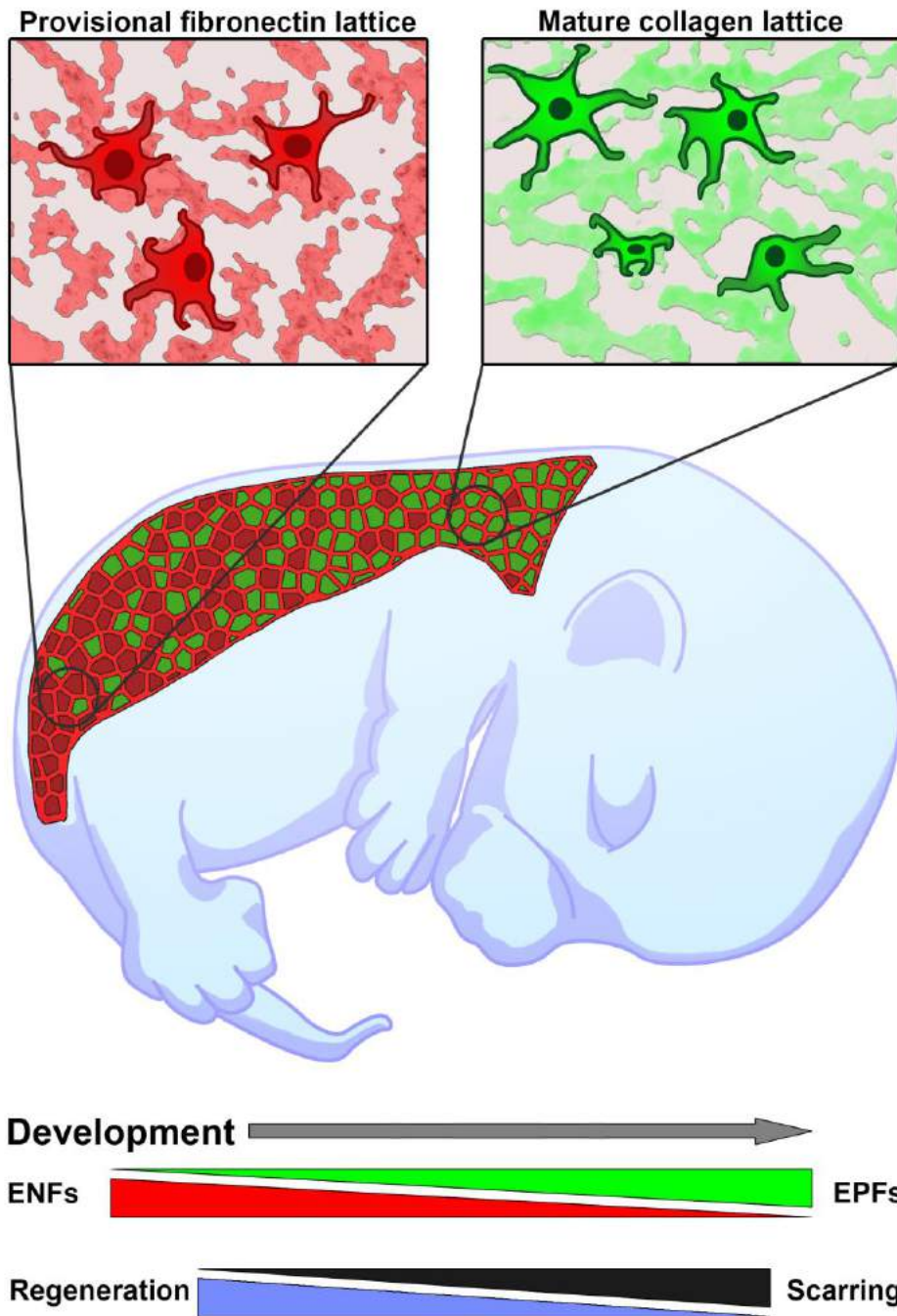
a, Graphical representation of the quantitative assessment of complexity and porosity in 2D images by Fractal analysis. **b**, Representative confocal images of clumped posterior E11.5 EPFs (up), and stretched anterior E12.5 (down) from *En1^{Cre},R26^{VT2/GK3}* embryos. **c**, Fractal dimension (up) and lacunarity (down) values derived from ENFs of different regions and developmental stages. Mean \pm SEM. $n = 9$ optical fields of anterior or posterior regions at each developmental stage. RM ANOVA, $p < 0.05$, Newman-Keuls test. **d**, Subsampled (local) fractal analysis (right) of low-power magnification confocal images of E16.5 *En1^{Cre},R26^{VT2/GK3}* embryos (left). Scale: 50 μm . **e**, Fractal dimension (up) and lacunarity (down) values derived from ENFs of different regions and developmental stages, $n > 60$ subsampled values pooled from three confocal images. ANOVA, Tukey test, $*p < 0.05$. Box and whiskers plots with minimum, lower quartile, median, upper quartile, and maximum. The exact p values are listed in Supplementary Table 1.



Supplementary Figure 6

Fibronectin matrix stiffens concurrent with EPF expansion.

a-d, Immunofluorescence for Fibronectin in E11.5 (a), E12.5 (b), E14.5 (c), or E16.5 (d) *En1^{Cre};R26^{VT2/GK3}* embryos. e-h, Representative linear profiles of diagonal lines on the Fibronectin signal from E11.5 (e), E12.5 (f), E14.5 (g), or E16.5 (h) images. Dashed lines above the plots represent the calculated distances between fibers. Scale: 50 μm. Images are representatives of 3 optical fields.



Supplementary Figure 7

The fibroblastic lineage replacement drives the transition of dermal response to injury from regeneration to scarring.

ENFs are the primary sculptors that drive dermal lattice development and regeneration during early development, and that their cell lineage declines during development. EPFs that produce mature matrix fibres expand concurrently, and predispose back-skin to scarring.

Publication II

Jiang D, Christ S, Correa-Gallegos D, Ramesh P, Kalgudde Gopal S, Wannemacher J, Mayr C, Lupperger V, Yu Q, Ye H, Mück-Häusl M, Rajendran V, Wan L, Liu J, Mirastschijski U, Volz T, Marr C, Schiller HB & Rinkevich Y. Injury triggers fascia fibroblast collective cell migration to drive scar formation through N-cadherin. *Nat Commun* **11**, 5653 (2020).

<https://doi.org/10.1038/s41467-020-19425-1> ***First author with equal contribution**







The above study is a result of my contribution as a “shared-first author” or “first-author with equal contribution”. This is a result of a merger of projects dealing with a) development of SCAD methodology by co-first authors Jiang D and Christ S along with b) my and Correa-Gallegos D’s contribution to the mechanistic findings in the manuscript. By performing cell-cell adhesion molecule screens, we identified N-Cadherin as a principal molecule that drives EPFs in scar development. Using a combination of novel imaging, gene-editing and viral transduction approaches we validated these mechanistic findings. These novel findings play a pivotal role in the manuscript to elucidate the relevance of SCAD model in studying *bona fide* scars. Further, my contributions are also explicitly described in the “authors’ contribution” section of the published article.

This includes my contribution to the development of SCAD assay (minor), **major or principal contribution** in 3-D and 3-D time-lapse multiphoton imaging, computational cell tracking, adhesion molecule identification, intra-vital vector field analysis, 3-D contour cell trajectory analysis, SCAD chimera generation, N-Cadherin inhibition experiments, mass production of AAV6-NcadgRNA-GFP, AAV6-Cre-GFP and AAV6-GFP viral particles. Finally, I contributed to the narrative for the mechanistic part of the manuscript along with the relevant figures and texts.

In particular:

- a) Figure 1 e, f and g: Iterative particle image velocimetry analysis , intra-vital vector field analysis and contour trajectory analysis of intra-vital wounding data
- b) Figure 3 e: EPF and WPF enrichment analysis in scar
- c) Figure 4 a, b, c, e : Adhesion marker screening, N-Cadherin adhesion molecule identification and peptide inhibition experiments using Exherin
- d) Figure 5 a and b : AAV generation and co-localization analysis of N-cadherin knockdown efficiency in *in-vivo* wounds
- e) Supplementary figures 3a, 4a-f , 5b , 7b-h: 3-D immunostaining, multiphoton imaging, and exherin knockdown experiments
- f) Supplementary figure 6d: Establish and generation of chimeric SCAD assay and 3-D time-lapse multiphoton imaging
- g) Supplementary figure 10a and c- Mass production and titration of AAV6-NcadgRNA-GFP, AAV6-GFP viral constructs for *in-vivo* validation experiments

Injury triggers fascia fibroblast collective cell migration to drive scar formation through N-cadherin

Dongsheng Jiang ^{1,8}, Simon Christ ^{1,8}, Donovan Correa-Gallegos^{1,8}, Pushkar Ramesh^{1,8}, Shruthi Kalgudde Gopal¹, Juliane Wannemacher¹, Christoph H. Mayr², Valerio Lupperger³, Qing Yu¹, Haifeng Ye¹, Martin Mück-Häusl¹, Vijayanand Rajendran¹, Li Wan¹, Juan Liu¹, Ursula Mirastschijski^{4,5}, Thomas Volz⁶, Carsten Marr ³, Herbert B. Schiller ^{2,7} & Yuval Rinkevich ^{1,7} 

Scars are more severe when the subcutaneous fascia beneath the dermis is injured upon surgical or traumatic wounding. Here, we present a detailed analysis of fascia cell mobilisation by using deep tissue intravital live imaging of acute surgical wounds, fibroblast lineage-specific transgenic mice, and skin-fascia explants (scar-like tissue in a dish - SCAD). We observe that injury triggers a swarming-like collective cell migration of fascia fibroblasts that progressively contracts the skin and form scars. Swarming is exclusive to fascia fibroblasts, and requires the upregulation of N-cadherin. Both swarming and N-cadherin expression are absent from fibroblasts in the upper skin layers and the oral mucosa, tissues that repair wounds with minimal scar. Impeding N-cadherin binding inhibits swarming and skin contraction, and leads to reduced scarring in SCADs and in animals. Fibroblast swarming and N-cadherin thus provide therapeutic avenues to curtail fascia mobilisation and pathological fibrotic responses across a range of medical settings.

¹Helmholtz Zentrum München, Institute of Lung Biology and Disease, Group Regenerative Biology and Medicine, Munich, Germany. ²Helmholtz Zentrum München, Institute of Lung Biology and Disease, Group Systems Medicine of Chronic Lung Disease, Munich, Germany. ³Helmholtz Zentrum München, Institute of Computational Biology, Munich, Germany. ⁴Mira-Beau gender esthetics, Berlin, Germany. ⁵Wound Repair Unit, CBIB, Faculty of Biology and Biochemistry, University of Bremen, Bremen, Germany. ⁶Department of Dermatology and Allergology, Technical University of Munich, School of Medicine, Klinikum rechts der Isar, Munich, Germany. ⁷German Centre for Lung Research (DZL), Munich, Germany. ⁸These authors contributed equally: Dongsheng Jiang, Simon Christ, Donovan Correa-Gallegos, Pushkar Ramesh. ✉email: yuval.rinkevich@helmholtz-muenchen.de

Organisms such as planaria, hydra, zebrafish and certain amphibians, are able to fully regenerate tissues and organs upon injury with minimal scarring. However, the global mammalian and human response to injury is scarring and contraction over the wound. Scars replace the original connective tissue foundation with dense “plugs” of matrix fibres that tighten the tissue and reduce its flexibility^{1,2}. Scarring occurs both after accidental injuries and after surgery in over 100 million patients per year and particularly among children, one in five of whom require reconstructive surgery for scar-induced contracted joints^{2–5}. Scarring and impaired wound-healing are major clinical problems and a tremendous burden for patients and global healthcare systems, costing tens of billions of dollars per year in the US.

Whereas deep skin wounds trigger the subcutaneous fascia to form exuberant scars, there are rare examples where skin injuries culminate in scarless regeneration. Scarless regeneration is prevalent during foetal life as well as in certain anatomic locations such as the oral mucosa^{6,7}. The African spiny mouse (genus *Acomys*)⁸ is another rare example of a mammalian species that can regenerate skin wounds without scarring. Despite extensive study into scarring, the underlying mechanism of how scars emerge remains incompletely understood. Understanding this universal wound-repair event would allow us to control, restore and preserve the functions of physically damaged adult tissues and pave the way towards clinically regenerating severe skin injuries.

Recent studies have uncovered fibroblasts with distinct potencies based on their lineage origins in certain skin locations^{9–14}. For example, we found that fibroblasts with scar-forming potential coexist with “ordinary” fibroblasts in the adult back-skin^{12,13}. Scarring ability of fibroblasts is instilled during embryogenesis in cells with temporary early embryonic expression of the *Engrailed-1* gene. In adults the scar-forming and non-scar-forming fibroblasts are thus referred to as the embryonic “engrailed-past” and “engrailed-naive” fibroblasts, EPFs and ENFs, respectively. We recently found that subcutaneous fascia, a viscoelastic membranous sheet of matrix, that creates a thin gelatinous and frictionless interface between the skin and the body’s interior rigid structures, is the main anatomical contributor to exuberant scars that form following deep skin wounds⁹. We have shown that injury induces fascia mobilisation across the skin, and that fascia mobilisation repairs breaches in the structural continuums of the skin, thereby preserving skin integrity and function. It remains unclear why fascia EPFs are prone to form scars, whereas upper dermal or oral mucosa fibroblasts do not.

In this study, by using intravital probing into deep wounds of live mice and an ex vivo explant technique termed scar-like tissue in a dish (SCAD) coupled with genetically traceable scar-forming EPFs, we show that upon wounding fascia EPFs upregulate N-cadherin, which is required for the collective migration and subsequent swarming of fascia EPFs towards wound centre and drives scar formation. Blocking N-cadherin by peptide inhibitor or genetic modification reduces scarring.

Results

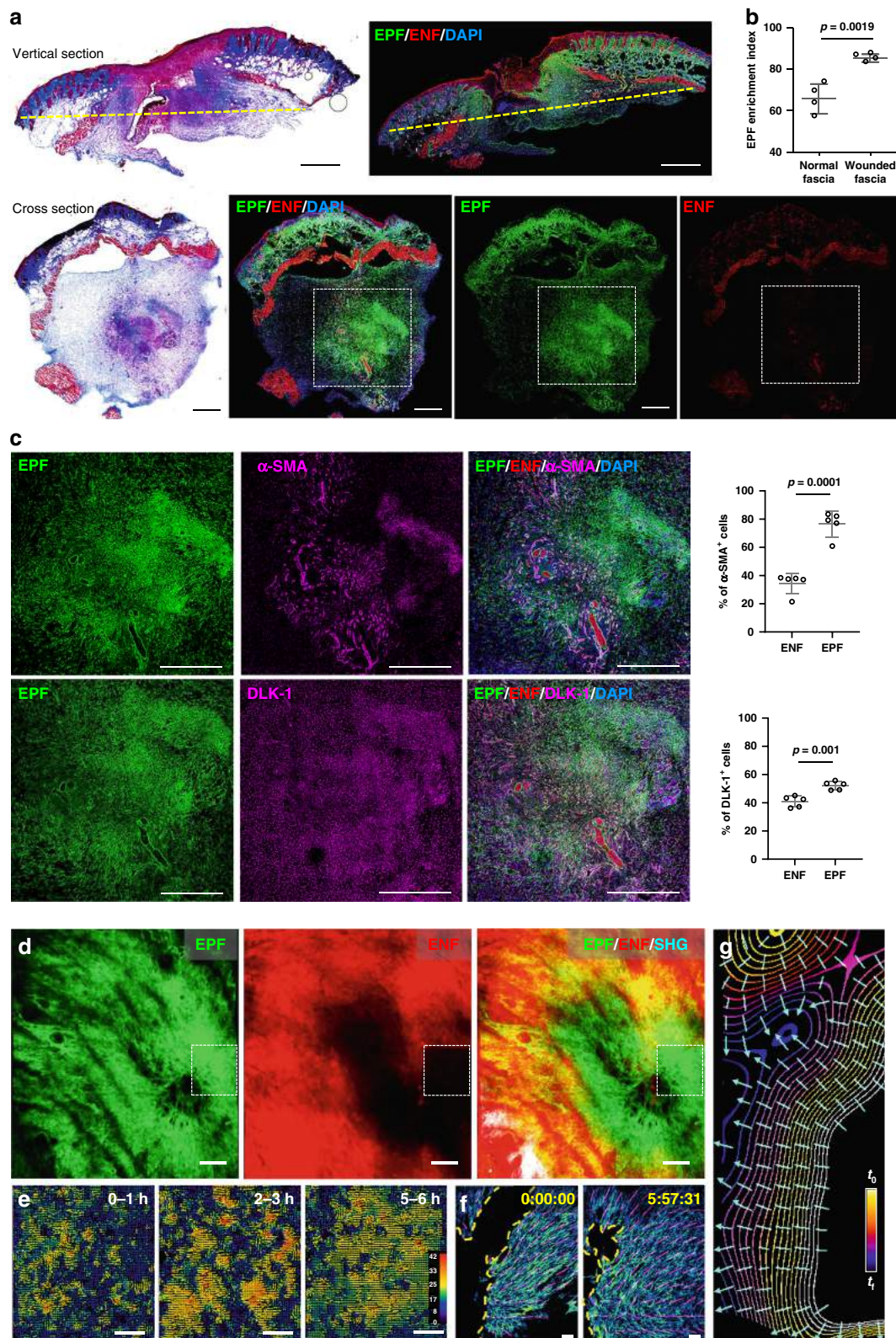
Collective migration of fascia EPFs in deep wounds. First, we looked into the composition of fascia fibroblasts during wound healing and scarring. We previously discovered that scars developed from a specific type of fibroblast that temporarily expressed *Engrailed-1* early in embryogenesis (termed EPFs). Whereas ENFs that have no history of *Engrailed-1* expression, do not contribute to scar formation in any way^{12,13}. We followed the fates of these two fibroblast lineages by crossing fibroblast lineage-specific promoter mice (*En1^{Cre}*) to mice (*R26^{mTmG}*) with a dual fluorescence reporter

that replaces membrane-bound tdTomato with membrane-bound green fluorescence protein (GFP) upon recombination. In all, 5-mm full-thickness excisional wounds were created on the back of *En1^{Cre};R26^{mTmG}* mice with biopsy punches. The excision went through the panniculus carnosus muscle and fascia completely. The wounds were splinted with silicone rings to minimise contraction and to allow healing through granulation and re-epithelialization, similar to human skin wounds. To zoom into subcutaneous fascia, we made transverse cross-section of wounds 7 days after wounding and examined the sections that were surrounded by panniculus carnosus of the adjacent normal skin. EPFs were clearly clustered at the wound centre (Fig. 1a), and were enriched from $65.6 \pm 6.2\%$ in uninjured subcutaneous fascia (Fig. 1b and Supplementary Fig. 1) to $85.3 \pm 1.7\%$ in day-7 wounds (Fig. 1b). Fascia EPFs that clustered at wound centres were 76.6 and 52.2% positive for the myofibroblast markers α -SMA and DLK-1, respectively (Fig. 1c).

To visualise how fascia EPFs become enriched in late wounds and in scars, we analysed physiological wounds using intravital microscopy coupled with a skin chamber that was placed over a full-thickness back-skin wound in *En1^{Cre};R26^{mTmG}* reporter mice. 3D snapshots of the whole in vivo wound at 14 days post-injury (dpi) clearly showed EPFs were enriched in wound centres, where they aggregate into a swarm eye that is devoid of ENFs (Fig. 1d). Supplementary Movie 1 shows a high-resolution 6-h intravital live recording of fascia EPFs at the leading front of the swarm (Supplementary Movie 1). Particle image velocimetry (PIV) analysis revealed that individual foci of EPFs join into large collective swarms that move towards wound centres (Fig. 1e). Prediction measurements of cell orientations (see Methods section) showed that EPFs collectively align themselves towards the leading front as a group (Fig. 1f and Supplementary Movie 2). Furthermore, cell trajectory measurements clearly demonstrated fascia EPFs migrated collectively in physiologic wounds towards the wound centre (Fig. 1g).

Fascia EPFs swarm to form scars. Intravital live imaging in animals is limited to 6-h intervals, revealing only fragments of scarring event. In order to visualise the entire scarring process, we invented an ex vivo skin-fascia explant culture technique termed as SCAD.

In brief, we excised and incubated 2-mm full-thickness mouse skin discs that included the epidermis, dermis, panniculus carnosus and subcutaneous fascia, with the fascia side facing upwards (Supplementary Fig. 2a). Under these conditions, skin-fascia explants developed uniform scars over a course of 5 days (Fig. 2a and Supplementary Fig. 2b). The technique worked with skin grafts of all ages from embryonic day 18.5 to adult (Supplementary Fig. 2c). These were bona fide scars by several different parameters. Histologic sections revealed masses of fibroblasts that developed increasingly woven connective tissue that bridged between skin folds. The fascia fibroblasts created a plug of collagen fibres that progressively formed scars (Fig. 2a, Day 5). 3D-immunolabelling of fibrillar matrix proteins revealed abundant fibronectins and collagen I aligning within ex vivo scars, with no elastin, just like in animals (Supplementary Fig. 3a, b). More conclusively, fractal analysis¹² of extracellular matrix lattice arrangements indicated that our ex vivo scars are structurally identical to those developing in animals, with similar lattice complexity and porosity values (Supplementary Fig. 3c, d). Mass spectrometry-driven proteomic analysis and subsequent String protein–protein interaction network analysis revealed a similar matrix protein composition and protein–protein interaction between SCAD and in vivo scars (Supplementary Fig. 3e, f and Supplementary Data 1). Unlike reconstructed 3D skin models, SCADs contained most skin and fascia cell types including



leucocytes, macrophages, lymph and blood vessels, adipocytes, panniculus carnosus muscle, pigmented melanocytes and β 3-tubulin positive nerve bundles, and their native microenvironments at unprecedented resolution during wounding (Supplementary Fig. 4a–g). When SCADs made from *En1*^{Cre};*R26*^{mTmG} mice, where EPFs and ENFs were distinctly labelled green and red

respectively, EPFs were the major contributor to scar (Supplementary Fig. 4h, i), and expressed myofibroblast markers α -SMA and DLK-1 (Supplementary Fig. 4j, k), exactly as in animals (Fig. 1a, b, d). α -SMA expression in EPFs was initially low ($3.6 \pm 2.7\%$) but substantially increased in SCADs on day 5 ($41.3 \pm 13.3\%$) mirroring the upregulation of α -SMA on myofibroblasts

Fig. 1 Collective migration of fascia EPFs in physiological in vivo wounds. **a** Masson's trichrome staining and fluorescence images of vertical sections and transverse cross sections of wounds at 7-dpi from *En1^{Cre};R26^{mTmG}* mice. EPFs were shown in green, ENFs in red, nuclei stained with DAPI in blue. The yellow dashed lines in vertical sections indicate the position of the cross sections. **b** EPF enrichment index in uninjured normal fascia or wounded fascia. Mean \pm SD, $p = 0.0019$, unpaired two-tailed t -test, $n = 4$. **c** Immunolabelling of α -SMA or DLK-1 in magenta of boxed area showed in **a**, and quantification of the percentages of α -SMA⁺ or DLK-1⁺ cells in EPFs and ENFs. Mean \pm SD, unpaired two-tailed t -test, $p = 0.0001$ (α -SMA), $p = 0.001$ (DLK-1), $n = 5$. **d** 3D image of in vivo wound at 14-dpi on the back of *En1^{Cre};R26^{mTmG}* mice. White boxes indicate field of view for intravital live imaging (Supplementary Movie 1) and particle image velocity (PIV) analysis. Images are representative of three biological replicates. **e** PIV analysis of EPF migration over the indicated time. The colour-coded vectors indicate the direction and displacement in pixels. **f** EPF channel of the first and last frames of the intravital recording (Supplementary Movie 2). The yellow dash lines indicate the leading front of invading fibroblasts, purple lines are predicted EPF cell orientation. **g** Contour lines are smoothed EPF leading front in selected frames from the intravital recording. Colours indicate time, bright for the beginning (t_0) and dark for the end (t_f). Cyan lines are predicted trajectories of EPF swarm that are perpendicular to contour lines. Scale bars: **a, b, d** = 500 μ m; **e, f** = 50 μ m.

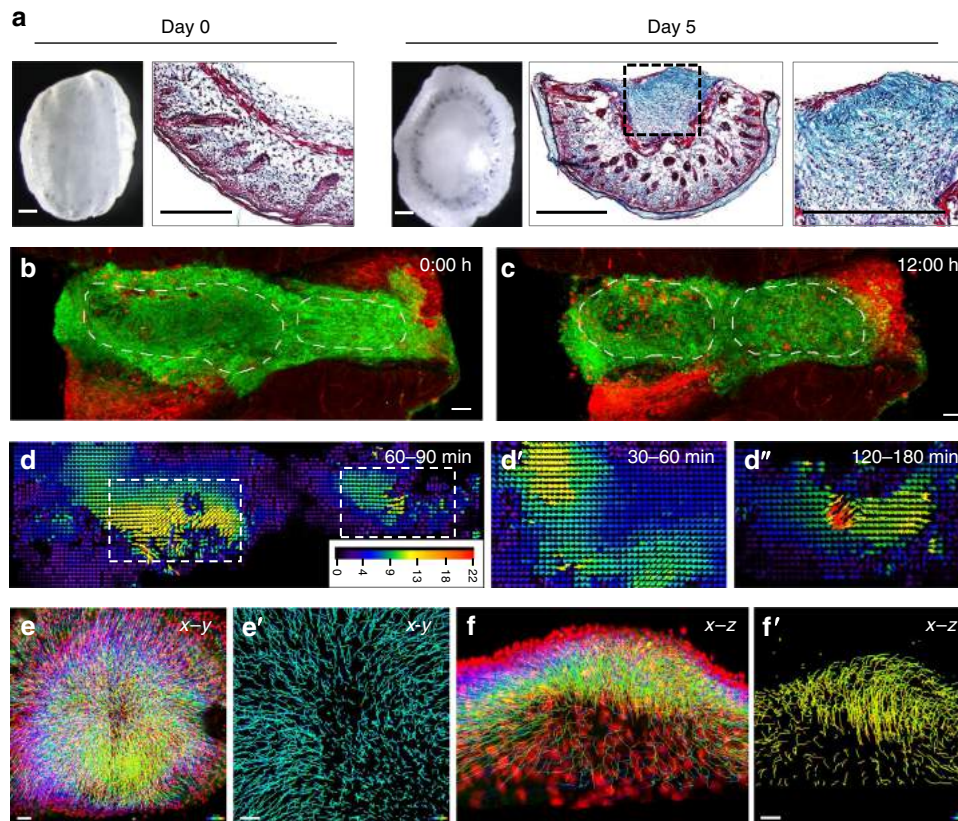


Fig. 2 Fascia EPFs swarm during scarring in SCAD. **a** Whole-mount bright-field images and Masson's trichrome staining with collagen in blue of fresh SCAD (day 0) and after 5-day culture (day 5). $n > 1000$. **b, c** Snapshots of live imaging of day 3 *En1^{Cre};R26^{mTmG}* SCAD. Two independent EPF aggregates are circled with a dotted line at time $t = 0$ h (**b**) and $t = 12$ h (**c**) (Supplementary Movie 4). Images are representative of four biological replicates. **d** PIV analysis of GFP channel from live imaging showed in Supplementary Movie 4. Arrowheads indicate the direction of particle movement. Particle velocity is indicated by a scale from slow (blue) to fast (red). Scale bar unit: pixel. **d'**–**d''** Vector map from PIV analysis of the left swarm over 30–60 min (**d'**) and of the right swarm over 120–180 mins (**d''**). **e, f** Colour-coded tracking of EPFs from live imaging (72–96 h) of *En1^{Cre};R26^{LSL-H2B-mCherry}* SCAD, from top view (**e**) and side view (**f**). Colours indicate time, starting from blue to red at the end of the movie (Supplementary Movie 6). **e'** Enlarged images of EPF migration tracks in the scar centre at the beginning of swarming (blue-to-cyan). **f'** Enlarged images of EPF migration tracks at the end of swarming (green-to-orange). Images are representative of four biological replicates. Scale bars: **a** = 500 μ m; **b, c, e, f** = 50 μ m; **e', f'** = 30 μ m.

in physiologic wounds (Supplementary Fig. 5). Collectively, these data demonstrate that SCADs have scars with identical matrix structure and protein composition, the same diverse cell types, fibrogenic cell origins and identical surface markers to in vivo fascia scars.

Having found that mobilisation of fascia tissue leads to scars in wounds, and can be studied ex vivo, we set out to view how fascia is mobilised and form real scars using multi-photon live imaging microscopy in SCAD.

Fractal analysis of SCADs from genetically labelled mice indicated that fascia EPFs uniquely increase intercellular connectivity within several hours after injury. Certain regions had a

simple porous structure, indicative of healthy fascia, whereas other areas developed a complex and smooth architecture, characteristic of an early stage scar in physiologic wounds (Supplementary Fig. 6a–c). In order to view the onset of fascia EPF migration, we generated chimeric SCADs where the interior part of the 4-mm tissue with green-labelled EPFs was replaced with 2-mm red-labelled tissue from a separate transgenic mouse. This mixing of tissues allowed single fascia EPFs to be clearly visualised as they entered the red-only inner tissue. The fascia EPFs clearly invaded the inner circle as aggregates within 24 h and each aggregate of EPFs moved collectively as a group (Supplementary Fig. 6d and Supplementary Movie 3).

By day 3, we frequently observed several distinct swarm clusters varying in size within a single SCAD. At least 4 swarms could be seen in Supplementary Movie 4. Two large swarms from SCADs were outlined at the 72 h and 96 h of the scarring process in Fig. 2b, c. Individual EPF swarms had various speeds and they changed direction regularly with a periodicity between one to two hours (Fig. 2d–d’).

To map the overall cell trajectory of all the EPF swarms, we wanted to move from manual to computational cell tracking, but the highly variable shapes of fibroblasts makes this difficult. We therefore crossed our fibroblast lineage-specific promoter mice to a nuclear mCherry reporter line and imaged SCADs from the offspring. Strikingly, all fascia EPFs coalesced into a single mega-swarm by day 4 (Fig. 2e, f). Fascia EPFs at the periphery moved towards the centre (Fig. 2e, e’). Once at the centre, fascia EPFs migrated vertically and towards the epidermis, generating a swarm eye of densely packed EPFs that contracted the skin from all sides (Fig. 2f, f’). The top view in Supplementary Movie 5 showed the collective movements of EPFs (mCherry-positive nuclei), as a single swarm across the dermis and the side view in Supplementary Movie 6 showed migratory tracks of EPFs towards epidermis.

Having discovered fibroblast swarms during back-skin scarring, we went on to investigate if swarms occur in the oral mucosa, an anatomic region that lacks fascia tissue and heals with minimal scarring, unlike the back-skin. We used a reporter mouse that permanently labels Wnt1-lineage positive fibroblasts (WPFs) that heal wounds in cranial skin and oral mucosa^{7,13}. We crossed fibroblast lineage-specific reporter mice (*Wnt1*^{Cre}) to *R26*^{mTmG} mice and made SCADs from the buccal mucosa of double-transgenic offspring (*Wnt1*^{Cre}; *R26*^{mTmG}). These tissues had no scars and minimal bundles of aligned collagen (Fig. 3a, b).

WPFs remained intermixed with other fibroblasts at all time and did not form pre-scar aggregates, compared to EPFs in back-skin SCADs (Fig. 3c–e). WPFs remained at ~50% in oral SCADs throughout the 5 days (Fig. 3e), similar to healthy oral mucosa.

To analyse the complete migration dynamics of WPFs at the whole-tissue level, we crossed *Wnt1*^{Cre} and nuclear mCherry reporter mice and made SCADs from buccal mucosa of the offspring. The migration and computational tracking of WPFs as showed in Supplementary Movies 7 and 8 respectively, revealed that oral mucosa fibroblasts moved stochastically without migrating in any particular direction, i.e., completely unlike fascia EPFs from back-skin (Fig. 3f–h). Oral mucosa fibroblasts migrated at around half the speed of back-skin fascia EPFs without the periodic shrivelling and relaxation seen in back-skin (Fig. 3i). Oral mucosa fibroblasts also did not swarm together (Supplementary Movie 9) and did not generate the same tensile forces and tissue bending movements as back-skin fascia EPFs. Thus, the swarming that causes scarring is an exclusive feature of the scar-forming fascia EPFs.

Our in vivo and ex vivo imaging and analyses revealed a collective migration pattern of fascia EPFs in wounds that build in a crescendo, with individual foci of EPFs joining into large collective swarms. Overall the collective swarms were remarkably similar when viewed by intravital imaging deep in mice and when viewed in ex vivo SCAD cultures.

Fibroblast swarms are driven by N-cadherin. Since fascia EPFs swarm during scar formation, we reasoned that they must require an adhesion molecule to aggregate. Cell adhesion is a calcium-dependent process. We therefore tested our hypothesis by inhibiting cell–cell adhesion in SCADs with the Ca²⁺ chelator EGTA. The blockage of Ca²⁺ signalling resulted in significantly reduced scarring (Supplementary Fig. 7a).

To determine which specific adhesion molecule was involved in swarming, we tested a panel of candidates for co-localisation with fascia EPFs in the scar area and found a clear co-localisation of N-cadherin (Fig. 4a). Among other adhesion molecules, notably integrins failed to co-localise (Supplementary Fig. 7b–d). However, the downstream effector of N-cadherin, α -catenin, did co-localise with fascia EPFs and N-cadherin in the scar area, consistent with a potential role for this molecule in swarming and scarring (Supplementary Fig. 7e). N-cadherin was minimally expressed by fascia EPFs upon wounding and was upregulated during the healing and scarring process (Fig. 4a and Supplementary Fig. 7f, g).

In contrast, WPFs in oral SCADs minimally expressed N-cadherin (Supplementary Fig. 7h). We therefore specifically blocked N-cadherin in *En1*^{Cre}; *R26*^{mTmG} SCADs with 500 μ g/ml Exherin, a synthetic peptide that selectively inhibits N-cadherin^{15,16}. Under Exherin treatment, EPFs refrained from aggregating and remained dispersed in the fascia and skin bending and folding was completely inhibited (Fig. 4b, c). Exherin treatment also abolished the wound-induced upregulation of α -SMA expression in fascia EPFs (Supplementary Fig. 5). Furthermore, the Exherin-treated tissues had profoundly altered expression pattern of decorin (Fig. 4d, d’), a marker of scar matrix assembly that binds to collagen fibrils¹⁷. Indeed, we observed that non-treated tissues had densely packed fascia EPFs with organised collagen I fibres, whereas Exherin-treated tissues had a mixed “salt and pepper” pattern of granular collagen deposition without uniform fibre bundles (Fig. 4e). Supplementary Movie 10 demonstrated this “salt and pepper” pattern of collagen was throughout the entire Exherin-treated SCAD. Correspondingly, Exherin-treated SCAD showed minimal scar by histology (Fig. 4f, g) and distinct collagen fibre arrangements to control scars by fractal analysis (Fig. 4h). These specific effects of Exherin were not due to increased cell death (Supplementary Fig. 7i, j) or reduced proliferation of EPFs (Supplementary Fig. 8a–c). In fact, the cell proliferation was not essential for the initial stage of scar formation (Supplementary Fig. 8d).

Compared to the mega-swarms and centripetal movements seen in control SCADs and in animals (Fig. 2e and Supplementary Movie 5), Exherin-treated fascia EPFs had greatly diminished collective migration (Fig. 4i and Supplementary Movie 11).

Overall, these data demonstrate unequivocally that N-cadherin facilitates the fibroblast swarming that leads to and links fascia mobilisation in wounds with scarring.

N-cadherin drives scarring in animals and in human skin. To test if our mechanistic findings from SCADs occur in animals, we first generated full-thickness wounds on backs of animals and found that the dynamic upregulation of N-cadherin in in vivo wounds mimics N-cadherin expression found in SCADs, with minimal expression in healthy skin and significantly elevated expression in day-7 and day-14 wounds, which co-localised with EPFs in scars (Supplementary Fig. 9).

We injected AAV6 viral particles expressing Cre recombinase into the fascia surrounding wounds in N-cadherin floxed mice (*Ncad*^{fl/fl}), which contains loxP sites flanking exon 1 of the *N-cadherin* gene. Thereafter, the transduced Cre-expressing fascia fibroblasts around wounds lost N-cadherin. As compared to the control virus, the Cre-expressing virus resulted in 65% reduction of N-cadherin expression in the scar region (Fig. 5a, b), and reduced scar area and width, evidenced by whole-mount macroscopic and histologic analyses (Fig. 5c–f). More importantly, transverse histologic views of scars clearly demonstrated that the centripetal pattern of collagen fibres around scar centres was disrupted by the N-cadherin patchy knockout (Fig. 5e lower panel). Fractal analysis measurements of control scars showed typical high fractal dimension (FD) and lower

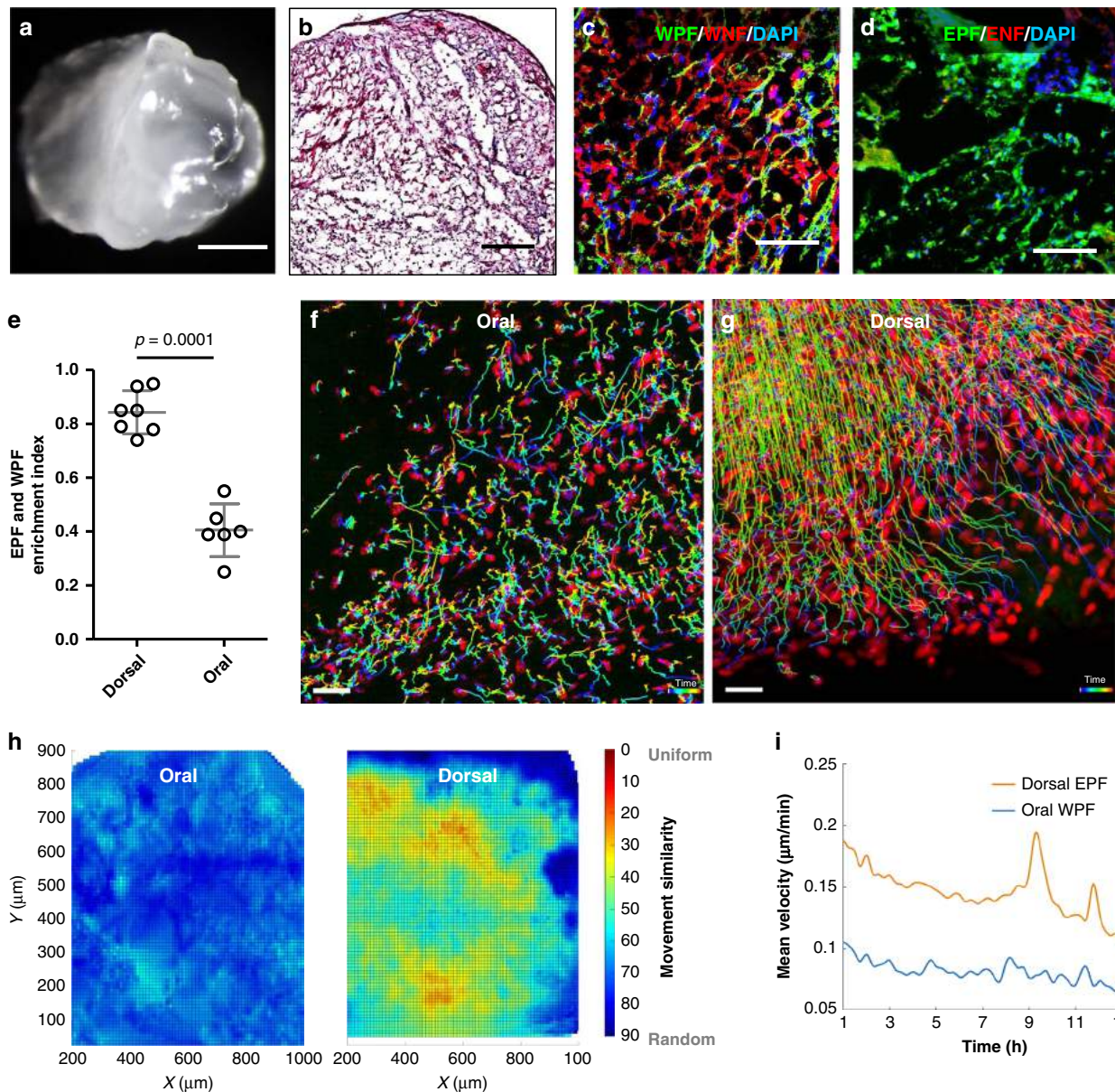


Fig. 3 Fibroblast swarms are absent from oral mucosa SCAD. **a, b** Whole-mount bright-field image (**a**) and Masson's trichrome staining (**b**) of SCAD from buccal mucosa. $n > 30$. **c, d** Fluorescence images of SCAD from *Wnt1^{Cre};R26^{mTmG}* buccal mucosa (**c**) and *En1^{Cre};R26^{mTmG}* back-skin (**d**). **e** EPF and WPF enrichment index in day 5 *En1^{Cre};R26^{mTmG}* dorsal SCAD or *Wnt1^{Cre};R26^{mTmG}* oral SCAD, respectively. Mean \pm SD, unpaired two-tailed *t*-test, $p = 0.0001$, $n = 7/6$. **f, g** Colour-coded tracking of WPFs in oral SCAD (**f**, Supplementary Movie 8) or tracking of EPFs in dorsal SCAD (**g**) on a mCherry nuclear reporter (72–96 h). The colour indicates the time, with purple at the beginning and red at the end of the movie. Images are representative of three biological replicates. **h** Movement similarity between WPF and EPF tracks is visualised in a scale from 0 (red, uniform migration) to 90 (blue, random migration). **i** Comparison of velocities of WPFs in oral SCADs (blue) versus fascia EPFs in dorsal SCAD (orange) over time. Lines shown are smoothing lines over all velocity values at each time point. Scale bars: **a** = 500 μm ; **b** = 200 μm ; **c, d** = 50 μm ; **f, g** = 30 μm .

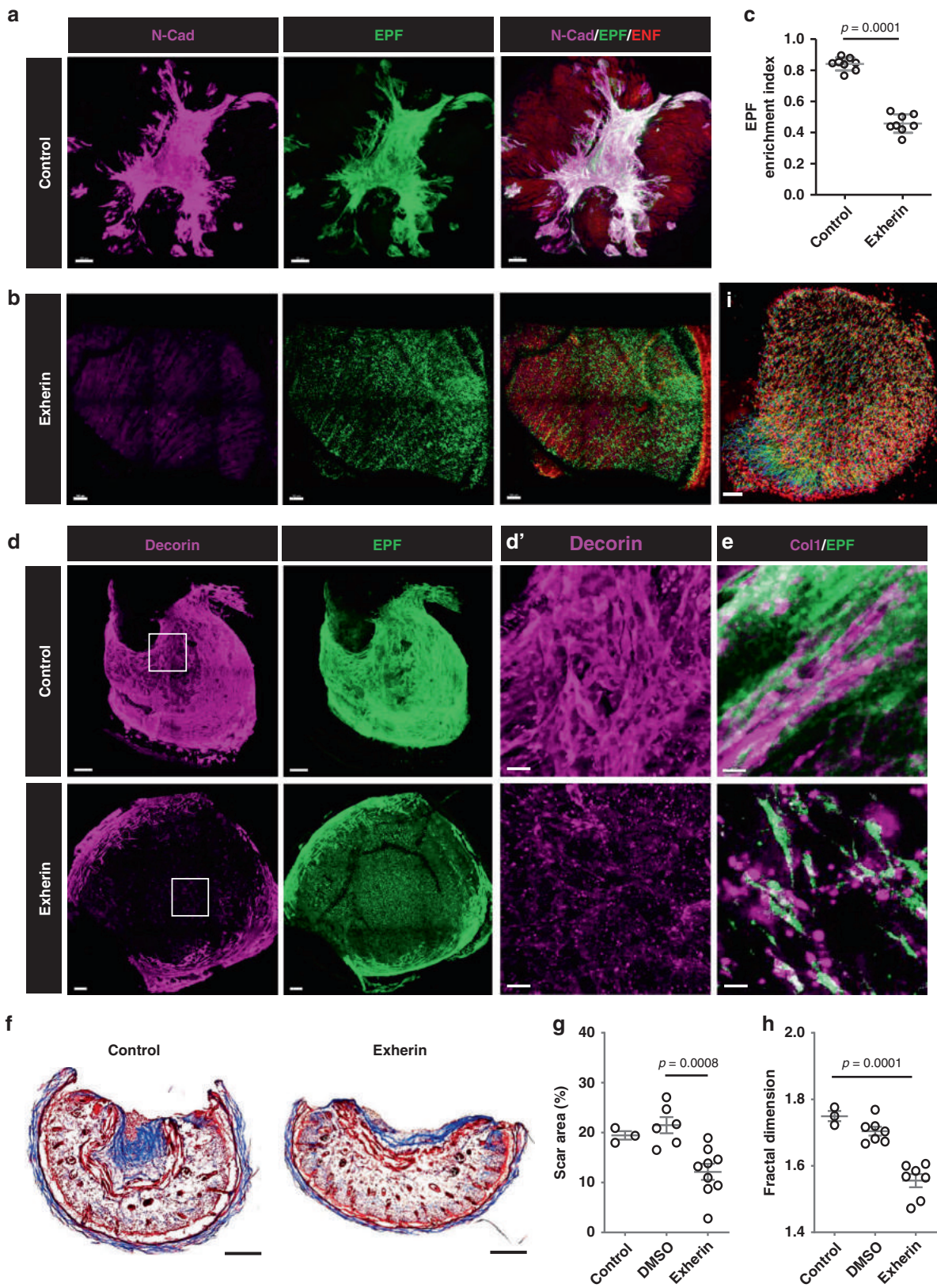
lacunarity (L) values in scars as compared to adjacent normal skin (Fig. 5g).

N-cadherin knockout scars had a significantly more porous and less complex lattice (Fig. 5g), indicating that loss of N-cadherin improves wound quality.

To further confirm the essential role of N-cadherin in swarming that leads to scarring, we used an independent strategy to locally patchy knockout N-cadherin using CRISPR-Cas9. AAV6 viral particles expressing guide RNA targeting murine *N-cadherin* exon 1 or control virus were injected into the fascia surrounding wounds of full-body Cas9-expressing *R26^{Cas9}* mice. N-cadherin down-regulation substantially reduced scar size in animals, as evidenced macroscopically and histologically (Supplementary Fig. 10). We

further crossed *En1^{Cre}* mice with Cas9 knock-in mice to generate offspring in which only EPFs express Cas9. We locally knocked out N-cadherin in fascia EPFs by injecting viruses expressing specific guide RNA into the fascia surrounding wounds. Similar to our previous two experimental models, specific loss of N-cadherin in EPFs resulted in smaller scars and disrupted EPF swarming in animals (Supplementary Fig. 11).

To test if the N-Cadherin mechanism seen in SCADs and mice is clinically relevant, we generated SCADs from human skin-punch biopsies from eyelids or from thigh-wound margins. SCADs made from human tissues behaved in the same way as mouse. Human SCADs contracted and curved over 14 days, and ultimately stiffened with scars (Fig. 6a, b). As in mouse SCADs,



N-cadherin expression within the contracted human SCADs overlapped with fibroblast aggregates (Fig. 6c).

We also examined the expression of N-cadherin in primary human hypertrophic breast scars (Fig. 6d) by whole-mount immunostaining. N-cadherin was highly expressed in scar fibroblasts

directly beneath the epidermis, (Fig. 6e–e', Supplementary Movie 12). N-cadherin-positive fibroblasts aligned in fibres in the more mature scar tissue in the deepest areas (Fig. 6e'' and Supplementary Movie 12). Adjacent normal breast skin had healthy dermal patterns (Fig. 6f) and minimal N-cadherin expression (Fig. 6g, g').

Fig. 4 Fibroblast swarms are driven by N-cadherin. 3D immunolabelling of N-cadherin (magenta) in control (a) or 500 µg/ml Exherin treated (b) *En1^{Cre};R26^{mTmG}* SCAD. c EPF enrichment index in control or Exherin-treated SCAD. Mean ± SD, $p = 0.0001$, unpaired two-tailed t -test, $n = 8$. 3D immunolabelling of decorin (d) or collagen I (e) in a control (upper panel) or Exherin-treated (lower panel, Supplementary Movie 10) SCAD. d' High magnification of white box in d. f Masson's trichrome staining of control (upper) or Exherin-treated (lower) SCAD. g Scar areas of control, or DMSO treated or Exherin-treated SCADs. One-way ANOVA Tukey's test, $p = 0.0008$, $n = 3/6/9$. h Fractal dimension analysis of control, or DMSO treated or Exherin-treated SCADs. One-way ANOVA Tukey's test, $p = 0.0001$, $n = 3/7/7$. i Colour-coded tracking of fascia EPFs from live imaging (72–96 h) of 500 µg/ml Exherin-treated *En1^{Cre};R26^{LSL-H2B-mCherry}* SCAD. Colours indicate time, starting from blue to red at the end of the movie (Supplementary Movie 11). Scale bars: a, b, d, i = 100 µm; d' = 20 µm; e = 50 µm.

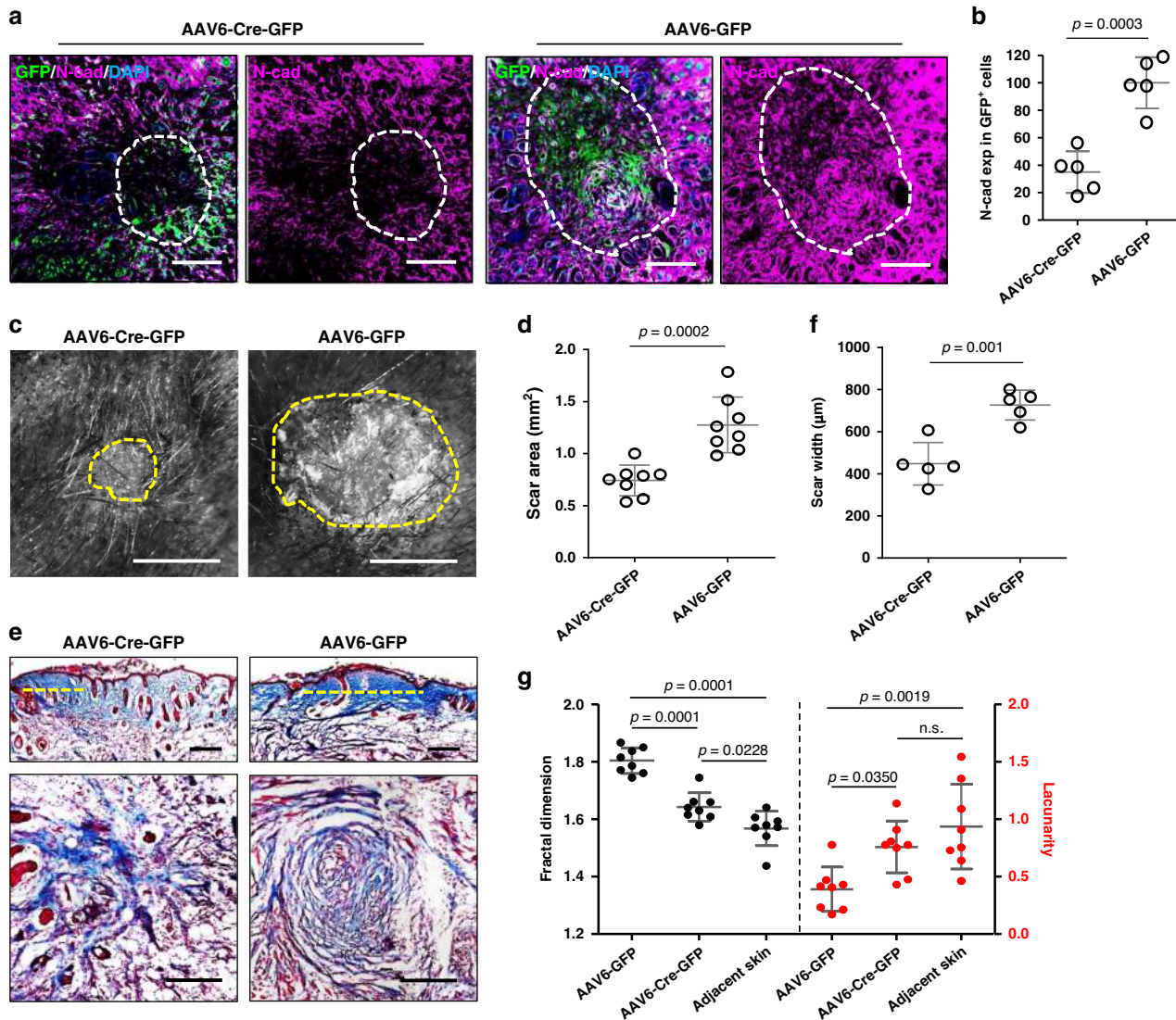


Fig. 5 N-cadherin is crucial for scar formation in vivo. N-cadherin was locally knockout around wounds on *Ncad^{fl/fl}* mice by injection of Cre-expressing AAV6-Cre-GFP virus. AAV6-GFP virus served as control. a Immunolabelling of N-cadherin on transverse cross-sections of harvested scars on 14-dpi. GFP indicates transduced cells. Dash lines outline the scar edges. b N-cadherin expression in GFP⁺ cells based on immunofluorescence analysis. Data are normalised on the mean of N-cadherin expression in AAV6-GFP wounds. Mean ± SD, $n = 5$, $p = 0.0003$, unpaired two-tailed t -test. c Stereomicroscopic images of AAV6-Cre-GFP and AAV6-GFP treated scars at 14-dpi. The yellow dash lines indicate the scar edge. d Quantification of scar area based on histomorphometric analysis. Mean ± SD, $n = 8$, $p = 0.0002$, unpaired two-tailed t -test. e Masson's trichrome stained vertical (upper panel) and transverse (lower panel) sections from AAV6-Cre-GFP and AAV6-GFP treated scars. The dash lines indicate scar width. f Quantification of scar width based on histomorphometric analysis. Mean ± SD, $n = 5$, $p = 0.001$, unpaired two-tailed t -test. g Fractal dimension and lacunarity analysis of AAV6-Cre-GFP and AAV6-GFP treated scars and adjacent normal skin. Mean ± SD, one-way ANOVA Tukey's test, $n = 8$, p values from multiple comparisons are shown in the graph. Scale bars: a, d = 200 µm; b = 500 µm.

Discussion

We recently demonstrated that the key scar-forming cells reside deep in the subcutaneous fascia⁹ but their movements had not been visualised in real-time and the mechanism was not explained.

Here we used in vivo and ex vivo live imaging to uncover their novel mode of movement and key molecular player and can thus propose a model of mammalian scarring involving N-cadherin expression and cell swarming towards formative scar centres

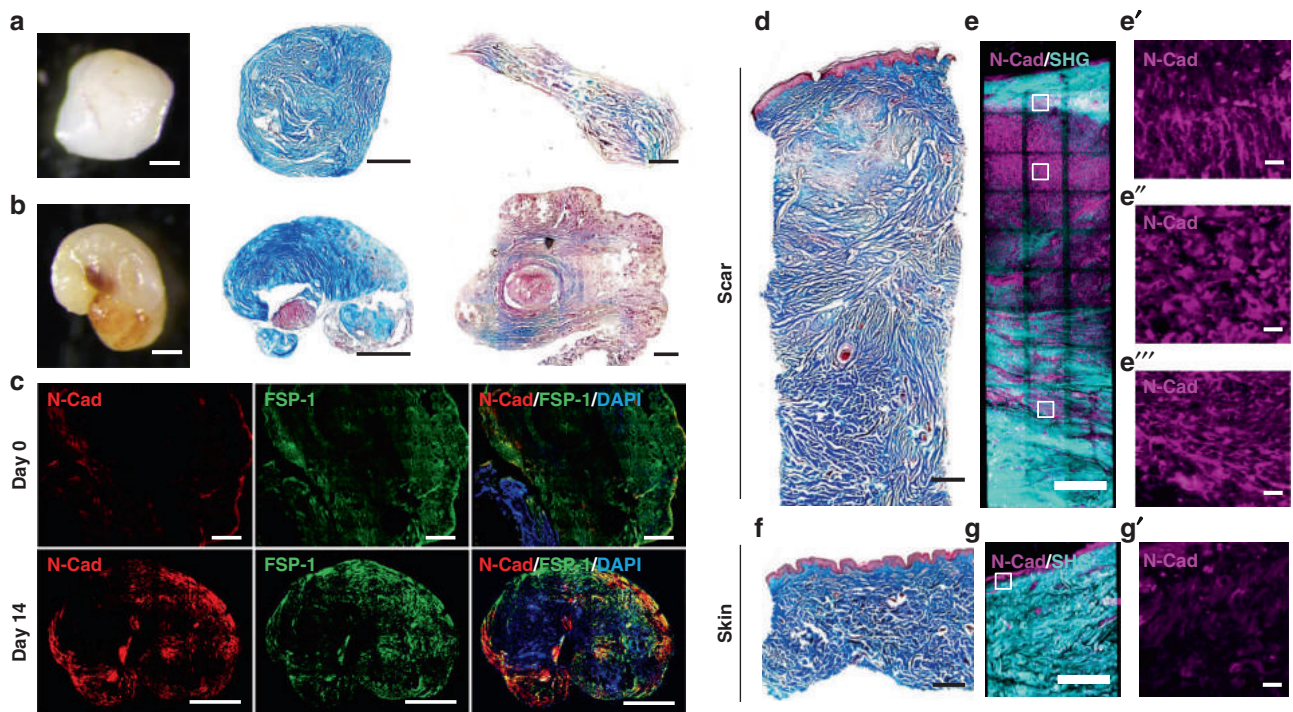


Fig. 6 N-cadherin is involved in scar formation in human skin. **a, b** whole-mount bright-field image and Masson's trichrome staining of SCADs made from human eyelid skin (**a**) or thigh skin (**b**) 14 days after culture (middle). The histology of respective fresh SCADs is shown in right column. $n > 100$. **c** Immunolabelling of N-cadherin (red) and FSP1 (green) of human SCAD at day 0 and day 14. **d–g** Masson's trichrome staining and 3D immunostaining of N-cadherin on biopsy from human breast hypertrophic scar (**d, e**) or adjacent breast skin (**f, g**). N-cadherin (magenta), SHG (cyan). The enlarged images of the N-cadherin channel indicated by white boxes in **e, g** are shown in **e', e'', e'''** and **g', g''**, respectively. Scale bars = 500 μm , except **e'–e''', g'** = 20 μm .

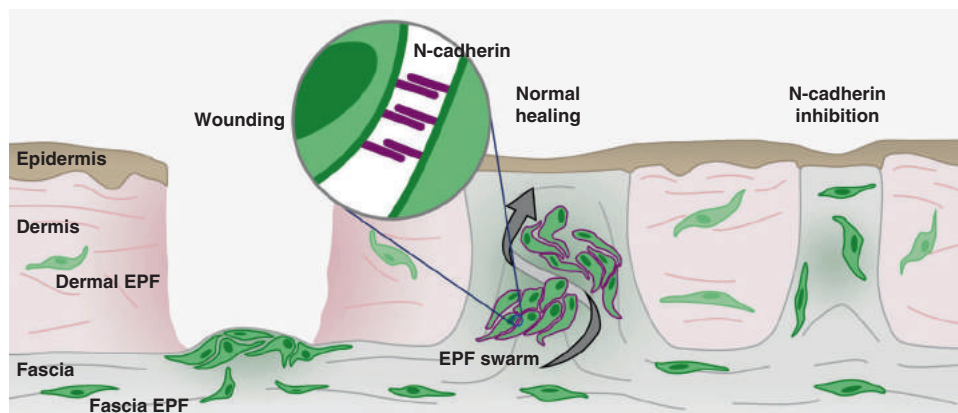


Fig. 7 Scheme of N-cadherin mediated fascia EPF swarms upon wounding and scarring. upon deep wounding, fascia EPFs assemble into aggregates and migrate collectively towards wound centre and then swarm towards epidermis by N-cadherin (purple) mediated cell-cell adhesion. Fascia EPF swarming triggers fascia mobilisation into wounds, contracts skin and drives scar formation. EPF swarms are absent in the tissues without fascia (e.g. oral mucosa) or when N-cadherin is inhibited by chemicals (eg. Exherin) or genetic mutations. The absence of collective migration of fascia EPF swarms results in less scar formation.

(Fig. 7). Fascia EPFs upregulate N-cadherin upon wounding. The elevated intercellular adhesion is required for the aggregation and collective migration of fascia EPFs, and subsequent swarming towards wound centres. Swarming of fascia EPF triggers fascia mobilisation into wounds, contracts the skin and drives scar formation. In the tissues without fascia (eg. oral mucosa) or when N-cadherin is inhibited chemically (eg. Exherin) or genetically, fascia EPF swarming is absent, resulting in minimal scars.

The here proposed wound-induced mechanism helps to expound a series of earlier observations that indicate the provisional granulation tissue padding the wound bed is not responsible for contraction but rather that the active contraction comes

from outside of the wound¹⁸. Indeed, excisions of the wound edge, which would disrupt swarming behaviours, relax skin contraction¹⁹.

N-cadherin has been shown to play a critical role in the invasion and migration of spheroid-myofibroblast aggregates into Collagen I gel or Matrigel in vitro²⁰. Fibroblasts from Crohn's disease strictures express enhanced levels of N-cadherin and N-cadherin overexpression has been shown to enhance fibroblast migration in vitro^{21,22}. Previous studies also suggest wound-induced TGF- β 1 signalling could be a trigger of elevated adherens junctions^{20,21}. In addition, it has been demonstrated recently that upregulation of N-cadherin in glioma cells is dependent on p120-

catenin. The adherens junctions stabilised by N-cadherin, β -catenin and p120-catenin appear to be crucial for the collective brain infiltration of glioma cells²³. The exact molecular trigger of N-cadherin upregulation that drives fascia mobilisation requires further investigation.

The fascia system is not only present in skin. It is a continuous viscoelastic matrix that attaches, encloses, separates and interpenetrates all tissues and organs²⁴. We therefore believe that fibroblast swarming is likely a general fibroblastic response to injuries in mammalian tissues and organs and not restricted to back-skin. Support to this tenet comes from functional experiments and *in silico* data from kidney and lung fibrosis. In these two models of fibrosis, Cadherin-11 is upregulated on fibroblasts in their connective tissues, and also serves as a translational biomarker for kidney fibrosis²⁵. Cadherin upregulation in fibroblasts is directly linked to their invasion during lung fibrosis^{26–28}. Fibroblast swarms within the injured internal organs may thus contribute to scarring in the same way as shown here in skin.

The recruitment of the fascia into wounds by fibroblast swarms has enormous clinical significance and opens a novel therapeutic space. Strategies that inhibit fascia fibroblast swarms from developing, for example by blocking the key molecule N-cadherin, could lead to therapeutics for preventing or reducing scar formation in human wounds.

Methods

Mice. C57BL/6J, *En1*^{Cre}, *Wnt1*^{Cre}, *ROSA26*^{LSL-H2B-mCherry} (*R26*^{LSL-H2B-mCherry})²⁹ (JAX #023139), *ROSA26*^{DTR} (*R26*^{DTR}) (JAX #008040), N-cadherin floxed mice *Ncad*^{fl/fl} (JAX #007611), B6.129S6(SJL)-Cdh2^{m1Glr/J} and Cas9 knock-in mice *R26*^{LSL-Cas9-knockin} (JAX #026175, B6J.129(B6N)-Gt(ROSA)26Sor^{tm1(CAG-cas9*,-EGFP)Fzh/J}) strains were obtained from Jackson laboratories. The *ROSA26*^{mTmG} (*R26*^{mTmG}) reporter mice were from Stanford University. *En1*^{Cre} or *Wnt1*^{Cre} transgenic mice were crossed with *R26*^{mTmG} or *R26*^{LSL-H2B-mCherry} reporter mice. Cas9-expressing Gt(ROSA)26Sor^{tm1(Cas9)Rad} (*R26*^{Cas9}) mice were obtained from R. Rad (Institute of Molecular Oncology and Functional Genomics, Technical University of Munich, Germany). Animals were housed at the Helmholtz centre animal facility. The rooms were maintained at constant temperature and humidity with a 12-h light cycle. Animals were allowed food and water ad libitum. All animal experiments were reviewed and approved by the Government of Upper Bavaria and registered under the project ROB-55.2-2532.Vet_02-16-61 and ROB-55.2-2532.Vet_02-19-23, and conducted under strict governmental and international guidelines. This study is compliant with all relevant ethical regulations regarding animal research. Both male and female mice were used in the study. For wounding experiment with silicone splints in adult mice, the mice were wounded during telogen hair cycle stage.

Human skin samples. Fresh human skin and scar biopsies, including 2 hypertrophic scars, from various anatomic locations, were collected from 71 donors between 18 and 65 years of age, through the Section of Plastic and Aesthetic Surgery, Red Cross Hospital Munich (reference number 2018–157), and by the Department of Dermatology and Allergy, Klinikum rechts der Isar, Technical University Munich (reference number 85/18S). Informed consent was obtained from all subjects prior to skin biopsies. Upon collection, these samples were directly processed for tissue culture or fixed with PFA and then processed for cryosection or paraffin section followed by histological or immunofluorescent analyses.

Scar-like tissue in a dish assay. Full-thickness back-skin including fascia was collected from C57BL/6J or two-colour membrane reporter *En1*^{Cre}; *R26*^{mTmG} or nuclear reporter *En1*^{Cre}; *R26*^{LSL-H2B-mCherry} neonates at postnatal day 0–1, to allow a homogeneous fascia thickness. The harvested tissue was washed twice with cold DMEM/F-12 (Thermo Fisher Scientific 11320074) medium to remove contaminating blood, and then washed once with Hank's Balanced Salt Solution (HBSS, Thermo Fisher Scientific 14175095). After careful removal of ventral non-skin tissue with a surgical scalpel, round skin pieces were cut out with a disposable \varnothing 2 mm biopsy punch (Stiefel 270130) down to below the panniculus carnosus muscle, and cultured in 200 μ l of DMEM/F-12 medium containing 10% FBS, 1x GlutaMAX (Thermo Fisher Scientific 35050038), 1x Penicillin/streptomycin (Thermo Fisher Scientific 15140122), and 1x MEM non-essential amino acids (Thermo Fisher Scientific 11140035) in 96-well plates, in a humidified 37 °C, 5% CO₂ incubator. (Note: the 2 mm skin pieces were cultured submerged in medium with dermal side face up, but not floating at the liquid-air interface). Fresh medium was supplied every other day and the skin tissues were harvested at the indicated time points (day 1–5 after culture), with the fresh tissues serving as day 0 control, and fixed in 2% PFA overnight at 4 °C. After washing in PBS, the tissues were

embedded and frozen in optimal cutting temperature compound and 6 μ m cryosections were prepared with a cryostat.

Oral SCADs were made from \varnothing 2-mm full-thickness cheek biopsies of neonates (postnatal day 0–1) of two-colour membrane reporter *Wnt1*^{Cre}; *R26*^{mTmG} or nuclear reporter *Wnt1*^{Cre}; *R26*^{LSL-H2B-mCherry} mice. Oral SCADs were cultured in a same way as the back-skin SCADs, with buccal mucosa face up.

Human SCADs were generated by incorporating the deep dermal and subcutaneous layers that contain fascia, but without epidermis, cultivated under same conditions as mouse SCADs. Tissues were harvested 14 days after culture, and processed for histology and immunofluorescence staining.

SCAD chimera assay. SCAD biopsies were taken from neonatal back-skin of *En1*^{Cre}; *R26*^{mTmG} mice with a \varnothing 4-mm biopsy punch. Thereafter, the 2-mm centre was excised from the 4-mm *En1*^{Cre}; *R26*^{mTmG} SCAD with a \varnothing 2-mm biopsy punch, and replaced by a 2-mm SCAD generated from the Cre-negative littermates, in which the entire tissue is RFP labelled. Resultant chimeric SCADs were cultured in our standard conditions. The migratory behaviour of GFP⁺ EPFs into RFP⁺ inner SCAD was documented by live imaging. The possibility that the injury induced upregulation of factors that may promote migration cannot be ruled out.

LC-MS/MS proteomic analysis. Scar tissues were harvested for proteomics from day 5 SCADs, and from *in vivo* 2-mm full-thickness excisional wounds on P2 neonates and at day-14 after wounding. After removing the epidermis, scar tissues were washed, pooled and homogenised. After centrifugation, proteins were extracted in Guanidinium Buffer (6 M Guanidinium chloride, 10 mM TCEP, 40 mM CAA, 100 mM Tris pH 8.5). Peptides from LysC and trypsin proteolysis (1:75), were purified on SDB-RPS material stage-tips and data was acquired on a Quadrupole/Orbitrap type Mass Spectrometer (Q-Exactive, Thermo Scientific)³⁰. MS raw files were processed by MaxQuant³¹ (version 1.5.3.20) and MaxQuant output tables were analysed using the Perseus software suite³² (version 1.5.8.7). The identified proteins were filtered for Matrisome proteins³³. Thereafter, network analysis was performed with Cytoscape software³⁴ (version 3.6.1). All other statistical and bioinformatics operations, such as normalisation, heat-map generation, string-network mapping and multiple-hypothesis testing corrections, were performed with the Perseus software suite. The mass spectrometry proteomics data have been deposited to the ProteomeXchange Consortium via the PRIDE partner repository with the dataset identifier PXD016068.

Local N-cadherin knockout in *R26*^{Cas9} or *En1*^{Cre}; *R26*^{Cas9}-knockin or *Ncad*^{fl/fl} wounds. A guide RNA (gRNA) targeting exon 1 of mouse N-cadherin was designed with the Benchling tool. The adeno associated virus serotype 6 (AAV6) expressing gRNA targeting murine N-cadherin (TCGGGCA-CATGGAGCGGAG) was created by cloning gRNA into the SAP1 sites of pAAV-U6-sgRNA-CMV-GFP (Addgene #85451³⁵). N-cadherin gRNA expressing AAV6 (AAV6-NcadgRNA-GFP) was produced by transfecting the AAVpro 293T Cell Line (Takara Bio 632273) with pAAV-U6-NcadgRNA-CMV-GFP, pRC6 and pHelper plasmids from the AAVpro Helper Free System (Takara Bio 6651). Cre-expressing AAV6 (AAV6-Cre-GFP) was purchased from Addgene (Addgene #68544³⁶). Transfection was performed with PEI transfection reagent and viruses were harvested 72 h post-transfection. AAV6-NcadgRNA-GFP or AAV6-Cre-GFP or control AAV6-GFP viruses were extracted and purified with an AAVpro purification kit all serotypes (Takara Bio 6666).

Two \varnothing 2-mm full-thickness excisional wounds were created on the back of anaesthetised 13-day-old full-body Cas9-expressing *R26*^{Cas9} mice or 5 days old *En1*^{Cre}; *R26*^{Cas9-knockin} mice that express Cas9 in EPFs. CRISPR/Cas9-based local N-cadherin ablation was performed by subcutaneously injecting 20 μ l of AAV6-gRNA-GFP virus at a viral titre of 1×10^{12} /ml at the area between the two wounds (~5 mm in distance) at day 0, 5 and 10 post-wounding. The small bleb (fluid pocket) resulted from the injection reached the edges of both wounds. The mice received subcutaneous injection of the AAV6-GFP virus without gRNA as control.

Similarly, two \varnothing 2-mm full-thickness excisional wounds were created on the back of anaesthetised 5 days old homozygous N-cadherin floxed *Ncad*^{fl/fl} mice containing loxP sites flanking exon 1 of the *N-cadherin* gene³⁷. Local N-cadherin ablation was performed by subcutaneously injecting 20 μ l of AAV6-Cre-GFP virus at a viral titre of 2×10^{12} /ml at the area between the two wounds at day 0, 5 and 10 post-wounding. The fluid pocket after injection reached the edges of both wounds. The mice received subcutaneous injection of the AAV6-GFP virus as control.

Scar tissues were harvested at day 14 post-wounding. Scar images were documented with a Leica M50 stereo-microscope (Leica) at $\times 4$ magnification. Subsequently, the scar tissue was processed for cryo-sections for histology and immunofluorescence.

Antibodies and reagent. The following antibodies were used: N-cadherin (clone GC4, Sigma-Aldrich C3865, 1:100 dilution), FSP1 (Abcam ab58597, 1:100 dilution), PDGFR α (R&D Systems AF1062, 1:50 dilution), Collagen I (Rockland 600-401-103-0.1, 1:150 dilution), Collagen III (Abcam ab7778, 1:150 dilution), Fibronectin (Abcam ab23750, 1:200 dilution), α -SMA (Abcam ab5694, 1:100 dilution), CD31 (Novus Biologicals NB100-2284, 1:500 dilution), EpCAM (Abcam ab92382, 1:500 dilution), Lyve-1 (Abcam ab14917, 1:500 dilution), Myf-5 (clone C-20, Santa Cruz

sc-302, 1:500 dilution), CD45 (clone IBL-3/16, Abcam ab23910, 1:500 dilution), FABP4 (clone EPR3579, Abcam ab92501, 1:500 dilution), F4/80 (Abcam ab90247, 1:500 dilution), Cytokeratin 14 (clone EPR17350, Abcam ab181595, 1:200 dilution), Integrin α_v (clone EPR16800, Abcam ab179475, 1:500 dilution), $\alpha 1$ -catenin (clone EP1793Y, Abcam ab51032, 1:500 dilution), decorin (Abcam ab175404, 1:500 dilution), DLK-1 (Abcam ab21682, 1:200 dilution) and Ki67 (clone SP6, Abcam ab16667, 1:500 dilution). Fluorophore-conjugated secondary antibodies were purchased from Thermo Fisher Scientific (1:500 dilution). Exherin (ADH-1) was from TargetMol (T2637).

Masson's trichrome staining. Cryo-sections were fixed in cold acetone (-20°C) for 5 min and incubated overnight in Bouin's solution (Sigma-Aldrich HT10132) at room temperature. After washing in cold tap water, the sections were stained with a working concentration of Weigert's Iron Hematoxylin (Sigma-Aldrich HT1079) for 5 min. Thereafter, the sections were treated with a Masson's trichrome stain kit (Sigma-Aldrich HT15) by sequentially incubating at room temperature in Biebrich scarlet-acid fuchsin solution for 5 min, working concentration of Phosphotungstic/Phosphomolybdic acid for 5 min, aniline blue solution for 10 min, and 1% acetic acid for 2 min. After dehydration, the sections were cleared with Roti-Histol and mounted with a Roti-Histokitt (Roth 6640 and 6638 respectively).

Cell counting was performed with ImageJ. Briefly, trichrome images were converted to CMYK and the black channel was used to count the iron haematoxylin stained nuclei. Regions of interest covering the scar area were delimited and processed using the functions of subtract background (rolling ball = 50 px), enhance contrast (saturated = 0.1 normalised), Unsharp Mask (Radius = 2, Mask = 0.6), Median (radius = 1) and the auto-threshold method Minimum. Watershed function was used in the binary images and the particles were counted (size threshold = 30–200 px^2).

For the quantification of scar areas, trichrome images were converted to CMYK and the cyan channel was used to analyse the blue-stained collagens.

Immunofluorescence staining. Cryo-sections were fixed in cold acetone for 5 min and blocked with 5% BSA in PBS for 1 h. Thereafter, sections were incubated overnight with primary antibodies at 4°C . After three PBS washes, sections were incubated with appropriate fluorophore-conjugated secondary antibodies (Thermo Fisher Scientific) at room temperature for 1 h. For double staining, sections were incubated at room temperature with the second primary antibody for 2 h, and appropriate secondary antibody for 1 h. Nuclei were counterstained with DAPI for 3 min. Coverslips were mounted with Fluoromount-G (Thermo Fisher Scientific 00–4958–02). Photomicrographs were taken with a Zeiss AxioImager microscope with AxioVision software (Carl Zeiss), or a Zeiss laser scanning microscope LSM710 with Zen software (Carl Zeiss).

Whole-mount bright-field imaging. SCAD tissues were fixed with 2% PFA at 4°C overnight, and washed three times with PBS. Whole-mount bright-field images were taken with a Leica M50 stereo-microscope (Leica) with a Leica DFC310 FX camera (Leica) and saved with Leica Application Suite (v4.8).

3D imaging. (1) By laser scanning microscopy with tissue-clearing: whole-mount samples were stained and cleared by a modified 3DISCO protocol. In short, fixed samples were pre-incubated in Dulbecco's Phosphate-Buffered Saline (DPBS, Thermo Fisher Scientific 14190169) containing 0.2% gelatin (Sigma G1393), 0.5% Triton-X100 (Sigma X100) and 0.01% Thimerosal (Sigma T8784) (PBS-GT), for 24 h at room temperature. Antibodies: anti-elastin (Abcam ab21610), anti-fibronectin (Abcam ab23750) and anti-collagen type I (Rockland 600–401–103), were pre-labelled with Alexa Fluor 488, 594 and 647 dyes (Thermo Fisher Scientific A20181, A20184, A20186) according to the manufacturer's instructions. The samples were incubated, rotating, with the labelled antibodies in PBS-GT (1:1000) for 24 h at room temperature. After washing in PBS-GT, samples were first dehydrated in an ascending THF (Sigma 186562) series (50%, 70%, 80%, $3 \times 100\%$; 30 min each), then cleared in dichloromethane (Sigma 270997) for 30 min and eventually immersed in benzyl ether (Sigma 108014). Cleared samples were imaged in 35 mm glass-bottom dishes (ibidi 81218) under a laser scanning confocal microscope (Zeiss LSM710, Carl Zeiss, Germany). Raw data was processed and optimised for visualisation, adjusting brightness and contrast with Imaris software (v9.1.0, Bitplane, UK).

(2) By multi-photon microscopy without tissue-clearing: whole-mount samples were immuno-labelled and embedded in 2% NuSieve GTG agarose (Lonza 859081) in a 35 mm dish (Falcon 351008) and were imaged under a Leica SP8 MP (Leica, Germany). Tiles were merged offline using the Leica Application Suite X (v4.8, Leica) with smooth overlap blending, and data were visualised with Imaris software (v9.1.0, Bitplane, UK) using contrast and brightness adjustments.

Live imaging using multi-photon microscopy. Full-thickness skin pieces were collected as described above and imaged with a Leica SP8 MP (Leica, Germany). In brief, samples were embedded in 4% agarose (Lonza, 859081) in a 35-mm dish (Corning, 351008) and submerged in imaging medium (phenol-red-free DMEM/F-12 (Thermo Fisher Scientific, 21041025) containing 10% KnockOut Serum Replacement (Thermo Fisher Scientific, A3181501), 1x GlutaMAX (Thermo Fisher Scientific, 35050038), 1x Penicillin/streptomycin (Thermo Fisher Scientific,

15140122), and 1x MEM non-essential amino acids (Thermo Fisher Scientific, 11140035)). A 25x water-dipping objective (HC IRAPO L 25x/1.00 W) was used in combination with a tunable laser (Spectra Physics, InSight DS + Single). Second harmonic signal was collected with external hybrid photodetectors with a HC 405/150 filter. Green, orange, red, and far-red signals were collected using a 525/50, 585/40, 624/40, and 650/50 bandpass filters.

A modified incubation system, with heating and gas control (ibidi 10915 and 11922), was used to guarantee physiologic and stable conditions during imaging (35°C , 5% CO_2). Z-stacks were recorded in 15 min intervals.

Intravital multi-photon imaging. Dorsal skinfold chamber was implanted as described before³⁸. In brief, mice were anaesthetised and the dorsal back skin was shaved, depilated and disinfected. A fold of the dorsal skin was examined for major vessels and relocated to spare them during preparation of the wound. The sterilised skinfold chamber (APJ Trading Co, Inc; Ventura, CA) was sutured to the skin on the upper side using 4/0 braided sutures (Chirilac #PG 0203, Vitrex Medical, Denmark) and fixed with the three bolts and nuts. A full-thickness wound was created in the middle of the observation window using a 3-mm biopsy punch (Stiefel) carefully removing epidermis, dermis and panniculus carnosus layer. After flushing with physiologic saline, a sterile coverslip was used to cover the wound.

The wound was imaged 14 days post wounding for a period of 6 h using a Leica SP8 MP (Leica, Germany) equipped with a 25x water-dipping objective (HC IRAPO L 25x/1.00 W) and a tuneable laser (Spectra Physics, InSight DS + Single). Fluorescent signal was generated at 960 nm (SHG, GFP) and 1050 nm (tdTomato) and collected with external hybrid photodetectors using the following bandpass filters: SHG: 405/150; GFP: 525/50; tdTomato: 585/40.

Mice were anaesthetised with 1–3% Isoflurane and maintained for the time of intravital imaging. A subcutaneous depot of 200 μL physiologic saline was injected to prevent dehydration. Mice were placed in lateral position on a heated plate and vital parameters (ECG, respiration, rectal temperature) were monitored continuously (75–1500, Harvard Apparatus, MA). The dorsal skinfold chamber was fixed on a custom made metal bracket, which was stably mounted to the stage of the microscope. A thin circular barrier of silicon grease (Korasilon, Kurt Obermeier, Germany) was applied to the coverslip to keep the immersion water from draining.

Orientation vector field analysis. Vector fields were generated using ImageJ plugin OrientationJ 2.0.4 – Vector Field³⁹. In brief, frame images of the green channel (EPFs) from intravital microscopic recording were subjected to maximum intensity projection. Substacks were created with every 10 frames of the recording. Orientation vector fields were applied with vector field grid size of 150 pixels with 100% length of scale vector. Resulting vector trajectories were converted into masks and overlaid on the original frame image.

Contour line trajectory analysis. Contour lines were derived using ImageJ plugin Interactive 3D surface plot. Maximum intensity substacks were computed using the frame images of the green channel (EPFs) corresponding to 0, 3 and 6 h of the intravital microscopic recording. These frames were subjected to 3D projection with full transparency to create a pseudo z stack. To mark the boundaries of the pseudo z stack, contour lines corresponding to leading front of the frames were overlaid and 3D surface plot were rendered. Contour lines were generated with following parameters: Grid size - full size of the image, Smoothing - 130, Lighting - 0.50 and perspective - 0.0. Resulting contour lines were displayed using standard fire lookup tables from LUT library. The gradient lines perpendicular to the contour lines are used to predict the trajectory of migrating EPF swarms.

Automated and manual cell tracking. Automated cell tracking was performed on SCADs made from nuclear reporter lines (*En1*^{Cre}; *R26*^{LSL-H2B-mCherry} or *Wnt1*^{Cre}; *R26*^{LSL-H2B-mCherry}) using Imaris software package (v9.1.0, Bitplane, UK). Tracks were generated from 4D data using the fluorescence intensity-based surface detection tool. The resulting data that represents the nuclei of Cre-positive cells were filtered for good quality. Tracks were visualised in a time-coded colour representation, ranging from purple to red. Only the last 12 time points of the respective tracks are shown for better visibility and to prevent overcrowded images and videos.

Manual cell tracking was performed on SCADs from two-colour membrane reporter lines (*En1*^{Cre}; *R26*^{mTmG} or *Wnt1*^{Cre}; *R26*^{mTmG}) with ImageJ using the Manual Tracking plugin (version 2.1.1), since the cell boundaries in the membrane reporter system can't be accurately segmented and followed by the automatic tracking software. In brief, the channels of 3D-Time lapse datasets were split and subjected to maximum intensity projection. Migration of individual cells was tracked over time. Trajectories and individual track information with coordinates were exported as TIFF and excel file respectively. Graphical visualisation and analysis of these trajectories were performed using R. Iterative loops to generate a colour-ramp for each track as a function of time and embedded into respective coordinates (Blue = first time point; Red = last time point).

Fractal analysis of images. We use fractal analysis to quantify the complexity of cellular arrangement and extracellular matrix. In this analysis, the fractal

dimensions and lacunarity values measure the complexity and porosity of shapes respectively. Complex arrangements score higher fractal dimension values than simpler arrangements, while porous structures score higher lacunarity values than smoother ones.

Images were analysed with ImageJ (ImageJ v1.47) to produce values that were analysed using GraphPad 6. For fractal analysis of collagens, trichrome images were converted to CMYK and the cyan channel was used to analyse the blue-stained collagens. Images were processed using the subtract background (rolling ball = 50 px), enhance contrast (saturated = 0.1 normalised), Unsharp Mask (Radius = 2, Mask = 0.6), Median (radius = 1) and the auto-threshold method Default functions. Fractal dimension and lacunarity values were calculated using the FracLac Plugin with a pixel threshold of 0.40.

Particle image velocimetry analysis of images. Particle image velocimetry (PIV) has been used to describe collective cell migration⁴⁰. Using the ImageJ plugin⁴¹ we performed PIV on the GFP/RFP signal from live-imaging video stacks of *En1^{Cre}; R26^{mTmG}* dorsal SCAD or *Wnt1^{Cre}; R26^{mTmG}* oral SCADs. Successive video frames of 30 min intervals from 24 h videos were subjected to iterative (cross-correlation) PIV on 64 × 64, 32 × 32 and 16 × 16 pixel sub-windows. Normalised median test (noise = 0.2, threshold = 5) post-processing was used to decrease the background noise. Calculated magnitude vectors were then used to measure direction and velocity.

Enrichment index, displacement, velocity and similarity measures of images. EPF enrichment index was calculated by mean fluorescence intensity (MFI) of GFP channel (EPF) divide by the sum of MFI of GFP channel and MFI of RFP channel (ENF). Similarly, WPF enrichment index in oral mucosa SCAD was calculated by MFI of GFP channel (WPF) divide by the sum of MFI of GFP channel and MFI of RFP channel (WNF). Displacement measures were based on five landmarks between alternate frames from live imaging. Mean displacement values were added up and plotted versus time. Using the tracked trajectories, we calculated the distance between positions of the same cell at consecutive time points in 3D. To measure movement similarity of neighbouring cells we first determined the movement vector for every cell between consecutive time points. Then we compared this vector to all movement vectors of neighbouring cells by calculating the angles between these vector pairs in 3D. Finally, we averaged all angles to produce one movement-similarity score. To identify neighbours of individual cells we applied a Delaunay triangulation on 3D cell coordinates⁴².

Statistics and reproducibility. GraphPad Prism was used for all statistical analyses except proteomics. Unless otherwise indicated, mean ± SD values are reported in the graphs. The exact statistical analyses used to quantify data, the exact values of *n*, and the exact *p* values are stated in the respective figure legends. For simplicity, *p* values below 0.0001 were stated as equal to 0.0001. All experiments were performed at least three times independently with similar results.

Reporting summary. Further information on research design is available in the Nature Research Reporting Summary linked to this article.

Data availability

The proteomics data have been deposited in the ProteomeXchange Consortium via the PRIDE partner repository with the dataset identifier: [PXD016068](https://doi.org/10.26434/chemrxiv-2020-pxd01).

The data that support the findings of this study are available from the authors on reasonable request.

Received: 18 May 2020; Accepted: 8 October 2020;

Published online: 06 November 2020

References

- Huang, T. T., Blackwell, S. J. & Lewis, S. R. Ten years of experience in managing patients with burn contractures of axilla, elbow, wrist, and knee joints. *Plast. Reconstr. Surg.* **61**, 70–76 (1978).
- Palmieri, T. L. et al. Alterations in functional movement after axillary burn scar contracture: a motion analysis study. *J. Burn Care Rehabil.* **24**, 104–108 (2003).
- Prasad, J. K., Bowden, M. L. & Thomson, P. D. A review of the reconstructive surgery needs of 3167 survivors of burn injury. *Burns* **17**, 302–305 (1991).
- Sen, C. K. et al. Human skin wounds: a major and snowballing threat to public health and the economy. *Wound Repair Regen.* **17**, 763–771 (2009).
- Sund, B. *New Developments In Wound Care*. 1–255 (London, PJB Publications, 2000). Clinical Report CBS 836.
- Szpaderska, A. M., Zuckerman, J. D. & DiPietro, L. A. Differential injury responses in oral mucosal and cutaneous wounds. *J. Dent. Res.* **82**, 621–626 (2003).
- Wong, J. W. et al. Wound healing in oral mucosa results in reduced scar formation as compared with skin: evidence from the red Duroc pig model and humans. *Wound Repair Regen.* **17**, 717–729 (2009).
- Seifert, A. W. et al. Skin shedding and tissue regeneration in African spiny mice (*Acomys*). *Nature* **489**, 561–565 (2012).
- Correa-Gallegos, D. et al. Patch repair of deep wounds by mobilized fascia. *Nature* **576**, 287–292 (2019).
- Driskell, R. R. et al. Distinct fibroblast lineages determine dermal architecture in skin development and repair. *Nature* **504**, 277–281 (2013).
- Hakkinen, L., Larjava, H. & Fournier, B. P. Distinct phenotype and therapeutic potential of gingival fibroblasts. *Cytotherapy* **16**, 1171–1186 (2014).
- Jiang, D. et al. Two succeeding fibroblastic lineages drive dermal development and the transition from regeneration to scarring. *Nat. Cell Biol.* **20**, 422–431 (2018).
- Rinkevich, Y. et al. Skin fibrosis. Identification and isolation of a dermal lineage with intrinsic fibrogenic potential. *Science* **348**, aaa2151 (2015).
- Shook, B. A. et al. Myofibroblast proliferation and heterogeneity are supported by macrophages during skin repair. *Science* **362**, eaar2971 (2018).
- Geurtzen, K. et al. Mature osteoblasts dedifferentiate in response to traumatic bone injury in the zebrafish fin and skull. *Development* **141**, 2225–2234 (2014).
- Ouspenskaia, T., Matos, I., Mertz, A. F., Fiore, V. F. & Fuchs, E. WNT-SHH antagonism specifies and expands stem cells prior to niche formation. *Cell* **164**, 156–169 (2016).
- Zhang, G. et al. Decorin regulates assembly of collagen fibrils and acquisition of biomechanical properties during tendon development. *J. Cell. Biochem.* **98**, 1436–1449 (2006).
- Grillo, H. C., Watts, G. T. & Gross, J. Studies in wound healing: I. Contraction and the wound contents. *Ann. Surg.* **148**, 145–160 (1958).
- Watts, G. T., Grillo, H. C. & Gross, J. Studies in wound healing: II. The role of granulation tissue in contraction. *Ann. Surg.* **148**, 153–160 (1958).
- De Wever, O. et al. Critical role of N-cadherin in myofibroblast invasion and migration in vitro stimulated by colon-cancer-cell-derived TGF-beta or wounding. *J. Cell Sci.* **117**, 4691–4703 (2004).
- Burke, J. P., Cunningham, M. F., Sweeney, C., Docherty, N. G. & O'Connell, P. R. N-cadherin is overexpressed in Crohn's stricture fibroblasts and promotes intestinal fibroblast migration. *Inflamm. Bowel Dis.* **17**, 1665–1673 (2011).
- Hinz, B., Pittet, P., Smith-Clerc, J., Chaponnier, C. & Meister, J. J. Myofibroblast development is characterized by specific cell-cell adhesion junctions. *Mol. Biol. Cell* **15**, 4310–4320 (2004).
- Gritsenko, P. G. et al. p120-catenin-dependent collective brain infiltration by glioma cell networks. *Nat. Cell Biol.* **22**, 97–107 (2020).
- Adstrum, S., Hedley, G., Schleip, R., Stecco, C. & Yucesoy, C. A. Defining the fascial system. *J. Bodyw. Mov. Ther.* **21**, 173–177 (2017).
- Craciun, F. L. et al. RNA sequencing identifies novel translational biomarkers of kidney fibrosis. *J. Am. Soc. Nephrol.* **27**, 1702–1713 (2016).
- Black, M. et al. FOXF1 inhibits pulmonary fibrosis by preventing CDH2-CDH11 cadherin switch in myofibroblasts. *Cell Rep.* **23**, 442–458 (2018).
- Lodyga, M. et al. Cadherin-11-mediated adhesion of macrophages to myofibroblasts establishes a profibrotic niche of active TGF-beta. *Sci. Signal.* **12**, eaao3469 (2019).
- Schneider, D. J. et al. Cadherin-11 contributes to pulmonary fibrosis: potential role in TGF-beta production and epithelial to mesenchymal transition. *FASEB J.* **26**, 503–512 (2012).
- Peron, S. P., Freeman, J., Iyer, V., Guo, C. & Svoboda, K. A cellular resolution map of barrel cortex activity during tactile behavior. *Neuron* **86**, 783–799 (2015).
- Schiller, H. B. et al. Time- and compartment-resolved proteome profiling of the extracellular niche in lung injury and repair. *Mol. Syst. Biol.* **11**, 819 (2015).
- Cox, J. et al. Accurate proteome-wide label-free quantification by delayed normalization and maximal peptide ratio extraction, termed MaxLFQ. *Mol. Cell Proteom.* **13**, 2513–2526 (2014).
- Tyanova, S. et al. The Perseus computational platform for comprehensive analysis of (pro)teomics data. *Nat. Methods* **13**, 731–740 (2016).
- Naba, A. et al. The matrisome: in silico definition and in vivo characterization by proteomics of normal and tumor extracellular matrices. *Mol. Cell Proteomics* **11**, M111.014647 (2012).
- Shannon, P. et al. Cytoscape: a software environment for integrated models of biomolecular interaction networks. *Genome Res.* **13**, 2498–2504 (2003).
- Duan, Y. et al. The clustered, regularly interspaced, short palindromic repeats-associated endonuclease 9 (CRISPR/Cas9)-created MDM2 T309G mutation enhances vitreous-induced expression of MDM2 and proliferation and survival of cells. *J. Biol. Chem.* **291**, 16339–16347 (2016).
- Kennedy, P. J. et al. Class I HDAC inhibition blocks cocaine-induced plasticity by targeted changes in histone methylation. *Nat. Neurosci.* **16**, 434–440 (2013).
- Kostetskii, I. et al. Induced deletion of the N-cadherin gene in the heart leads to dissolution of the intercalated disc structure. *Circ. Res.* **96**, 346–354 (2005).

38. Lehr, H. A., Leunig, M., Menger, M. D., Nolte, D. & Messmer, K. Dorsal skinfold chamber technique for intravital microscopy in nude mice. *Am. J. Pathol.* **143**, 1055–1062 (1993).
39. Puspoki, Z., Storath, M., Sage, D. & Unser, M. Transforms and operators for directional bioimage analysis: a survey. *Adv. Anat. Embryol. Cell Biol.* **219**, 69–93 (2016).
40. Zhang, Y. et al. Collective cell migration has distinct directionality and speed dynamics. *Cell Mol. Life Sci.* **74**, 3841–3850 (2017).
41. Tseng, Q. et al. Spatial organization of the extracellular matrix regulates cell-cell junction positioning. *Proc. Natl Acad. Sci. USA* **109**, 1506–1511 (2012).
42. Lupperger, V., Buggenthin, F., Chapouton, P. & Marr, C. Image analysis of neural stem cell division patterns in the zebrafish brain. *Cytometry A* **93**, 314–322 (2018).

Acknowledgements

We thank Dr. Steffen Dietzel and the Core Facility Bioimaging at the Biomedical Centre of the Ludwig-Maximilians-Universität München for access and support with the multi-photon system. Gt(ROSA)26Sor^{tm1}(Cas9)^{Rad} mice were a kind gift from Prof. Roland Rad (Institute of Molecular Oncology and Functional Genomics, Technical University of Munich, Germany). Y.R. was supported by the Human Frontier Science Program Career Development Award (CDA00017/2016), the German Research Foundation (RI 2787/1–1 AOBJ: 628819), the Fritz-Thyssen-Stiftung (2016–01277), and the European Research Council Consolidator Grant (ERC-CoG 819933). D.C.-G. was supported by the Consejo Nacional de Ciencia y Tecnología (CONACYT) and the Deutscher Akademischer Austauschdienst (DAAD). Q.Y., L.W. and J.L. were supported by the China Scholarship Council (CSC).

Author contributions

Y.R. outlined and supervised the research narrative and designed experiments. D.J. established the mouse and human SCAD assays, performed SCAD characterisation, FACS sorting and flow cytometric analysis, animal experiments, and human tissue analysis. S.C. and J.W. performed intravital imaging. S.C. and P.R. performed the live imaging, 3D imaging, and cell tracking analysis. D.C.-G. performed the fractal and PIV analyses. P.R. performed the intravital vector field and contour trajectory analyses. D.C.G., P.R. and Q.Y. performed the SCAD chimera assay and Exherin experiment. S.K.G., P.R., M.M.-H. and V.R. cloned and produced the AAV6-NcadgRNA-GFP, AAV6-Cre-GFP and AAV6-GFP viral particles. J.W. provided veterinary advice and prepared animal experiment protocols. U.M. and T.V. collected patients' consents and thereafter the primary human tissue samples, and assisted with translational and clinical advice. H.Y., L.W. and J.L. assisted with mouse and human tissue preparation for SCAD assays and immunostaining. C.H.M. and H.B.S. performed proteomic

analysis. V.L. and C.M. performed the velocity and similarity analysis of cell tracking data. D.J. and Y.R. wrote the manuscript.

Funding

Open Access funding enabled and organised by Projekt DEAL.

Competing interests

The authors declare no competing interests.

Additional information

Supplementary information is available for this paper at <https://doi.org/10.1038/s41467-020-19425-1>.

Correspondence and requests for materials should be addressed to Y.R.

Peer review information *Nature Communications* thanks Ayman Grada, James Stewart and the other, anonymous, reviewer(s) for their contribution to the peer review of this work.

Reprints and permission information is available at <http://www.nature.com/reprints>

Publisher's note Springer Nature remains neutral with regard to jurisdictional claims in published maps and institutional affiliations.



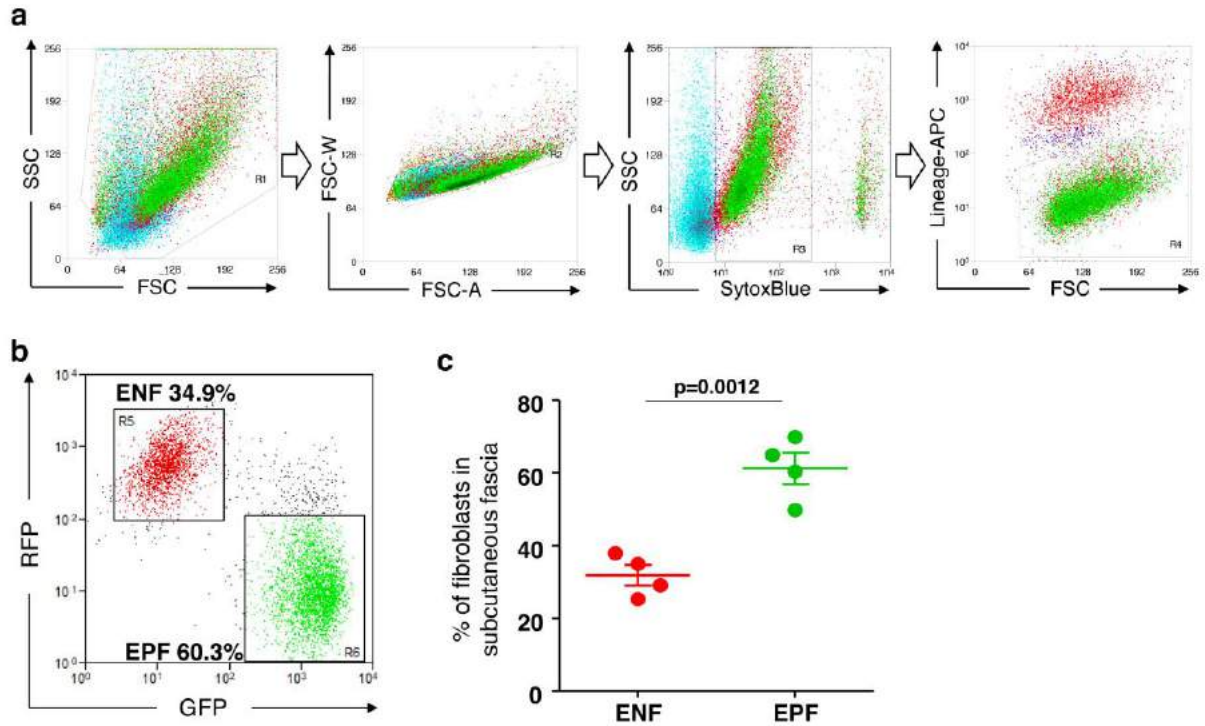
Open Access This article is licensed under a Creative Commons Attribution 4.0 International License, which permits use, sharing, adaptation, distribution and reproduction in any medium or format, as long as you give appropriate credit to the original author(s) and the source, provide a link to the Creative Commons license, and indicate if changes were made. The images or other third party material in this article are included in the article's Creative Commons license, unless indicated otherwise in a credit line to the material. If material is not included in the article's Creative Commons license and your intended use is not permitted by statutory regulation or exceeds the permitted use, you will need to obtain permission directly from the copyright holder. To view a copy of this license, visit <http://creativecommons.org/licenses/by/4.0/>.

© The Author(s) 2020

Injury triggers fascia fibroblast collective cell migration to drive scar formation through N-cadherin

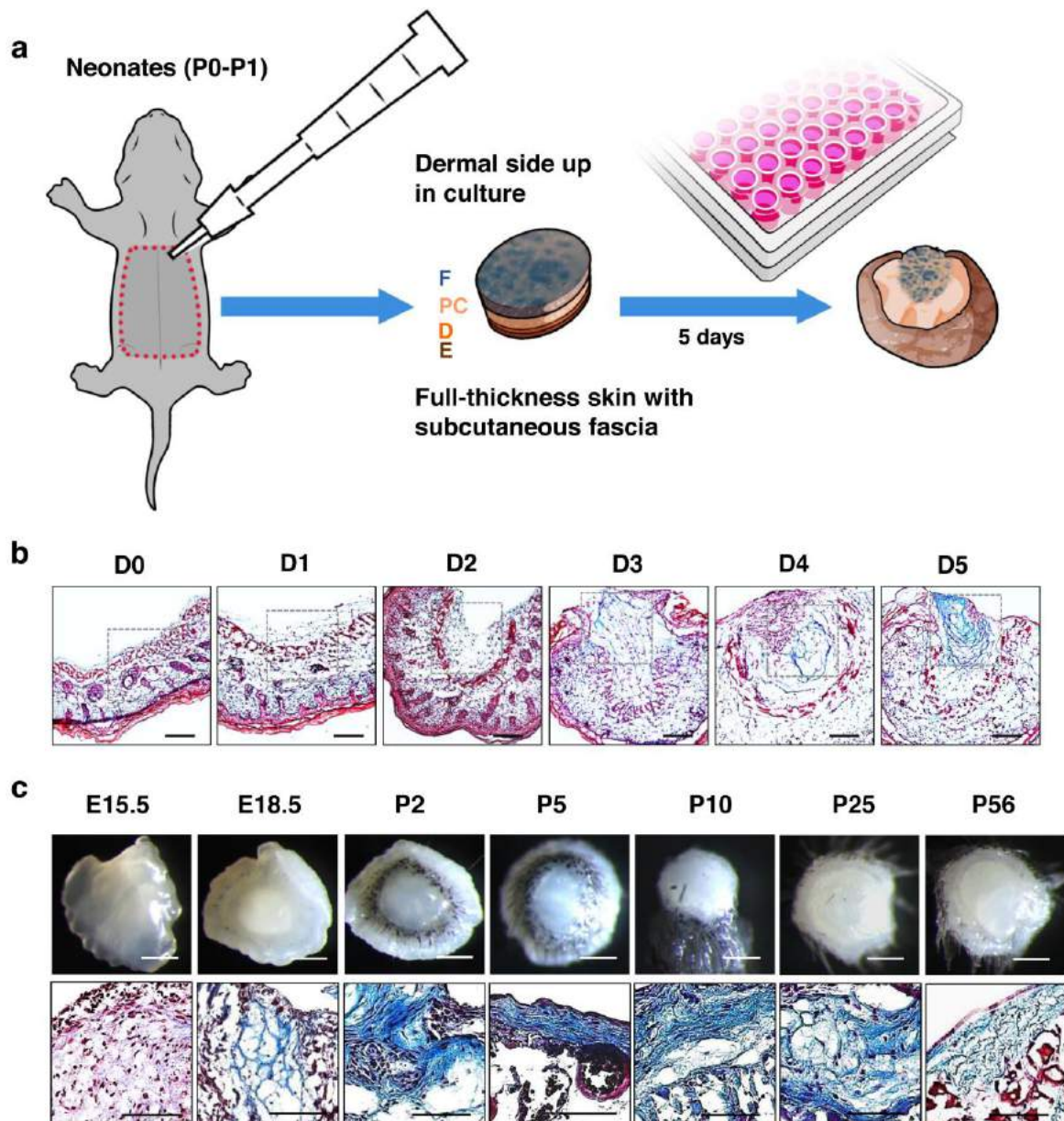
Dongsheng Jiang^{1,ξ}, Simon Christ^{1,ξ}, Donovan Correa-Gallegos^{1,ξ}, Pushkar Ramesh^{1,ξ}, Shruthi Kalgudde Gopal¹, Juliane Wannemacher¹, Christoph H. Mayr², Valerio Lupperger³, Qing Yu¹, Haifeng Ye¹, Martin Mück-Häusl¹, Vijayanand Rajendran¹, Li Wan¹, Juan Liu¹, Ursula Mirastschijski^{4,5}, Thomas Volz⁶, Carsten Marr³, Herbert B. Schiller^{2,7}, Yuval Rinkevich^{1,7,*}

SUPPLEMENTARY INFORMATION



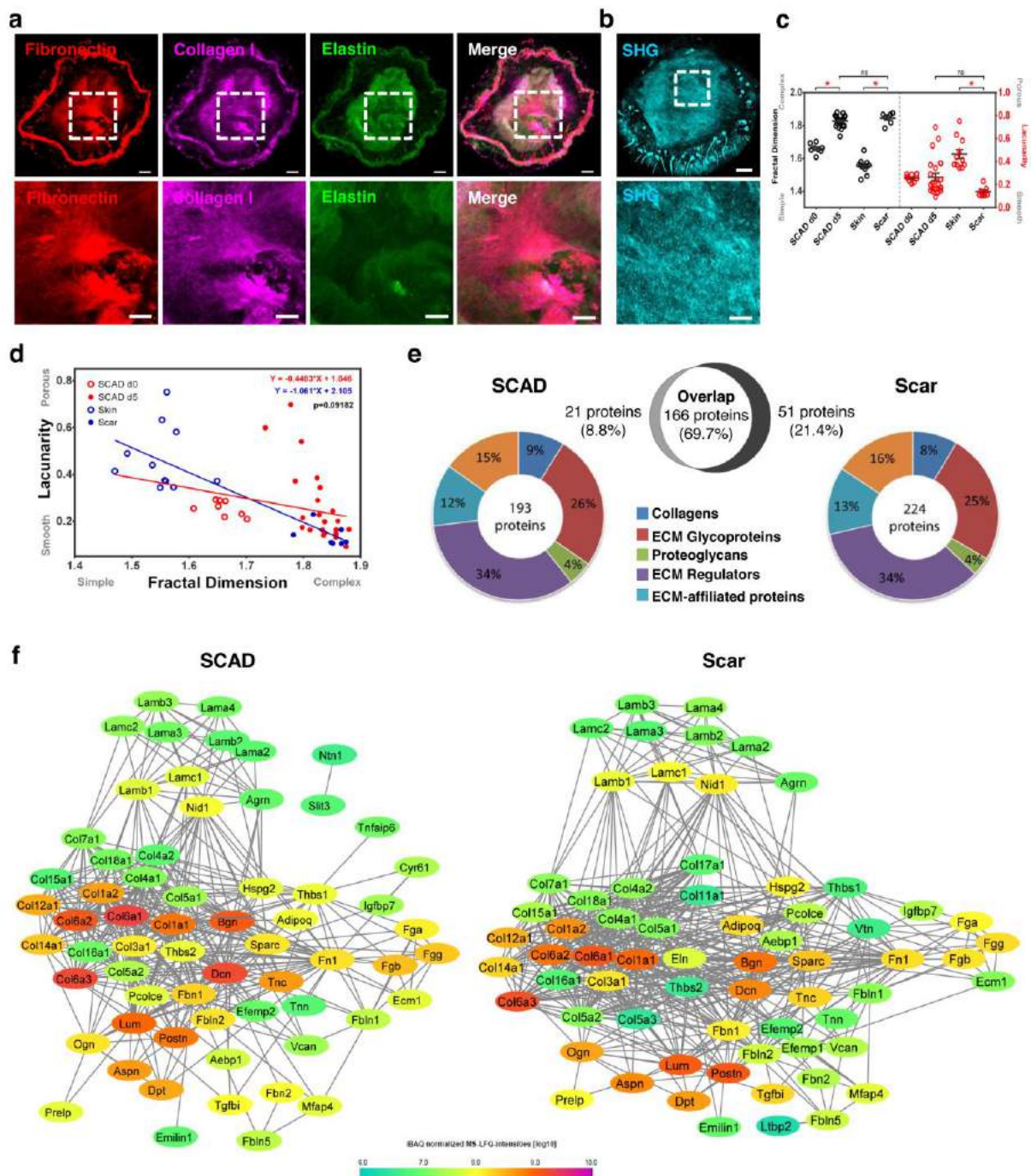
Supplementary Figure 1. EPF and ENF composition in subcutaneous fascia.

a, Subcutaneous fascia was separated from the back-skin of *En1^{Cre};R26^{mTmG}* neonates (P0-P1). Single cell suspension was prepared from the pooled fascia and subjected to flow cytometric analysis. Sytox Blue was used to exclude dead cells, and APC-conjugated lineage markers (CD45, CD31, Ter119, EpCAM, Tie-2, Lyve-1) were used to exclude non-fibroblastic cells. **b**, in living Lin⁻ population, GFP⁺RFP⁻ cells were gated as EPFs, and GFP⁻RFP⁺ cells were gated as ENFs. **c**, percentages of ENFs and EPFs in subcutaneous fascia. Mean ± SD, unpaired two-tailed *t*-test, $p=0.0012$, $n=4$.



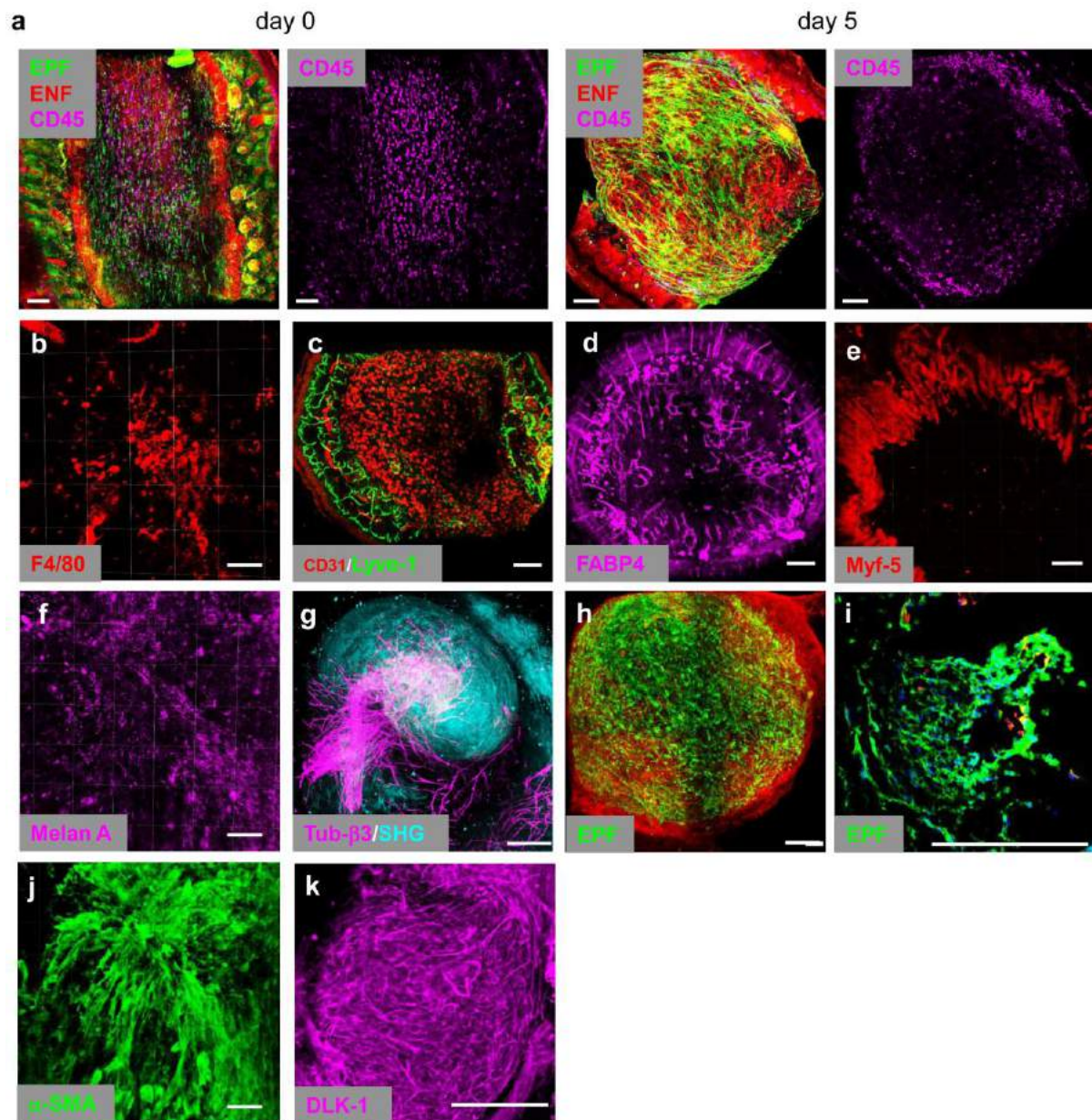
Supplementary Figure 2. SCAD model.

a, Key elements of the SCAD assay include (1) back-skin from new-born mice (postnatal day 0-1) for uniform scar formation, (2) full-thickness skin biopsy including subcutaneous fascia, (3) culturing with fascia side up. E, epidermis; D, dermis; PC, panniculus carnosus; F, subcutaneous fascia. **b**, Masson's trichrome staining of cryosections of SCADs from day 0 to day 5 of culture. Scale bars = 200 μ m. **c**, SCADs from mice at various development stages. Whole-mount images (upper panel, scale bars = 500 μ m) and Masson's trichrome staining (lower panel, scale bars = 200 μ m) of SCADs using back-skin from embryos (E15.5, E18.5), new-borns (P2), juveniles (P5, P10, P25) to adults (P56).



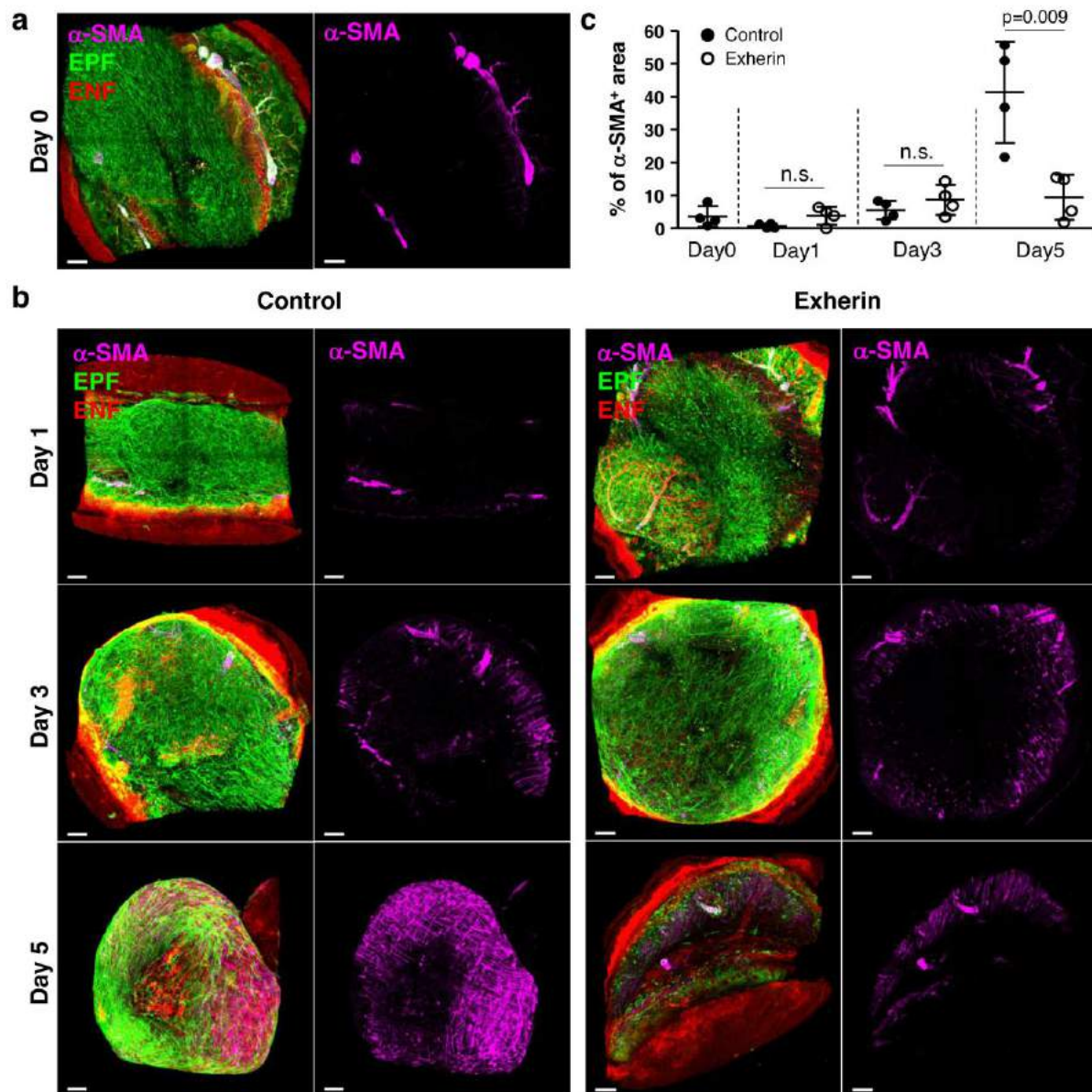
Supplementary Figure 3. SCAD recapitulates characteristics of *in vivo* fascia scar.

a, 3D immunostaining of fibronectin (red), collagen I (magenta) and elastin (green) in SCADs at low (upper panel) and high (lower panel) magnification. **b**, fibrillary collagens represented by second harmonic generation (SHG, cyan) signal in SCADs at low (upper) and low (lower) magnification. **c**, fractal dimension (left) and lacunarity (right) of day0 SCAD, day5 SCAD, *in vivo* skin, and *in vivo* scars. Mean \pm SD, n=7/22/11/7, One-way ANOVA Tukey's test. *, p=0.0001; ns, not significant. **d**, regression lines showing similar changes in fractal values between SCAD and *in vivo* scars. **e**, 4438 proteins were identified by proteomic analysis. When filtered for Matrisome proteins, 193 proteins in SCADs and 224 proteins in *in vivo* scars remained, respectively. The pie chart shows the similar percentages of Matrisome proteins in the indicated categories and the Venn diagram shows the overlapping Matrisome proteins of SCAD and *in vivo* scars. **f**, a protein-protein interaction network showing the similarity of matrix proteins between SCAD and *in vivo* scars. The colour coding indicates the abundance of proteins. Scale bars: a, b upper panel = 100 μ m, lower panel = 30 μ m.



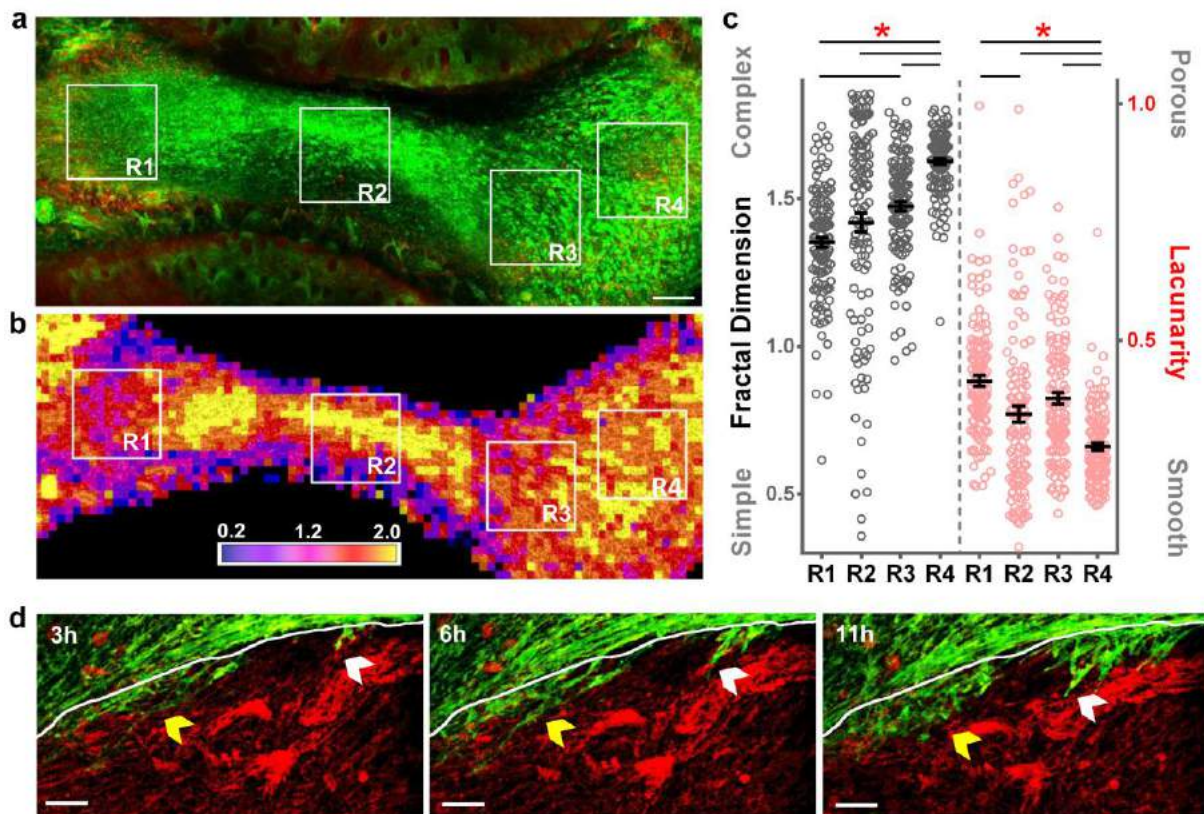
Supplementary Figure 4. Cellular component of SCAD.

a, 3D immunolabeling of CD45 (magenta) in day0 and day5 SCADs. b-g, 3D immunolabeling of F4/80 (b), CD31 (red) and Lyve-1 (green) (c), FABP4 (d), Myf-5 (e), Melan A (f), and Tubulin β3 (magenta) and SHG (cyan) (g) in SCADs. h, i, 3D (h) and 2D (i) fluorescence images of *En1*^{Cre};*R26*^{mTmG} SCAD, EPFs in green. j, k, 3D immunolabeling of α-SMA (j) and DLK-1 (k) in SCAD. Images are representative of at least three biological replicates. Scale bars = 100 μm.



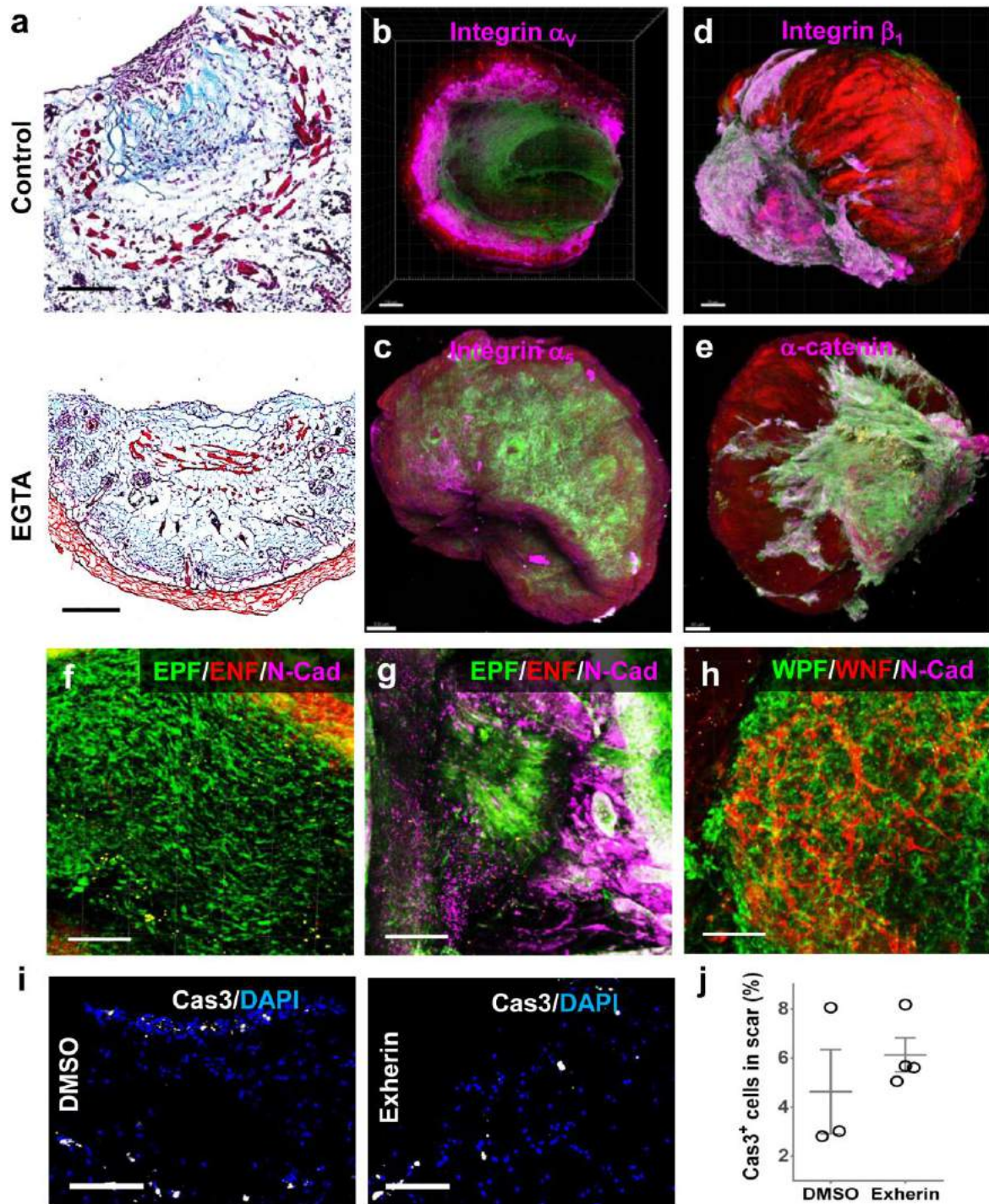
Supplementary Figure 5. α -SMA expression in SCAD.

3D immunolabeling of α -SMA in *En1*^{Cre}, *R26*^{mTmG} SCAD before culture (**a**) or cultured 1, 3, 5 days with or without 500 μ g/ml Exherin treatment (**b**). α -SMA in magenta, EPFs in green, and ENFs in red. **c**, quantitative analysis of percentage of α -SMA⁺ area in respective SCAD. Mean \pm SD, unpaired two-tailed *t*-test, *p*=0.009, *n* = 4. Scale bars: 100 μ m.



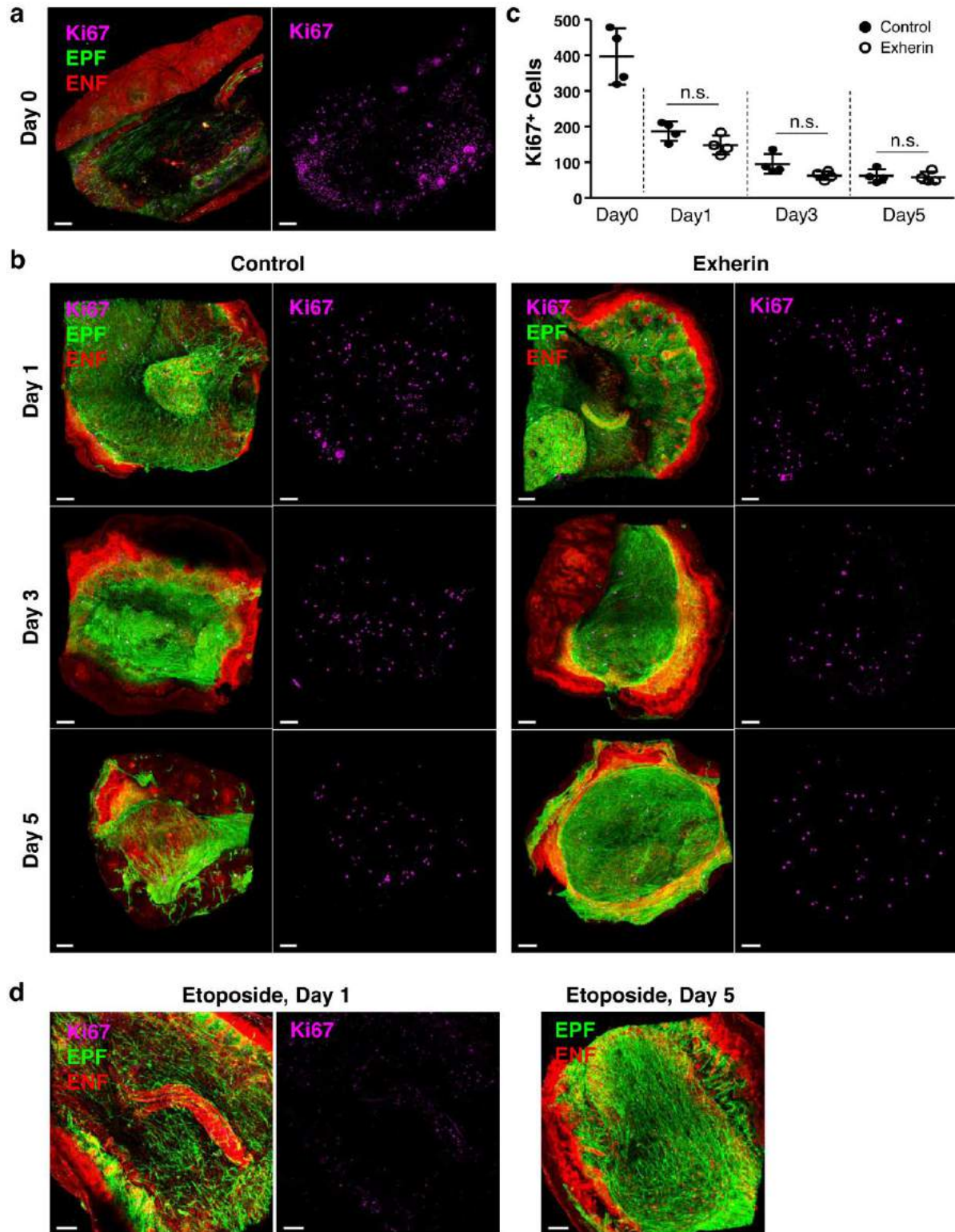
Supplementary Figure 6. Fascia EPFs aggregate in groups and migrate collectively at the onset of scarring.

a, snapshot of live imaging (0-24 h) of *En1^{Cre};R26^{mTmG}* SCAD at 24 h in culture. **b**, fractal analysis of EPFs (GFP channel). Colour code indicates fractal dimension (FD) values from low (dark) to high (bright). **c**, FD (left) and lacunarity (right) values of regions R1-R4. Mean \pm SEM of all subsampled values in each region. One-way ANOVA, Tukey's multiple comparisons test, * $p=0.001$, $n=121$ samples. **d**, snapshots (3h, 6h, 11h) of live imaging of a chimeric SCAD showing the migration of fascia EPF aggregates (Supplementary Movie 3). White lines indicate the border between the outer *En1^{Cre};R26^{mTmG}* SCAD and inner grafted RFP only SCAD. The arrows indicate the invasion of fascia EPF aggregates into the inner region. The yellow and white arrows indicate two independent EPF aggregates. Scale bars: a = 100 μm ; d = 50 μm .



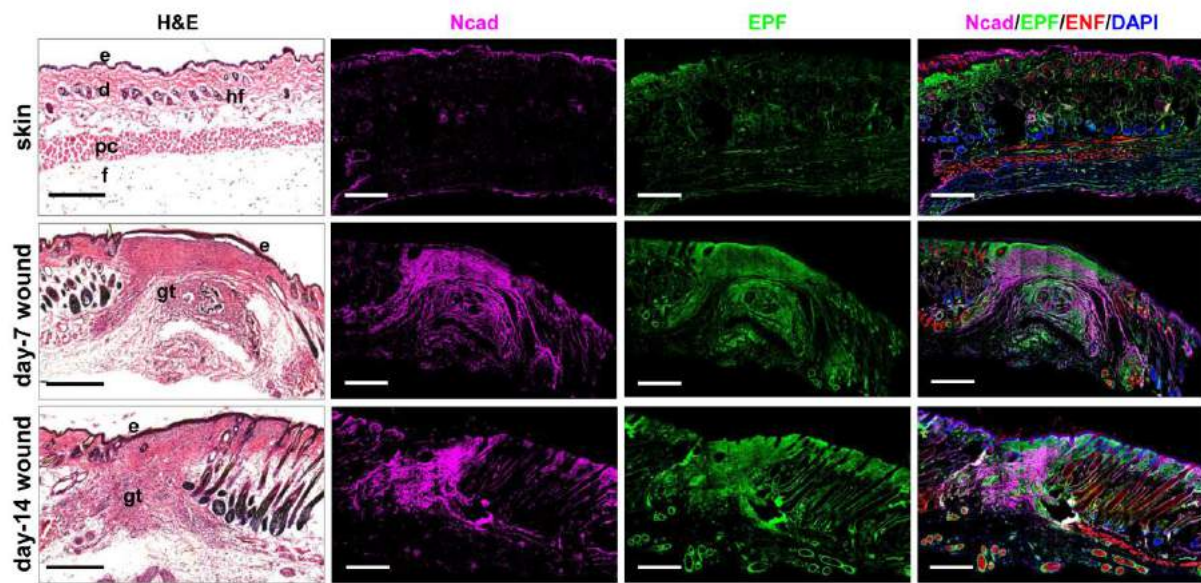
Supplementary Figure 7. N-cadherin mediated cellular adhesion of EPFs is essential for scar formation.

a, Masson's trichrome staining of control and 0.5 mM EGTA treated SCAD. **b-e**, 3D immunolabeling of integrin α_V (**b**), integrin α_5 (**c**), integrin β_1 (**d**), and α -catenin (**e**) in *En1^{Cre};R26^{mTmG}* SCAD. **f-h**, 3D immunostaining of N-cadherin (magenta) in day0 (**f**) and day2 (**g**) *En1^{Cre};R26^{mTmG}* dorsal SCAD, and day4 *Wnt1^{Cre};R26^{mTmG}* oral SCAD (**h**). **i**, immunostaining of active caspase-3 in scar area of DMSO or 500 μ g/ml Exherin treated SCAD. Cell nuclei were stained with DAPI. **j**, percentages of active caspase-3⁺ cells in scar area of DMSO or Exherin treated SCAD. $n=3/4$, $p=0.4066$, unpaired two-tailed t -test. Scales: **a** = 200 μ m; **b** = 150 μ m; **c, f-i** = 100 μ m; **d** = 70 μ m; **e** = 80 μ m.



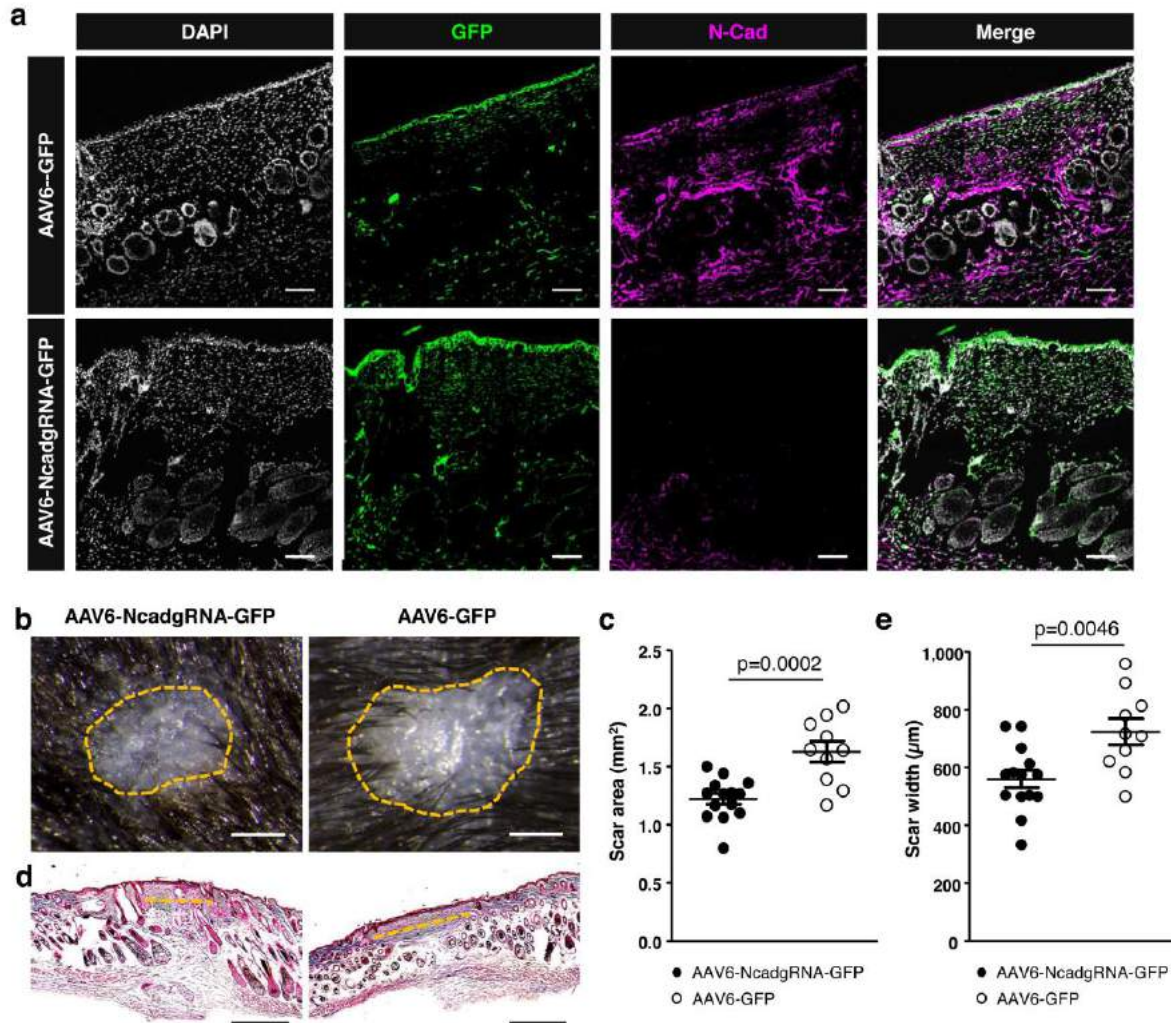
Supplementary Figure 8. Ki67 expression in SCAD.

3D immunolabeling of Ki67 in *En1^{Cre},R26^{mTmG}* SCAD before culture (a) or cultured 1, 3, 5 days with or without 500 μ g/ml Exherin treatment (b). Ki67 in magenta, EPFs in green, and ENFs in red. c, quantitative analysis of number of Ki67⁺ cells in respective SCAD. Mean \pm SD, unpaired two-tailed *t*-test, *n* = 4; n.s., not significant. d, SCAD treated with 100 μ M etoposide at day 1 and 5 after culture. Scale bars: 100 μ m.



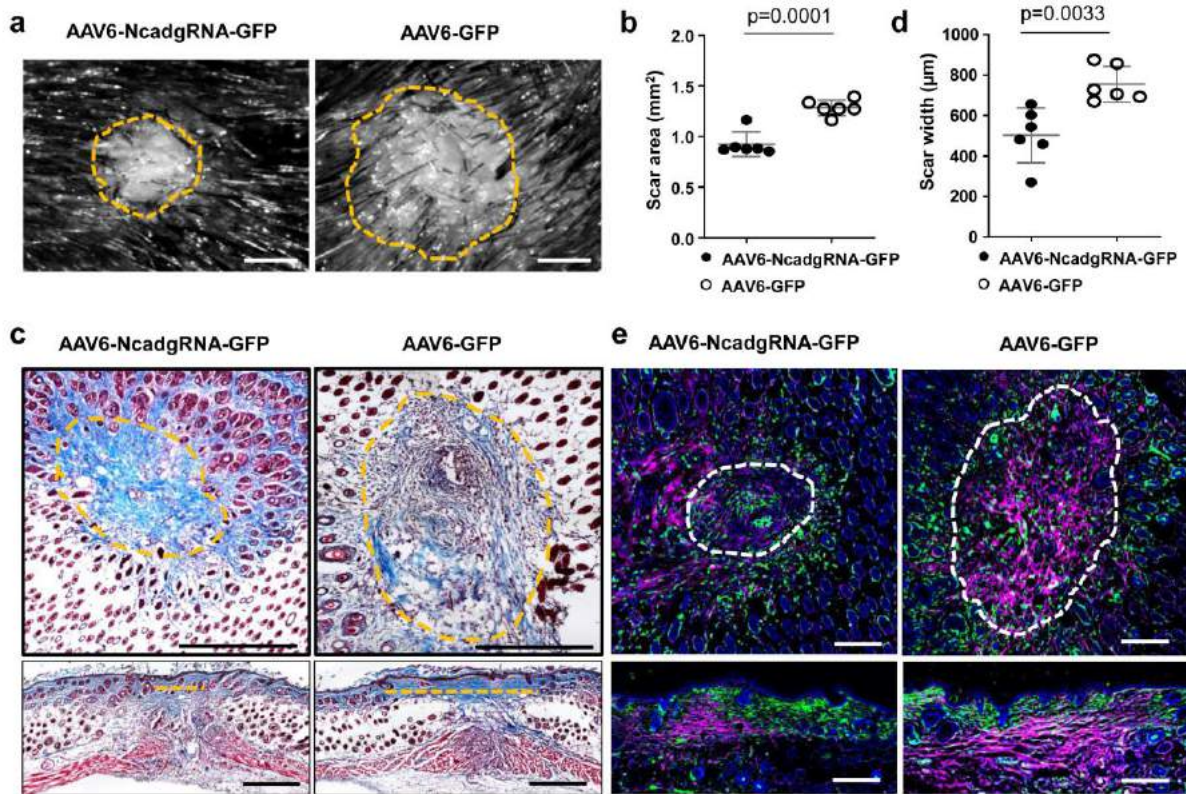
Supplementary Figure 9. N-cadherin expression is elevated in EPFs in physiological wounds.

H&E staining and immunolabeling of N-cadherin (magenta) in skin and *in vivo* wounds at day 7 and day 14 after wounding. EPFs showed in green. e, epidermis; d, dermis; pc, panniculus carnosus; hf, hair follicle; f, fascia; gt, granulation tissue. Scale bars = 500 μ m.



Supplementary Figure 10. Local knockout of N-cadherin reduces scarring with full-body Cas9 mouse model.

Local knockout of N-cadherin in wounds on full-body Cas9 ($R26^{Cas9}$) mice by AAV6 viral particle expressing guide RNA specific to mouse N-cadherin (AAV6-NcadgRNA-GFP). AAV6-GFP transduced wounds served as controls. **a**, immunofluorescence images of scars transduced with AAV6-GFP control virus (upper panel) or with AAV6-NcadgRNA-GFP virus (lower panel), harvested at 14-dpi. **b**, representative stereomicroscopic images of AAV6-NcadgRNA-GFP and AAV6-GFP treated scars at 14-dpi. The yellow dotted lines indicate the scar edges. **c**, quantification of scar area based on histomorphometric analysis. Mean \pm SEM, $n=14/10$, $p=0.0002$, unpaired two-tailed t -test. **d**, Masson's trichrome staining of AAV6-NcadgRNA-GFP and AAV6-GFP treated scars. The orange dotted lines indicate scar width. **e**, quantification of scar width based on histomorphometric analysis. Mean \pm SEM, $n=14/10$, $p=0.0046$, unpaired two-tailed t -test. Scale bars: a = 100 μ m; b, d = 500 μ m.



Supplementary Figure 11. Local knockout of N-cadherin in EPFs reduces scarring with Cas9 knock-in mouse model.

Knockout of N-cadherin in EPFs around wounds on *En1*^{Cre}*R26*^{Cas9-knockin} mice by AAV6 viral particle expressing guide RNA specific to mouse N-cadherin (AAV6-NcadgRNA-GFP). AAV6-GFP transduced wounds served as controls. **a**, representative stereomicroscopic images of AAV6-NcadgRNA-GFP and AAV6-GFP treated scars at 14-dpi. The dash lines indicate the scar edge. **b**, quantification of scar area based on histomorphometric analysis. Mean \pm SD, n=6, p=0.0001, unpaired two-tailed *t*-test. **c**, Masson's trichrome stained transverse (upper panel) and vertical (lower panel) sections from AAV6-NcadgRNA-GFP and AAV6-GFP treated scars. The dash lines indicate scar edge or width. **d**, quantification of scar width based on histomorphometric analysis. Mean \pm SD, n=6, p=0.0033, unpaired two-tailed *t*-test. **e**, immunolabeling of N-cadherin on transverse (upper panel) or vertical (lower panel) sections of scars. GFP indicates transduced cells. Dash lines outline the scar edges. Scale bars: 500 μ m.

Appendix: Publication III and IV

Publication III

Correa-Gallegos D, Jiang D, Christ S, **Ramesh P**, Ye H, Wannemacher J, Gopal SK, Yu Q, Aichler M, Walch A, Mirastschijski U, Volz T, Rinkevich Y. Patch repair of deep wounds by mobilized fascia. *Nature*. 2019;576(7786):287-292.

In the above work, my contributions include 3-D multiphoton imaging to visualize basic structural features of murine subcutaneous fascia. This includes orientation and localization of EPF and its associated fascial matrix in a 3-D space. The matrix diversity or ECM profile were visualized using label-free second harmonic generation approach (Figure 3a and extended data Figure 2f).

Related publication not included in the thesis

Fischer A, Koopmans T, **Ramesh P**, Christ S, Strunz M, Wannemacher J, Aichler M, Feuchtinger A, Walch A, Ansari M, Theis FJ, Schropp K, Hadian K, Neumann PA, Schiller H, Rinkevich Y. Post-surgical adhesions are triggered by calcium-dependent membrane bridges between mesothelial surfaces. *Nature Communications* **11**, 3068 (2020).

<https://doi.org/10.1038/s41467-020-16893-3>

Patch repair of deep wounds by mobilized fascia

<https://doi.org/10.1038/s41586-019-1794-y>

Received: 28 February 2019

Accepted: 30 October 2019

Published online: 27 November 2019

Donovan Correa-Gallegos^{1,7}, Dongsheng Jiang^{1,7}, Simon Christ¹, Pushkar Ramesh¹, Haifeng Ye¹, Juliane Wannemacher¹, Shruthi Kalgudde Gopal¹, Qing Yu¹, Michaela Aichler², Axel Walch², Ursula Mirastschijski^{3,4}, Thomas Volz⁵ & Yuval Rinkevich^{1,6*}

Mammals form scars to quickly seal wounds and ensure survival by an incompletely understood mechanism^{1–5}. Here we show that skin scars originate from prefabricated matrix in the subcutaneous fascia. Fate mapping and live imaging revealed that fascia fibroblasts rise to the skin surface after wounding, dragging their surrounding extracellular jelly-like matrix, including embedded blood vessels, macrophages and peripheral nerves, to form the provisional matrix. Genetic ablation of fascia fibroblasts prevented matrix from homing into wounds and resulted in defective scars, whereas placing an impermeable film beneath the skin—preventing fascia fibroblasts from migrating upwards—led to chronic open wounds. Thus, fascia contains a specialized prefabricated kit of sentry fibroblasts, embedded within a movable sealant, that preassemble together diverse cell types and matrix components needed to heal wounds. Our findings suggest that chronic and excessive skin wounds may be attributed to the mobility of the fascia matrix.

Mammalian scarring occurs when specialized fibroblasts migrate into wounds to deposit plugs of extracellular matrix¹. Abnormal scarring results in either non-healing chronic wounds or aggravating fibrosis^{2–4}, which represent a high burden for patients and to the global healthcare system. In the US alone, costs related to impaired scarring amount to tens of billions of dollars per year⁵.

The origin of fibroblasts in wounds and the mechanism by which they act remain unclear⁶. Possible sources, such as papillary (upper) and reticular (lower) dermal layers⁷, pericytes⁸, adipocytes^{9,10} and bone-marrow derived monocytes¹¹ have been suggested. We previously demonstrated that all scars in the back skin derive from a distinct fibroblast lineage expressing the engrailed 1 gene (*En1*) during embryogenesis and we refer to these cells as *En1*-lineage positive fibroblasts (EPFs)^{12,13}. This lineage is present not only in the skin but also in the strata underneath, called fascia.

The fascia is a gelatinous viscoelastic membranous sheet that creates a frictionless gliding interface between the skin and the body's rigid structure below. Mouse back-skin fascia extends as a single sheet separated from the skin by the Panniculus carnosus (PC) muscle, whereas in humans back-skin there is no intervening muscle and the fascia consists of several thicker sheets that are continuous with the skin. In humans the fascia layers incorporate fibroblasts, lymphatics, adipose tissue, neurovascular sheets and sensory neurons^{14,15}.

Here we explored the fundamental mechanisms of scar formation by using matrix-tracing techniques, live imaging, genetic-lineage tracing and anatomic fate-mapping models. We identified the fascia as a major source of wound-native cells, including fibroblasts. Notably, we found that wound provisional matrix originates from prefabricated matrix in the fascia that homes in to open wounds as a movable sealant dragging along vasculature, immune cells and nerves, upwards into the skin.

Wound cells rise from fascia

To trace the origins of cells in wounds, we developed a fate-mapping technique by transplanting chimeric skin and fascia grafts into living animals (Fig. 1a and Methods).

At 14 days post-wounding (dpw), 80.04 ± 3.443% (mean ± s.e.m.) of the labelled cells in the wound originated from fascia (Fig. 1b). Fascia-derived cells filled the entire wound bordering the regenerated epidermis and even the surrounding dermis, making up 35.46 ± 4.938% of the total labelled cells within a 0.2 mm radius (Fig. 1b, c). ACTA2⁺ myofibroblasts (81.63 ± 12.84%), nerve cells, endothelial cells and macrophages within wounds were predominantly of fascia origin (Fig. 1d, e). Independently, in vivo labelling of the fascia showed same results (Extended Data Fig. 1a, Methods). Labelled cells populated the wounds and surrounding dermis at 14 dpw, whereas in uninjured controls, labelled cells remained in the fascia (Extended Data Fig. 1b). Up to 56.71 ± 9.319% of fascia-derived cells in wounds expressed classical fibroblast markers (Extended Data Fig. 1c). Labelled monocytes (macrophages), lymphatics, endothelium and nerves also derived from fascia (Extended Data Fig. 1d). Collectively, our two independent fate-mapping approaches demonstrate that fascia is a major reservoir of fibroblasts, endothelial cells macrophages and peripheral nerves that populate wounds following injury.

Fascia fibroblasts dictate scar severity

We then analysed the scar-forming EPFs across dermal and fascia compartments by using a TdTomato-to-GFP replacement reporter^{12,13} (*En1^{Cre};R26^{mTmG}*; see Methods). Fibroblasts were the predominant fascia cell type (71.1%), whereas dermis had a significantly lower fraction of

¹Group Regenerative Biology and Medicine, Institute of Lung Biology and Disease, Helmholtz Zentrum München, Munich, Germany. ²Research Unit Analytical Pathology, Helmholtz Zentrum München, Munich, Germany. ³Mira-Beau Gender Esthetics, Berlin, Germany. ⁴Wound Repair Unit, CBIB, Department of Biology and Biochemistry, University of Bremen, Bremen, Germany. ⁵Department of Dermatology and Allergology, School of Medicine, Klinikum rechts der Isar, Technical University of Munich, Munich, Germany. ⁶German Centre for Lung Research (DZL), Munich, Germany. ⁷These authors contributed equally: Donovan Correa-Gallegos, Dongsheng Jiang. *e-mail: yuval.rinkevich@helmholtz-muenchen.de

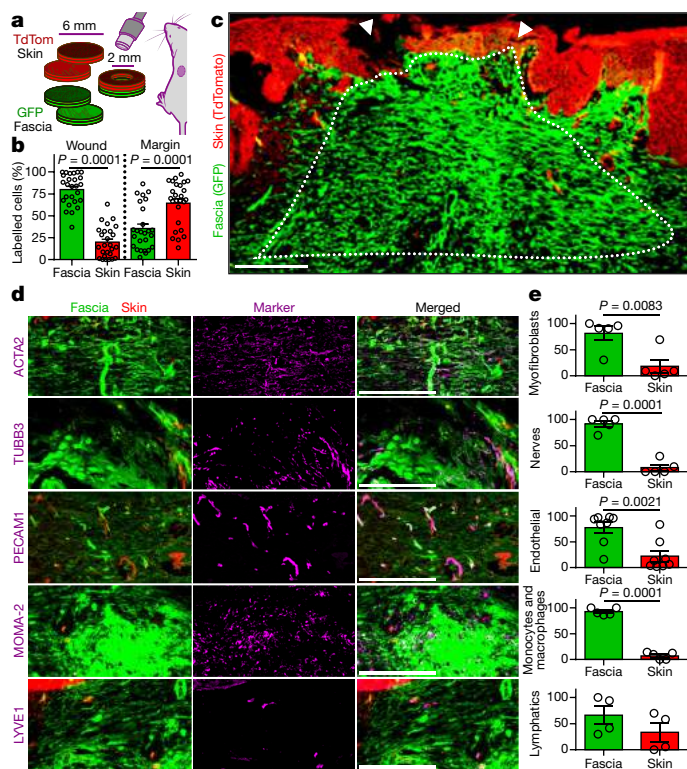


Fig. 1 | Fascia is a major cellular source for wounds. **a**, Generation of 6-mm diameter chimeric grafts with an inner 2-mm wound to determine contributions of dermis and fascia. **b**, Percentages of TdTomato⁺ or GFP⁺ cells from total labelled cells in the wound and wound margin. Data are mean \pm s.e.m., $n = 26$ images from 4 biological replicates. One-way ANOVA, multiple comparison Tukey's test, 95% confidence interval (CI). **c**, Wound showing skin- and fascia-derived cells at 14 dpw. **d**, e, Immunolabelling and contributions of myofibroblasts (ACTA2), nerves (TUBB3), blood vessels (PECAM1), monocytes or macrophages (MOMA-2) and lymphatic cells (LYVE1). Data are mean \pm s.e.m.; $n = 4$ (LYVE1), 5 (ACTA2, TUBB3 and MOMA-2) or 8 (PECAM1) images from 4 biological replicates. Unpaired two-tailed t -test, 95% CI. Dotted lines delimit the wound. Arrowheads indicate injury site. Scale bars, 200 μ m. TdTom, TdTomato.

fibroblasts (56.4%, Extended Data Fig. 2a, b). Within this population, there were twice as many EPFs as En1-naïve fibroblasts (ENFs) in the fascia (61.2% and 31.8%, respectively). In dermis, there was a sixfold excess of EPFs (83.13% EPFs versus 12.78% ENFs; Extended Data Fig. 2c, d). Fascia was also enriched in regenerative cell types such as endothelial cells and lymphatics, whereas populations of macrophages and nerve cells were similar in both compartments (Extended Data Fig. 2e). Thus, a higher proportion of fibroblasts, endothelial cells and lymphatic cells and a lower EPF to ENF ratio distinguishes the fascia from dermis.

Two-photon microscopy revealed that fascia EPFs assemble in monolayers of consecutive perpendicular sheets across the dorsal–ventral axis (Extended Data Fig. 2f, Supplementary Video 1). EPFs populate the entire back in topographic continua extending from the fascia and traversing the PC (Extended Data Fig. 2g, h Supplementary Video 2). Regions where PC ended or where nerve bundles and blood vessels traversed the PC also showed continuums of EPFs without clear boundaries (Extended Data Fig. 2i, j). To test whether fascia EPFs could access dermal layers upon injury, we generated superficial excisional wounds. Aggregates of EPFs rising into open wounds from fissures in the PC were observed after only 3 dpw (Extended Data Fig. 2k, Supplementary Video 3). Collectively, our observations suggest that fascia EPFs easily traverse upwards into dermal layers during wounding and are unobstructed by the PC muscle.

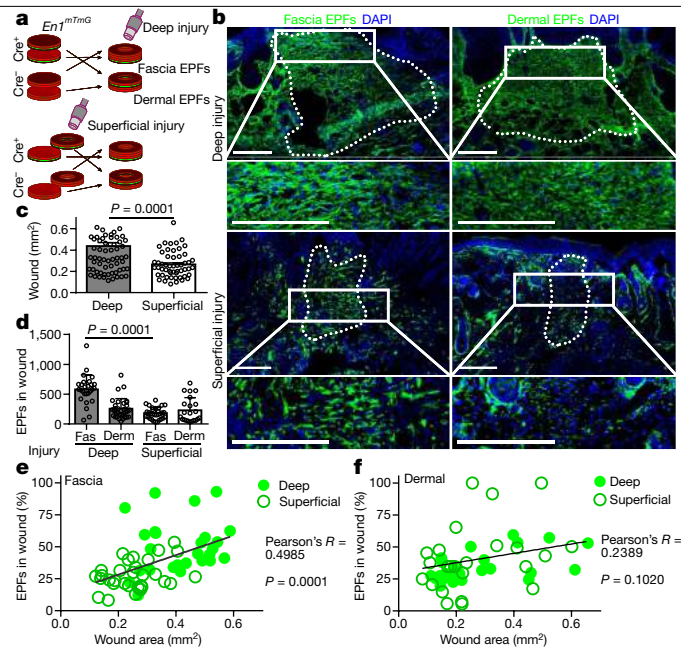


Fig. 2 | Fascia EPFs dictate scar severity. **a**, Dermal versus fascia EPFs chimeric grafts. Chimeric grafts were prepared as in Fig. 1a, using the EPF reporter line *En1^{Cre};R26^{mTmG}* combined with Cre-negative littermate samples to trace EPFs in each compartment. **b**, Images showing fascia EPFs (left) or dermal EPFs (right) in wounds after a deep (top) or superficial injury (bottom). **c**, Wound size. Data are mean \pm s.e.m.; $n = 70$ (deep) and 53 (superficial) images analysed from 5 biological replicates. Unpaired, two-tailed t -test, 95% CI. **d**, Numbers of fascia and dermal EPFs. Data are mean \pm s.e.m.; $n = 27, 32, 27$ and 22 images analysed from 5 biological replicates. Unpaired, two-tailed t -test, 95% CI. **e, f**, Plots of EPF fractions and wound size from fascia (e) and dermal EPFs (f). $n = 57$ (e) and 48 (f) images analysed from 5 biological replicates. Two-tailed Pearson's R^2 correlation, 95% CI. Dotted lines delimit wounds. Scale bars, 200 μ m.

The size of a scar increases with the depth of the injury¹⁶. We therefore investigated whether this correlation can be attributed to fascia by analysing the extent of fibroblast contributions from the fascia and dermis in deep versus superficial wounds. For this, we combined genetic lineage-tracing (*En1^{Cre};R26^{mTmG}*) with our anatomic fate-mapping chimeric grafts and inflicted superficial or deep injuries (Fig. 2a, Methods). Fourteen days post-wounding, mean wound size of deep injuries was 1.7 times that of superficial injuries (Fig. 2b, c). There were twice as many fascia EPFs in deep wounds, whereas the number of dermal EPFs remained constant in both conditions (Fig. 2d). The abundance of fascia EPFs in the wound directly correlated with wound size and thus scar severity, whereas dermal EPFs showed no such correlation (Fig. 2e, f). No crossing of EPFs between these compartments was observed in uninjured controls, indicating that the influx of fascia EPFs was triggered by injury (Extended Data Fig. 3a, b).

Long-term tracing of fascia EPFs in wounds showed that they recede ten weeks after injury (Extended Data Fig. 3c). This desertion from mature scars occurred through an apoptosis-independent mechanism, indicated by a low rate of cell death (<5%) across earlier time points (Extended Data Fig. 3d, e).

We next sought to place fascia EPFs in the framework of known lineage markers used to define different populations of wound fibroblasts such as CD24, CD34, DPP4, DLK1 and LY6A^{7,10,12}. All markers were prominent in fascia EPFs and were surprisingly downregulated upon entering the wound in our graft experiments (Extended Data Fig. 4). Flow cytometry confirmed the higher expression of DPP4, ITGB1, LY6A and PDGFR α in fascia than in dermal fibroblasts (Extended Data Fig. 5a–c). Sorted fascia EPFs also revealed low cellular heterogeneity, with the population predominantly comprising LY6G⁺PDGFR α ⁺ (87.0%) and DPP4⁺ITGB1⁺

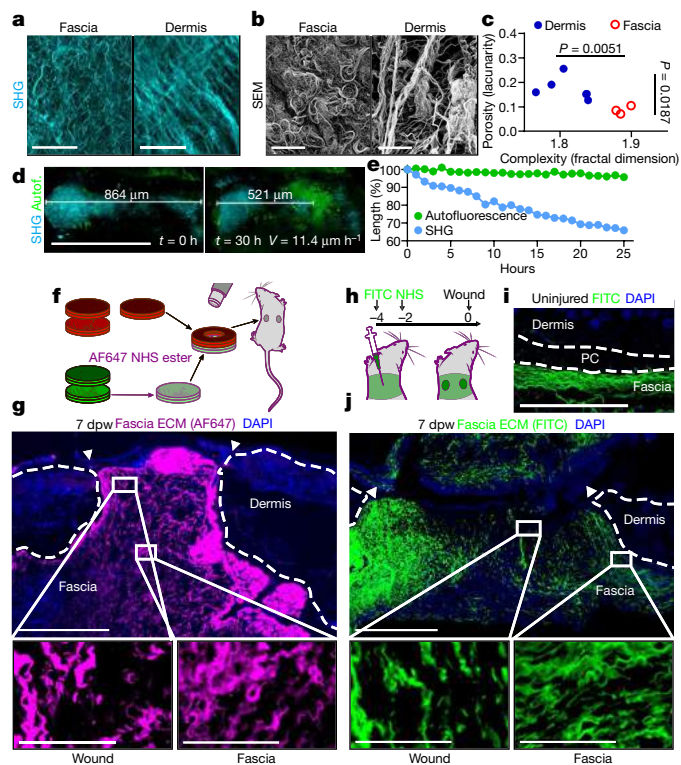


Fig. 3 | Fascia matrix steers into wounds. **a**, SHG (**a**) and SEM images (**b**) of fascia (left) and dermis (right) showing matrix arrangements, representative images of 3 biological replicates. **c**, Fractal dimension and lacunarity values from SHG images. $n = 6$ (dermis) and 3 (fascia) images analysed from 3 biological replicates. Unpaired two-tailed t -test, 95% CI. **d**, Time-lapse images of fascia in culture at time 0 (left) and 30 h (right). Representative video from at least three independent experiments. Autof., autofluorescence. **e**, Contraction rate from the SHG and autofluorescence. Data derived from Supplementary Video 4. **f**, Fascia matrix labelling with AF647 NHS ester in chimeric grafts. TdTomato and GFP reporter lines biopsies were used for the chimeric grafts as before. Only the matrix of the GFP-positive fascia compartment was labelled before transplantation. **g**, Images at 7 dpw showing fascia matrix covering the wound. Representative image of at least three biological replicates. **h**, In situ fascia matrix-tracing experiment using FITC NHS ester. Subcutaneous injections of FITC NHS ester were performed 4 and 2 days before wounding in the back-skin of wild-type mice to label the fascia matrix. **i**, Uninjured controls showing specificity of the labelling in fascia. Representative sample of at least three biological replicates. **j**, Images from 7 dpw showing fascia matrix covering the wound area. Representative samples of at least three biological replicates. Arrowheads indicate the original injury. Broken lines delimit dermis (**g** and **j**) or PC (**i**). Scale bars, 30 μm (**a**, **b**), 500 μm (**d**, **g**, **i**, **j**), and 100 μm (**g**, **j** magnified insets).

(72.8%) cells (Extended Data Fig. 5d). This broad marker convergence identifies fascia EPFs as the major source of wound fibroblasts.

Provisional matrix emerges from fascia matrix

We then looked at the fascia matrix itself. Second harmonic generation (SHG) signal and scanning electron micrographs (SEM) revealed profuse coiled collagen fibrils in the fascia, indicative of a relaxed and immature matrix (Fig. 3a, b). Fractal measurements¹³ of the fibre alignments showed a more condensed matrix configuration in fascia than the stretched and woven dermal matrix (Fig. 3c).

Given the immaturity of the fascia matrix, we checked whether it could work as a repository for scar tissue. We developed an incubation chamber that enabled live imaging of fascia biopsies over several days (Methods). Recording of SHG signals showed steering of the matrix at a rate of 11.4 $\mu\text{m h}^{-1}$ (Fig. 3d, e, Supplementary Video 4). Assuming

a similar rate in vivo, the fascia matrix could move about 2 mm in 7 days, accounting for the dynamics of provisional matrix deposition in mammals.

To test whether fascia matrix steers into wounds in vivo, we developed a method to trace the fascia matrix in our chimeric grafts using NHS esters. (Fig. 3f, Methods). Streams of traced matrix from the fascia extended upwards and plugged the open wounds from 7 dpw (Fig. 3g, Extended Data Fig. 6a, b). Fascia-derived matrix covered $74.78 \pm 12.94\%$ of total collagen content in the wound (Extended Data Fig. 6c). Our data indicated that individual fascia matrix fibres were not being pulled; instead, pliable matrix was extended upwards to mould the wound. Advanced wound stages showed a decline in label in specific regions of the wound, suggesting an active remodelling process of the fascia-derived matrix (Extended Data Fig. 6d–f, Supplementary Video 5).

We then tested whether dermal matrix could be steered by double labelling our chimeric grafts. Only the fascia matrix plugged deep injury wounds (Extended Data Fig. 6g–j), whereas dermal matrix remained immobile in deep and superficial injuries; the superficial injuries healed via de novo matrix deposition (Extended Data Fig. 6k, l).

To provide further evidence showing that fascia matrix migrates to open wounds, we labelled the fascia matrix in situ before injury (Fig. 3h, i, Methods). Labelled matrix made up most of the wound provisional matrix (Fig. 3j), which underwent remodelling during the first two weeks following injury (Extended Data Fig. 7a, b). Fractal measurements showed that fascia fibre interfaces expanded by 3 dpw, changing from a parallel sheet arrangement to a highly porous plug. This expansion was followed by contraction into thicker and more complex mature scar matrix architecture (Extended Data Fig. 7c–e). Surprisingly, traced matrix was also present in the eschar. Activated platelets infiltrated and clustered within fascia fibres before eschar formation (Extended Data Fig. 7f), indicating that the coagulation cascade occurs in parallel with fascia matrix steering.

EPFs steer fascia matrix into wounds

To test whether matrix steering from fascia is caused by EPFs, we blocked fascia by implanting an impermeable dual surface expanded polytetrafluoroethylene (ePTFE) membrane¹⁷ between the fascia and the PC in wounds of *En1^{cre};R26^{VT2/GK3}* mice (Fig. 4a, Methods). Surprisingly, wounds with implants remained completely open whereas sham controls closed within 21 days (Fig. 4b). After two months, EPFs trailed from the wound margins and under the membrane without generating scars (Fig. 4c, Extended Data Fig. 8a). Implants produced a transient inflammation that resolved even when the wound remained open. Two-month-old wounds with implants showed normal leukocyte and pro- and anti-inflammatory interleukins levels (Extended Data Fig. 8b–i), consistent with the clinical use of ePTFE as immunologically inert membranes. The coagulation cascade also was unaltered at the border between the dermis and the membrane (Extended Data Fig. 8j, k). These results indicate that the lack of scarring with ePTFE membranes does not reflect chronic inflammation or poor clotting, but rather a blockade of fascia steering mediated by the fascia fibroblasts. These findings further support the notion that scar tissue is mostly derived from the fascia, since dermal EPFs or dermal matrix are unable to repair wounds in the absence of fascia movements.

We next investigated whether mechanical separation between dermis and fascia alone, without barrier implants, would affect matrix steering and scar formation. To address this question, we performed full excisional wounds in wild-type mice and physically released the fascia below the PC around the wound (Fig. 4d). Wound closure from released-fascia wounds was significantly delayed, and wounds remained open early on, similarly to those documented following membrane implantations (Fig. 4e, f).

To definitively link fascia EPFs to matrix steering, we genetically ablated fascia EPFs using two separate strategies. First, we used a

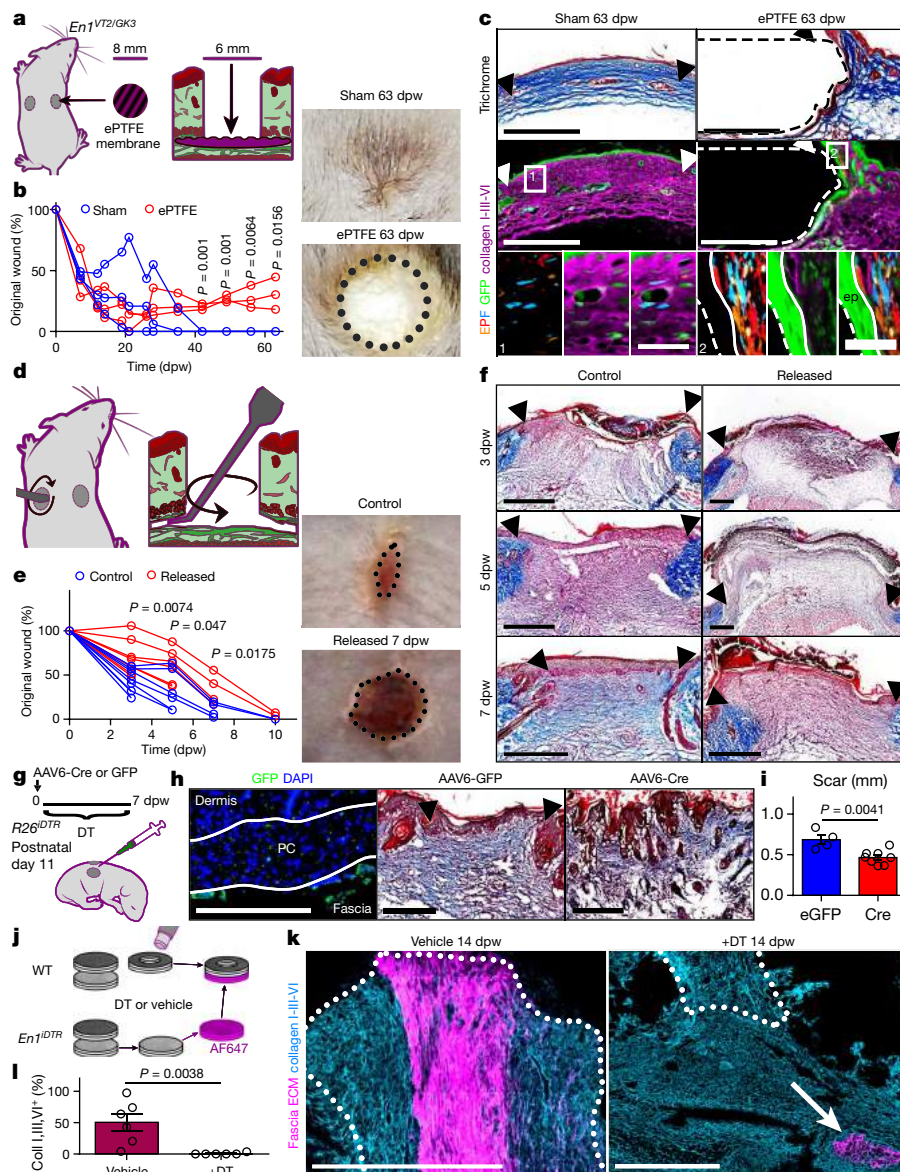


Fig. 4 | Fascia EPFs steer scar primordium into wounds. **a**, 8-mm diameter ePTFE membranes were implanted between the skin and fascia in fresh 6-mm diameter wounds to block fascia steering. **b**, ePTFE-implanted or sham wound closure (left) determined from photographs (right) at specified time points. Individual values, $n = 3$ biological replicates. Unpaired two-tailed t -test, 95% CI. **c**, Sham (left) or ePTFE-implanted (right) wounds at 63 dpw. Trichrome staining (top) and collagen immunolabelling (middle). Magnifications (1, 2 (bottom)) show multiclonal dermal EPFs. Representative images from 3 biological replicates. **d**, Fascia tissue around fresh 5-mm diameter wounds was mechanically separated from the skin above using a metal paddle. **e**, Fascia-released or control wound closure (left) determined from photographs (right) at specified time points. Individual values, $n = 8$ (0–3 dpw), 6 (5 dpw), 4 (7 dpw) and 2 (10 dpw) images from 8 biological replicates. Unpaired two-tailed t -test, 95% CI. **f**, Trichrome-stained wounds at 3, 5 and 7 dpw from control or fascia-

released wounds. Representative images from 8 biological replicates. **g**, Fascia cell depletion in $R26^{DTR}$ neonates. **h**, Fluorescence image (left) and trichrome-stained wounds at 7 dpw in GFP- (middle) or Cre-transduced (right) fascia. Representative images from 3 biological replicates. **i**, Scar-length measurements. Data are mean \pm s.e.m.; $n = 4$ and 8 sections from 3 biological replicates. Unpaired two-tailed t -test, 95% CI. **j**, Depletion of fascia EPFs in chimeric grafts with fascia matrix labelling. **k**, Immunolabelling for collagens, and fascia matrix in control (left) or DT-treated (right) grafts. Representative images from 3 biological replicates. **l**, Matrix-labelling coverage. Data are mean \pm s.e.m.; $n = 6$ sections from 3 biological replicates. Unpaired two-tailed t -test, 95% CI. Dashed lines delimit the implant. Dotted lines delimit the wound. Arrowheads indicate the original injury. Arrow indicates remaining labelled fascia matrix in DT-treated grafts. Scale bars, 50 μ m (c (1 and 2)), 200 μ m (h), and 500 μ m (c (main image), f, h, k).

transgenic line that expresses the diphtheria toxin receptor (DTR) in a Cre-dependent manner ($R26^{DTR}$), enabling us to deplete cells expressing Cre recombinase upon exposure to diphtheria toxin (DT). We thus generated Cre-expressing adeno-associated viral particles (AAV6-Cre) and injected them into the fascia of $R26^{DTR}$ pups underneath freshly made full excisional wounds (Fig. 4g). Scar size from AAV6-Cre transduced mice treated with DT were significantly smaller those from controls (Fig. 4h, i).

Second, we used $En1^{cre};R26^{DTR}$ double transgenic mice, in which DTR expression is restricted to EPFs, making them susceptible to

DT-mediated ablation. We corroborated the ablation of fascia EPFs in cultured biopsies 6 days after acute exposure to DT for 1 h. Effective dose of DT prevented the normal increase in collagen fibre density observed in control samples and decreased the cell density by 2.5 times (Extended Data Fig. 9a–c). Live imaging showed absence of any matrix steering after DT exposure (Extended Data Fig. 9d, e, Supplementary Video 6), confirming that fascia EPFs are essential for matrix steering.

Next, we created chimeric grafts using dermis from wild-type mice and fascia from $En1^{cre};R26^{DTR}$ mice. We ablated fascia EPFs using DT

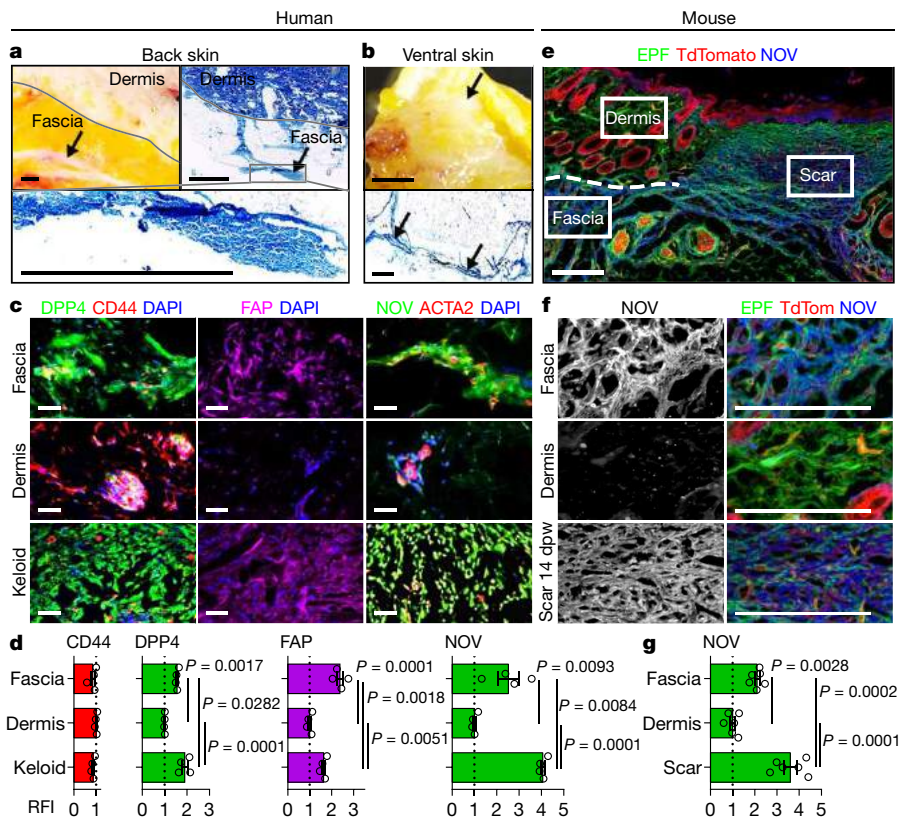


Fig. 5 | Marker signature in keloids and fascia. **a, b**, Macroscopic images and trichrome staining of human back (**a**) and abdominal (**b**) skin showing fascia layers embedded in subcutaneous tissue. Arrows indicate the fascia. Representative images from 4 independent samples. **c**, Immunolabelling for DPP4, CD44 and FAP, and NOV and ACTA2 in fascia, dermis and keloids of human back skin. **d**, Relative fluorescence intensity (RFI) in **c**, normalized to the dermis. Data are mean \pm s.e.m.; $n = 4$ images analysed from 4 biological

replicates. One-way ANOVA with Tukey's test, 95% CI. **e, f**, Immunostaining for NOV in *En1^{cre};R26^{mtmG}* 14 dpw scars. **g**, Relative fluorescence intensity in **f**, normalized to the dermis. Data are mean \pm s.e.m.; $n = 6$ images of 3 biological replicates. One-way ANOVA, Tukey's test, 95% CI. Dotted and broken lines delimit scar and fascia, respectively. Scale bars, 2 mm (**a, b**), 50 μ m (**c**) and 200 μ m (**e, f**).

and labelled the matrix before transplantation (Fig. 4j). Ablation of fascia EPFs prevented matrix steering into the wound (Fig. 4k, l) and instead labelled matrix remained in the fascia layer below. Together, our data demonstrate that fascia resident EPFs actively steer matrix to seal open wounds.

To check whether fibroblast proliferation preceded and was needed for matrix steering, we analysed the proliferation rate in our matrix-tracing experiments. Expansion of the fascia gel beneath the wound occurred during the first days after injury, whereas cell proliferation peaked after one week (Extended Data Fig. 10a–c), indicating that proliferation is not required for matrix steering. Furthermore, treatment with a proliferation inhibitor had no effect on fascia matrix steering in vitro (Extended Data Fig. 9f–k, Supplementary Video 7). Our results demonstrate that fascia matrix works as an expanding sealant that quickly clogs deep wounds independently of cell proliferation.

Fascia and keloid share marker signatures

Similar to mouse fascia matrix, human keloids present poorly structured and densely packed collagen fibres¹⁸. This motivated us to investigate the presence of fascia fibroblasts in keloid tissue. We screened for markers present in keloids and compared them with healthy dermis and the connective tissue in the subcutaneous space (fascia) of human skin across multiple anatomic locations (Fig. 5a, b). FAP and DPP4 were highly expressed in both fascia and keloids, with low expression in dermis. The fascia-restricted protein NOV was also prominently expressed in both human and mouse fascia, as well as in human keloids and mouse scars (Fig. 5c–g). This preservation of fascia markers across mouse

and human fascia and keloid scars suggests a common fascia origin for most human cutaneous scars.

Discussion

Current models of wound healing propose that dermal fibroblasts migrate into wounds and locally deposit matrix de novo onto the granulation tissue provided by the coagulation cascade. This provisional matrix is then remodelled into a mature scar. On the basis of our findings in this study, we propose a revised model (Fig. 6) in which, in deep injuries, fascia fibroblasts pilot their local composite matrix into wounds that, in coordination with the coagulation cascade, form the provisional matrix. Thus, instead of de novo matrix deposition by dermal fibroblasts, a 'scar primordium' is steered by the fascia fibroblasts. Thus, fascia serves as an external repository, or *externum repono*, of scar-forming provisional matrix, which represents an efficient mechanism to quickly seal large open wounds. Previous studies have shown that the matrix undergoes movement during early development and organ morphogenesis^{19–22}. To our knowledge, the extent and magnitude of matrix movements that we document here have not been observed during injury or regenerative settings. Cultured dermal fibroblasts have been shown to pull and reorient individual collagen or fibronectin fibres locally in cultured plates and in 3D in vitro assays^{23,24}. However, our findings reveal highly dynamic and large-scale movements of composite tissue matrix during injury that are mediated exclusively by specialized fibroblasts of the fascia.

Our findings on the contribution of fascia to large scars and its blockage leading to chronic open wounds indicates that the spectrum of poor

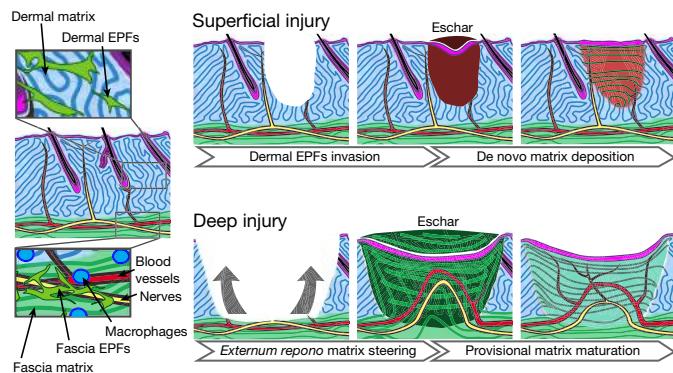


Fig. 6 | Revised wound healing model. Superficial injuries heal by the classical fibroblast migration and de novo matrix deposition process. In response to a deep injury, fascia fibroblasts steer their surrounding tissue into wounds. Fascia-derived macrophages, endothelial and peripheral nerves rapidly clog the open wound. In coordination with the platelet response, the fascia matrix serves as a provisional matrix that undergoes remodelling until it forms a mature scar.

and excessive scarring in the skin, such as in diabetic and ulcerative wounds, as well as in hypertrophic and particularly keloid scars, might all be attributed to fascia. Indeed, the subcutaneous fascia varies widely according to species, sex, age and anatomic skin location²⁵. In some mammals, the superficial fascia is loose, whereas in scar-prone species such as human, dog and horse, the superficial fascia is thicker. Human fascia further varies in thickness in different regions of the body²⁶. For example, the lower chest, back, thigh and arm have much thicker and multi-layered membranous sheets, and it is these anatomic sites that are prone to form hypertrophic and keloid scars²⁷. Understanding the topographic anatomy of the fascia layer may help explain scar phenotypes and severities, including the occurrences of hypertrophic and keloid scars.

Online content

Any methods, additional references, Nature Research reporting summaries, source data, extended data, supplementary information, acknowledgements, peer review information; details of author contributions and competing interests; and statements of data and code availability are available at <https://doi.org/10.1038/s41586-019-1794-y>.

1. Marshall, C. D. et al. Cutaneous scarring: basic science, current treatments, and future directions. *Adv. Wound Care* **7**, 29–45 (2018).

2. Finnerty, C. C. et al. Hypertrophic scarring: the greatest unmet challenge after burn injury. *Lancet* **388**, 1427–1436 (2016).

3. Morton, L. M. & Phillips, T. J. Wound healing and treating wounds: differential diagnosis and evaluation of chronic wounds. *J. Am. Acad. Dermatol.* **74**, 589–605, quiz 605–606 (2016).

4. Do, N. N. & Eming, S. A. Skin fibrosis: models and mechanisms. *Curr. Res. Transl. Med.* **64**, 185–193 (2016).

5. Sen, C. K. et al. Human skin wounds: a major and snowballing threat to public health and the economy. *Wound Repair Regen.* **17**, 763–771 (2009).

6. Hinz, B. Myofibroblasts. *Exp. Eye Res.* **142**, 56–70 (2016).

7. Driskell, R. R. et al. Distinct fibroblast lineages determine dermal architecture in skin development and repair. *Nature* **504**, 277–281 (2013).

8. Greenhalgh, S. N., Conroy, K. P. & Henderson, N. C. Healing scars: targeting pericytes to treat fibrosis. *QJM* **108**, 3–7 (2015).

9. Plikus, M. V. et al. Regeneration of fat cells from myofibroblasts during wound healing. *Science* **355**, 748–752 (2017).

10. Shook, B. A. et al. Myofibroblast proliferation and heterogeneity are supported by macrophages during skin repair. *Science* **362**, eaar2971 (2018).

11. Mori, L., Bellini, A., Stacey, M. A., Schmidt, M. & Mattoli, S. Fibrocytes contribute to the myofibroblast population in wounded skin and originate from the bone marrow. *Exp. Cell Res.* **304**, 81–90 (2005).

12. Rinkevich, Y. et al. Identification and isolation of a dermal lineage with intrinsic fibrogenic potential. *Science* **348**, aaa2151 (2015).

13. Jiang, D. et al. Two succeeding fibroblastic lineages drive dermal development and the transition from regeneration to scarring. *Nat. Cell Biol.* **20**, 422–431 (2018).

14. Adstrum, S., Hedley, G., Schleip, R., Stecco, C. & Yucesoy, C. A. Defining the fascial system. *J. Bodyw. Mov. Ther.* **21**, 173–177 (2017).

15. Stecco, C. & Schleip, R. A fascia and the fascial system. *J. Bodyw. Mov. Ther.* **20**, 139–140 (2016).

16. Dunkin, C. S. et al. Scarring occurs at a critical depth of skin injury: precise measurement in a graduated dermal scratch in human volunteers. *Plast. Reconstr. Surg.* **119**, 1722–1734 (2007).

17. Koehler, R. H. et al. Minimal adhesions to ePTFE mesh after laparoscopic ventral incisional hernia repair: reoperative findings in 65 cases. *JSLs* **7**, 335–340 (2003).

18. Rippa, A. L., Kalabusheva, E. P., & Vorotelyak, E., A. Regeneration of dermis: scarring and cells involved. *Cells* **8**, 607 (2019).

19. Zamir, E. A., Rongish, B. J. & Little, C. D. The ECM moves during primitive streak formation—computation of ECM versus cellular motion. *PLoS Biol.* **6**, e247 (2008).

20. Szabó, A., Rupp, P. A., Rongish, B. J., Little, C. D. & Czirók, A. Extracellular matrix fluctuations during early embryogenesis. *Phys. Biol.* **8**, 045006 (2011).

21. Aleksandrova, A. et al. Convective tissue movements play a major role in avian endocardial morphogenesis. *Dev. Biol.* **363**, 348–361 (2012).

22. Loganathan, R. et al. Extracellular matrix motion and early morphogenesis. *Development* **143**, 2056–2065 (2016).

23. Miron-Mendoza, M., Koppaka, V., Zhou, C. & Petroll, W. M. Techniques for assessing 3-D cell-matrix mechanical interactions in vitro and in vivo. *Exp. Cell Res.* **319**, 2470–2480 (2013).

24. Sakar, M. S. et al. Cellular forces and matrix assembly coordinate fibrous tissue repair. *Nat. Commun.* **7**, 11036 (2016).

25. Abu-Hijleh, M. F., Roshier, A. L., Al-Shboul, Q., Dharap, A. S. & Harris, P. F. The membranous layer of superficial fascia: evidence for its widespread distribution in the body. *Surg. Radiol. Anat.* **28**, 606–619 (2006).

26. Avelar, J. Regional distribution and behavior of the subcutaneous tissue concerning selection and indication for liposuction. *Aesthetic Plast. Surg.* **13**, 155–165 (1989).

27. Lockwood, T. E. Superficial fascial system (SFS) of the trunk and extremities: a new concept. *Plast. Reconstr. Surg.* **87**, 1009–1018 (1991).

Publisher's note Springer Nature remains neutral with regard to jurisdictional claims in published maps and institutional affiliations.

© The Author(s), under exclusive licence to Springer Nature Limited 2019

Methods

Mice and genotyping

All mouse strains (C57BL/6J, *En1^{cre}*, *R26^{VT2/Gk3}*, *R26^{mTmG}*, *R26^{idTR}*, *Rag2^{-/-}* and Fox Chase SCID) were obtained from either Jackson laboratories, Charles River or generated at the Stanford University Research Animal Facility as described previously¹². Animals were housed at the Helmholtz Center Animal Facility. Cages were maintained at constant temperature and humidity with a 12-h light cycle. Animals were supplied with food and water ad libitum. All animal experiments were reviewed and approved by the Government of Upper Bavaria and registered under the projects 55.2-1-54-2532-16-61 and 55.2-2532-02-19-23 and conducted under strict governmental and international guidelines. This study is compliant with all relevant ethical regulations regarding animal research. Unless specified, 8-to-10-week-old adult mice were used for the animal experiments. Both male and female mice were used. Cre-positive (Cre⁺) animals from double-transgenic reporter mice were identified by detection of relevant fluorescence in the dorsal dermis. Genotyping was performed to distinguish mouse lines containing a 200-base pair (bp) *cre* fragment (*cre^{+/+}*) from the wild-type (*cre^{-/-}*). Genomic DNA from the ear-clips was extracted using QuickExtract DNA extraction solution (Epicentre) following the manufacturer's guidelines. DNA extract (1 µl) was added to each 24 µl PCR. The reaction mixture was set up using Taq PCR core kit (Qiagen) containing 1× coral buffer, 10mM dNTPs, 0.625 units Taq polymerase, 0.5 µM forward primer 'Cre_genotype_4F' 5'-ATTGCTGTCACCTGGTCGTGGC-3' (Sigma) and 0.5 µM reverse primer 'Cre_genotype_4R' 5'-GGAAAATGCTTCTGTCCGTTTGC-3' (Sigma). PCRs were performed with initial denaturation for 10 min at 94 °C, amplification for 30 cycles (denaturation for 30 s at 94 °C, hybridization for 30 s at 56 °C, and elongation for 30 s at 72 °C) and final elongation for 8 min at 72 °C, and then cooled to 4 °C. In every experiment, negative controls (non-template and extraction) and positive controls were included. The reactions were carried out in an Eppendorf master cycler. Reactions were analysed by gel electrophoresis.

Human skin samples

Fresh human skin and scar biopsies, from various anatomic locations, were collected from donors between 18–65 years of age, through the Section of Plastic and Aesthetic Surgery, Red Cross Hospital Munich (reference number 2018-157), and by the Department of Dermatology and Allergology, Klinikum rechts der Isar Technical University Munich (reference number 85/18S). Informed consent was obtained from all subjects before skin biopsies. Upon collection, these samples were directly processed for tissue culture or fixed with PFA and then processed for cryosection or paraffin section followed by histological or immunofluorescent analyses.

Fascia in vitro culture

Two in vitro systems were used. To visualize the changes in matrix architecture in real time, 2-mm-diameter biopsies were excised from PO C57BL/6J neonates and processed for live imaging (SCAD assay, Patent Application no. PLA17A13). To determine the effectiveness of the DT treatment, muscle and fascia were manually separated from the rest of the skin in the chimeric grafts experiments and incubated with DT at different concentrations for 1 h at ambient temperature. Next, samples were washed with PBS and incubated in DMEM/F12 (Thermo Fisher) supplemented with 10% serum (Thermo Fisher), 1% penicillin–streptavidin (Thermo Fisher), 1% GlutaMAX (Thermo Fisher) and 1% non-essential amino acids solution (Thermo Fisher) in a 37 °C, 5% CO₂ incubator. Medium was routinely exchanged every other day. Samples were fixed at day 6 of culture with 2% paraformaldehyde and processed for histology.

Histology

Tissue samples were fixed overnight with 2% paraformaldehyde in PBS at 4 °C. Samples were rinsed three times with PBS, embedded in optimal

cutting temperature (OCT, Sakura Finetek) and flash-frozen on dry ice. Six-micrometre sections were made in a Cryostar NX70 cryostat (Thermo fisher). Masson's trichrome staining was performed with a Sigma-Aldrich trichrome stain kit, according to the manufacturer's guidelines. For immunolabelling, sections were air-dried for 5 min and fixed with –20 °C-chilled acetone for 20 min. Sections were rinsed three times with PBS and blocked for 1 h at room temperature with 10% serum in PBS. Then, the sections were incubated with primary antibody in blocking solution for 3 h at ambient temperature. Sections were then rinsed three times with PBS and incubated with secondary antibody in blocking solution for 60 min at ambient temperature. Finally, sections were rinsed three times in PBS and mounted with fluorescent mounting media with 4,6-diamidino-2-phenylindole (DAPI). Primary antibodies used: goat-anti-ACTA2(αSMA) (1:50, Abcam), rabbit-anti-TUBB3 (1:100, Abcam), rat-anti-THY1(CD90) (1:100, Abcam), rat-anti-CD24 (1:50, BD biosciences), rabbit-anti-DPP4(CD26) (1:150, Abcam), rabbit-anti-PECAM1 (1:10, Abcam), rat-anti-CD34 (1:100, Abcam), rabbit-anti-collagen I (1:150, Rockland), rabbit-anti-collagen III (1:150, Abcam), rabbit-anti-collagen VI (1:150, Abcam), rabbit-anti-DLK1 (1:200, Abcam), rat-anti-ERTR7 (1:200, Abcam), rat-anti-F4/80 (1:400, Abcam), rabbit-anti-LYVE1 (1:100, Abcam), rat-anti-MOMA2 (1:100, Abcam), goat-anti-PDGFRα (1:50, R & D systems), rat-anti-LY6A(Sca1) (1:150, Biologend), rat-anti-CD44 (1:100, Abcam), rabbit-anti-NOV/CCN3 (1:20, Elabscience), sheep-anti-FAP (1:100, R&D systems), rat-anti-IL12 (1:50, Biologend), rat-anti-IL4 (1:50, Biologend), rat-anti-CD19 (1:20, BD biosciences), hamster-anti-CD3e (1:100, Biologend), rat-anti-NCR1 (1:20, Biologend) and rat-anti-LY6G (1:100, Abcam). PacificBlue-, Alexa Fluor 488-, Alexa Fluor 568- or Alexa Fluor 647-conjugated antibodies (1:500, Life technologies) against suitable species were used as secondary antibodies.

Microscopy

Histological sections were imaged using a ZEISS AxioImager. Z2m (Carl Zeiss). For whole-mount 3D imaging of wounds, fixed samples were embedded in 35-mm glass bottom dishes (Ibidi) with low-melting point agarose (Biozym) and left to solidify for 30 min. Imaging was performed using a Leica SP8 multi photon microscope (Leica, Germany). For live imaging of fascia cultures, samples were embedded as just above. Attention was paid to mount the samples with the fascia facing up towards the objective. Imaging medium (DMEM/F-12; SiR-DNA 1:1,000) was then added. Time-lapse imaging was performed over 20 h under the multi-photon microscope. A modified incubation system, with heating and gas control (ibidi, catalogue nos. 10915 and 11922), was used to guarantee physiologic and stable conditions during imaging. Temperature control was set to 35 °C with 5% CO₂-supplemented air. Second harmonic generation signal and green auto-fluorescence as a reference were recorded every hour. 3D and 4D data was processed with Imaris 9.1.0 (Bitplane) and ImageJ (1.52i). Contrast and brightness were adjusted for better visibility.

Image analysis

Histological images were analysed using ImageJ. For quantification of labelled cells in our fate mapping experiments, we manually defined the wound, surrounding dermis, and adjacent fascia areas. We defined the wound as the area flanked by the near hair follicles on both sides, extending from the base of the epidermis down to the level of the hair follicles bulges. Surrounding dermis area was defined as the 200 µm immediately adjacent to the wound on both sides. Fascia area was defined as the tissue immediately below the wound. The number of labelled cells in each area was determined by quantifying the particles that were double-positive for DAPI and for the desired label (for example, DiI or GFP) channels. The coverage of the labelled matrix in the wound area was determined by quantifying the area that was double-positive for the labelled matrix and the collagen I-, III- and VI-staining signal. Cell density of *En1^{cre}*, *R26^{idTR}* cultures treated with DT was

Article

quantified by dividing the total cells (DAPI) by the matrix area (collagen I, III and VI), Collagens density was calculated as the collagens area coverage of the entire section area. Matrix movements in live-imaged cultures were determined by tracking the length of the two furthest points along the sample in both the SHG and auto-fluorescence channels. Length measurements were normalized to the original length at time 0. Wound size was normalized for each time point using the original area at day 0. Scar length was quantified from randomly selected sections taken from the middle of the scar using the two flanking hair follicles as a reference. RFI was calculated by measuring the mean grey value and normalize to the dermis images. Fractal analysis was performed using the ImageJ plug-in 'FracLac'29 (FracLac2015Sep090313a9390) using the same settings and preprocessing as previously described¹³.

Dil labelling of fascia in animals

Two 5-mm-diameter full-thickness excisional wounds were created on the back of 8- to 10-week-old C57BL6/J mice with a biopsy punch. Lipophilic Vybrant Dil dye (Life technologies, V22885) (10–20 μ l) was injected into the exposed fascia directly above the dorsal muscles. Wounded tissue was harvested 14 dpw and processed for histology and imaging by fluorescence microscopy.

Chimeric skin transplantation

Full-thickness 6-mm-diameter biopsies were collected from the back-skin of either $R26^{mTmG}$, $R26^{VT2/GK3}$, $En1^{cre};R26^{mTmG}$, $En1^{cre};R26^{IDTR}$ or C57BL6/J adult mice. Using the PC muscle layer as an anatomical reference, the fascia together with the muscle layer were carefully separated from the dermis and epidermis using Dumont no. 5 forceps (Fine Science Tools) and a 26G needle under the fluorescent stereomicroscope (M205 FA, Leica). EPFs from fascia + muscle samples of $En1^{cre};R26^{IDTR}$ mice were ablated by incubation with 20 μ g ml⁻¹ of diphtheria toxin (Sigma-Aldrich, D0564) or only DMEM/F12 as vehicle for 1 h at ambient temperature followed by 3 washing steps with PBS. At this point, the matrix samples were labelled by incubation with 100 μ M Alexa Fluor NHS Ester (Life Technologies, A20006) or Pacific Blue succinimidyl ester (Thermo Fisher, P10163) in PBS for 1 h at ambient temperature followed by 3 washing steps with PBS. Chimeras were made by placing the epidermis + dermis portion of a mouse strain on top of the muscle + fascia of another strain and left to rest for 20 min at 4 °C inside a 35-mm culture dish with 2 ml of DMEM/F12. Special attention was paid on preserving the original order of the different layers (top to bottom: epidermis > dermis > muscle > fascia). Then, a 2 mm 'deep' full thickness was excised from the chimeric graft using a biopsy punch in the middle of the biopsy. To create 'superficial' wounds, the 2-mm excision was done only in the epidermis + dermis half before reconstitution with the bottom part. 'Wounded' chimeric grafts were then transplanted into freshly-made 4-mm-diameter full-thickness excisional wounds in the back of either $RAG2^{-/-}$ or Fox Chase SCID immunodeficient 8- to 10-week-old mice. Precautions were taken to clean out the host blood from the fresh wound before the transplant and to leave the graft to dry for at least 20 min before ending the anaesthesia, to increase the transplantation success. To prevent mice from removing the graft, a transparent dressing (Tegaderm, 3M) was placed on top of the grafts.

In situ matrix tracing and EdU pulses

Eight- to ten-week-old C57BL6/J mice received subcutaneous 20- μ l injections of 10 mg ml⁻¹ FITC NHS ester in physiological saline with 0.1 M sodium bicarbonate pH9 (46409, Life technologies) four and two days before wounding. At 2, 6 or 13 dpw, mice received 200 μ l intraperitoneal injections of 1 mg ml⁻¹ EdU in PBS. Samples were collected 24 h after the EdU pulse and processed for cryosection and imaging by fluorescence microscopy.

Flow cytometry

Fascia and dermis were physically separated from the back-skin of C57BL6/J or $En1^{cre};R26^{mTmG}$ mice under the fluorescence

stereomicroscope as before. Harvested tissue was minced with surgical scissors and digested with an enzymatic cocktail containing 1 mg ml⁻¹ collagenase IV, 0.5 mg ml⁻¹ hyaluronidase, and 25 U ml⁻¹ DNase I (Sigma-Aldrich) at 37 °C for 30 min. The resulted single cell suspension was filtered and incubated with conjugated/unconjugated primary antibodies (dilution 1:200) at 4 °C for 30 min, followed by an incubation with a suitable secondary antibody when needed at 4 °C for 30 min. Cells were washed and stained with Sytox blue dye (dilution 1:1,000, Life technologies, S34857) for dead cell exclusion. Cells were subjected to flow cytometric analysis using a FACS Aria III (BD Bioscience). Fibroblasts were gated as the lineage negative (Lin⁻) fraction not expressing the PTPRC, PECAM1, LY76, LYVE-1, or EPCAM markers. Primary antibodies used: anti-DLK1 (Abcam), anti-CD9 (Santa Cruz), anti-NGFR (Miltenyi), anti-F4/80 (Abcam), AlexaFluor790-anti-NG2 (Santa Cruz), FITC-anti-DPP4 (eBioscience), PerCP-eFluor710-anti-ITGB1 (eBioscience), anti-CD34 (Abcam), PerCP-Cy5.5-anti-CD24 (eBioscience), APC-Fire750-anti-CD34 (Biolegend), APC-anti-ITGA7 (R&D systems), PerCP-Cy5.5-anti-LY6A (eBioscience), PE-Vio770-anti-PDGFR α (Miltenyi), PerCP-Vio700-anti-CD146 (Miltenyi), APC-anti-PECAM1 (eBioscience), eFluor660-anti-LYVE1 (Thermo fisher), APC-LY76 (TER119), APC-anti-EPCAM (CD326) and APC-anti-PTPRC. Secondary antibodies used: Alexa Fluor 488 goat anti-rabbit (Life technologies) and AlexaFluor568 goat anti-rat (Life technologies).

Scanning electron microscopy

Skin biopsies of adult C57BL6/J mice were collected, and the fascia was manually separated as before. Samples were then fixed overnight with paraformaldehyde and glutaraldehyde, 3% each, in 0.1% sodium cacodylate buffer pH 7.4 (Electron Microscopy Sciences). Samples were dehydrated in gradual ethanol and dried by the critical-point method, using CO₂ as the transitional fluid (Polaron Critical Point Dryer CPC E3000; Quorum Technologies) and observed by scanning electron microscopy (JSM 6300F; JEOL).

ePTFE membrane implants

These membranes are routinely used in the clinic to circumvent post-operative adhesions after laparoscopic ventral incisional hernia repairs¹⁷. Two 6-mm-diameter full-thickness excisional wounds were created with a biopsy punch on the back of 8-week-old $En1^{cre};R26^{VT2/GK3}$ or C57BL6/J mice. Sterile 8-mm-diameter ePTFE impermeable membranes (Dualmesh, GORE) were implanted between the surrounding skin and the fascia underneath, to cover the open wound on the right side. For this, the surrounding skin was loosen using Dumont no. 5 forceps and spatula (10090-13, Fine Science Tools). The dual-surface membrane was implanted with the attaching face facing out, so to promote dermal cell attachment, while the smooth surface was in direct contact with the fascia. The left sham control wound underwent the same procedure without implanting any membrane. Each wound was photographed at indicated time points, and wound areas were measured using ImageJ. Wound sizes at any given time point after wounding were expressed as percentage of initial (day 0) wound area. At 7 or 63 dpw, samples were collected and processed for histology.

Released fascia injury in adult mice

Two 5-mm-diameter full-thickness excisional wounds were created with a biopsy punch on the back of 8-week old male C57BL6/J mice. The skin around the wound on the left side was separated from the underneath skeletal muscle using a sterilized gold-plated 3 \times 5 mm genepaddles (Harvard Apparatus, 45-0122) to release the fascia layer. The right wound served as a control. Each wound was digitally photographed at indicated time points, and wound areas were measured using Photoshop (Adobe Systems). Wound sizes at any given time point after wounding were expressed as percentage of initial (day 0) wound area. The harvested tissue at the indicated time points was processed for cryosection and Masson's trichrome staining for histology.

Viral particle production

AAV6 expressing GFP or Cre recombinase were produced by transfecting the AAVpro 293T Cell Line (Takara Bio, 632273) with pAAV-U6-sgRNA-CMV-GFP (Addgene, 8545142) or pAAV-CRE Recombinase vector (Takara Bio, 6654), pRC6 and pHelper plasmids procured from AAVpro Helper Free System (Takara Bio, 6651). Transfection was performed with PEI transfection reagent and viruses were harvested 72 h later and purified with an AAVpro purification kit (Takara Bio, 6666) and titre was calculated using real-time PCR.

Fascia cells ablation with AAV6-Cre viral particles and DT treatment in pups

Two 3-mm-diameter full-thickness excisional wounds were created with a biopsy punch on the back of postnatal day 11 (P11) *R26^{idTR}* mice. Twenty microlitres of Cre-expressing AAV6-Cre or control AAV6-eGFP at viral titre of $5 \times 10^{11} \text{ ml}^{-1}$ were injected subcutaneously at the area between the two wounds. DT solution at $1 \text{ ng } \mu\text{l}^{-1}$ in PBS was intraperitoneally injected to each mouse once per day for 7 days at the dosage of 5 ng g^{-1} . Tissue was collected seven days after wounding.

Statistics

Statistical analyses were performed using GraphPad Prism software (v.6.0, GraphPad). Statistical test and *P* values are specified in the figure legends and in the corresponding plots. For simplicity, *P* values below 0.0001 were stated as equal to 0.0001.

Reporting summary

Further information on research design is available in the Nature Research Reporting Summary linked to this paper.

Data availability

Source Data for Figs. 1–5 and Extended Data Figs. 1–10 are provided with the paper. Additional information is available from the corresponding author on reasonable request.

Acknowledgements We thank G. Mettenleiter for technical assistance with the SEM; S. Dietzel and the Core Facility Bioimaging at the Biomedical Centre of the Ludwig-Maximilians-Universität München for access and support with the multi-photon system. Y.R. was supported by the Human Frontier Science Program Career Development Award (CDA00017/2016), the German Research Foundation (RI 2787/1-1 AOBJ: 628819), the Fritz-Thyssen-Stiftung (2016-01277) and the European Research Council Consolidator Grant (ERC-CoG 819933). D.C.-G. was supported by the Consejo Nacional de Ciencia y Tecnología (CONACYT) and the Deutscher Akademischer Austauschdienst (DAAD).

Author contributions Y.R. outlined and supervised the research narrative and experimental design. D.C.-G. performed the cell and matrix tracing experiments, chimeric skin transplantations, ePTEF implantations and image analysis. D.J. performed the cell depletion with DT in pups, flow cytometry experiments and analysis, fascia release experiments and experiments with human skin samples. S.C. performed the live imaging and analysis. S.C. and P.R. performed 3D imaging and analysis. H.Y. performed histology and immunofluorescence staining of human samples. J.W. provided veterinary advice and prepared animal experiment protocols. S.K.G. made the viral particles and performed titre quantification. Q.Y. assisted in the flow cytometry experiments. U.M. and T.V. collected consent from patients and the primary human tissue samples, and assisted with translational and clinical advice. U.M. wrote, in part, the ethical application for collection and use of human samples. M.A. and A.W. performed the scanning electron microscopy images. Y.R., D.C.-G. and D.J. wrote the manuscript.

Competing interests The authors declare no competing interests.

Additional information

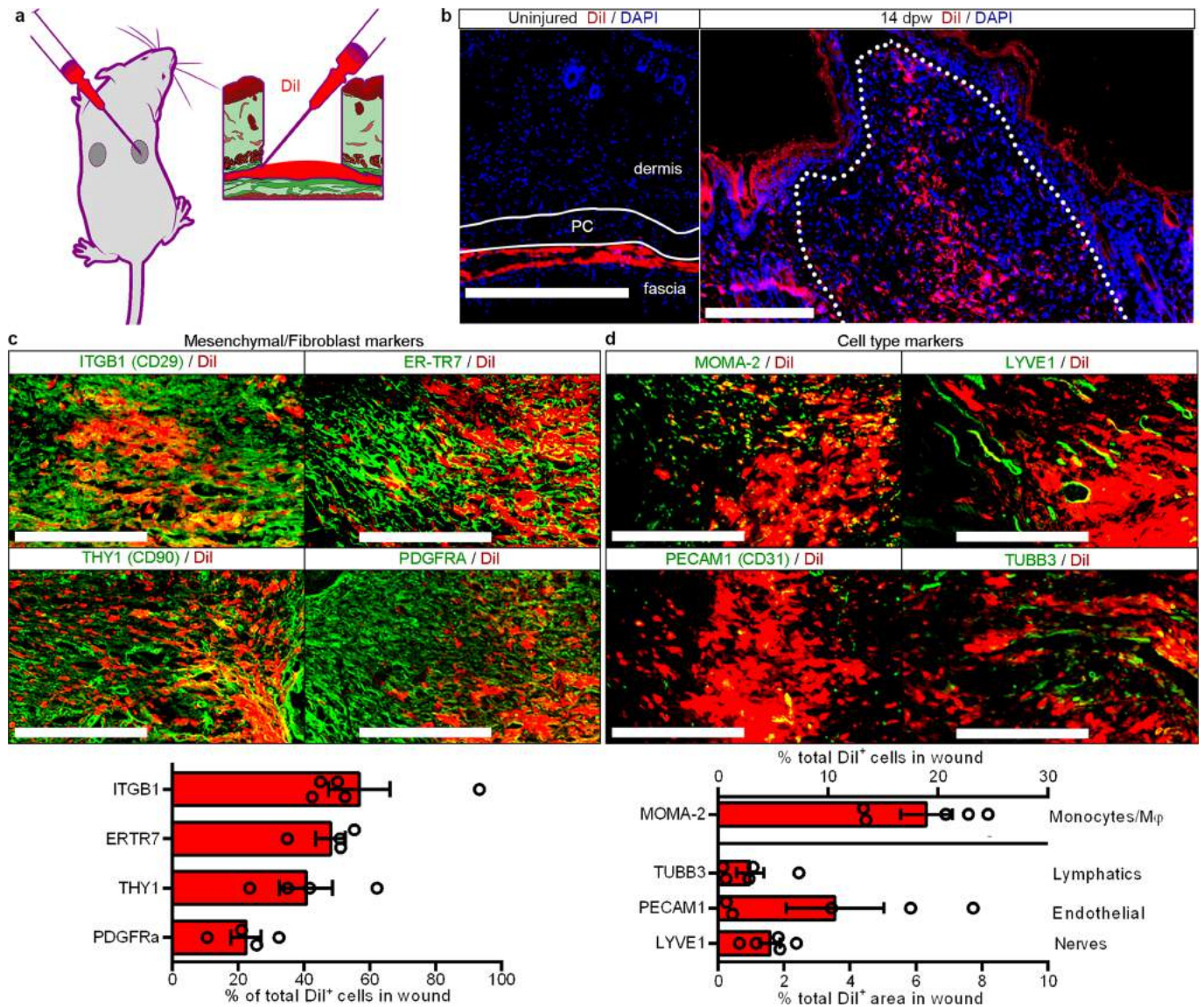
Supplementary information is available for this paper at <https://doi.org/10.1038/s41586-019-1794-y>.

Correspondence and requests for materials should be addressed to Y.R.

Peer review information *Nature* thanks Christopher Buckley and the other, anonymous, reviewer(s) for their contribution to the peer review of this work.

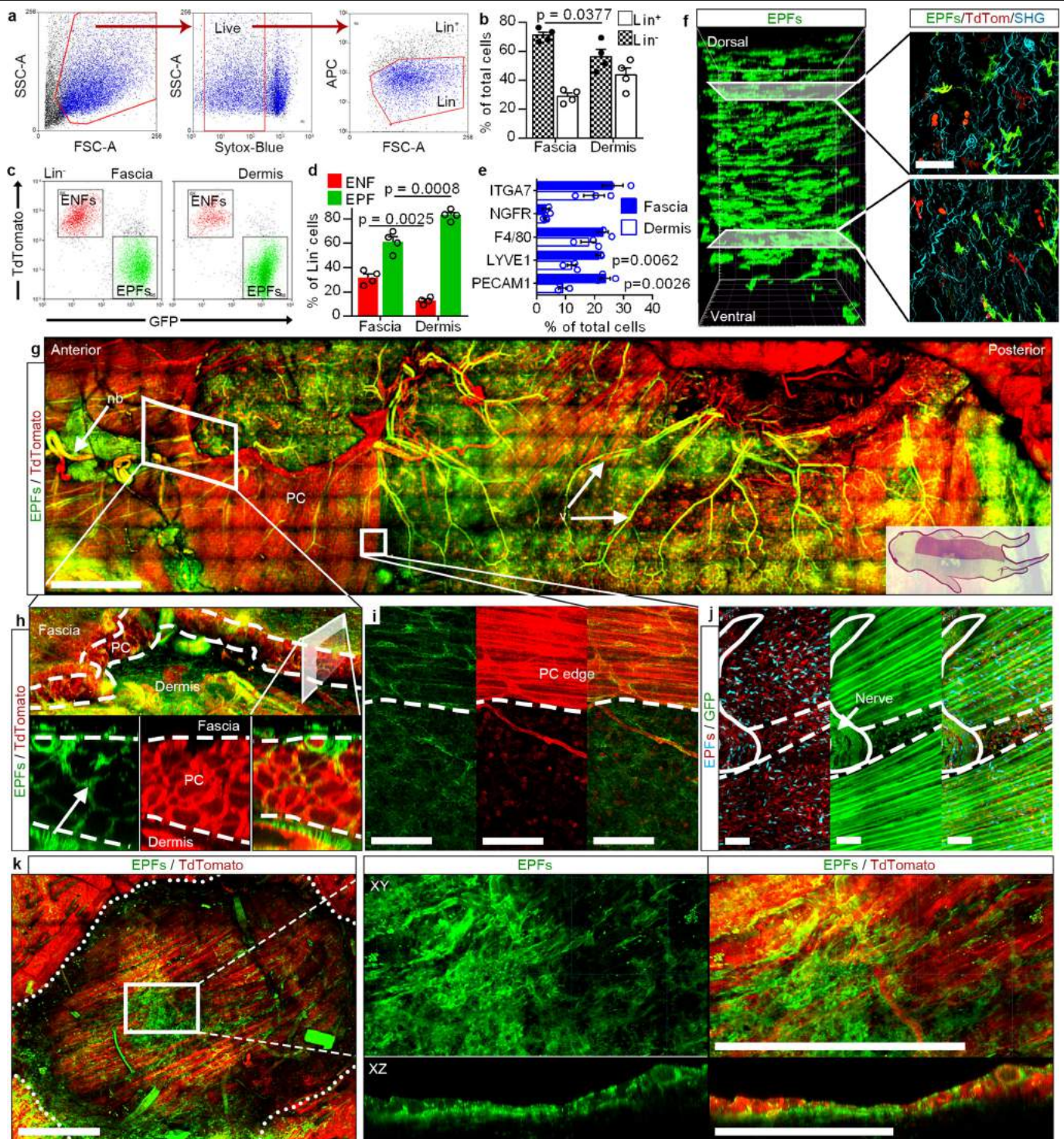
Reprints and permissions information is available at <http://www.nature.com/reprints>.

Article



Extended Data Fig. 1 | Fate mapping of fascia cells with Dil. **a**, Dil labelling of fascia cells. **b**, Histology showing Dil⁺ cells in uninjured controls (left) and at 14 dpw (right). Representative images of five biological replicates. **c**, Immunolabelling (top) and fractions (bottom) of Dil-positive cells expressing mesenchymal/fibroblast markers ITGB1, ER-TR7, THY1 and PDGFRA. Data are mean \pm s.e.m.; $n=4$ (5 in ITGB1) images analysed from 3

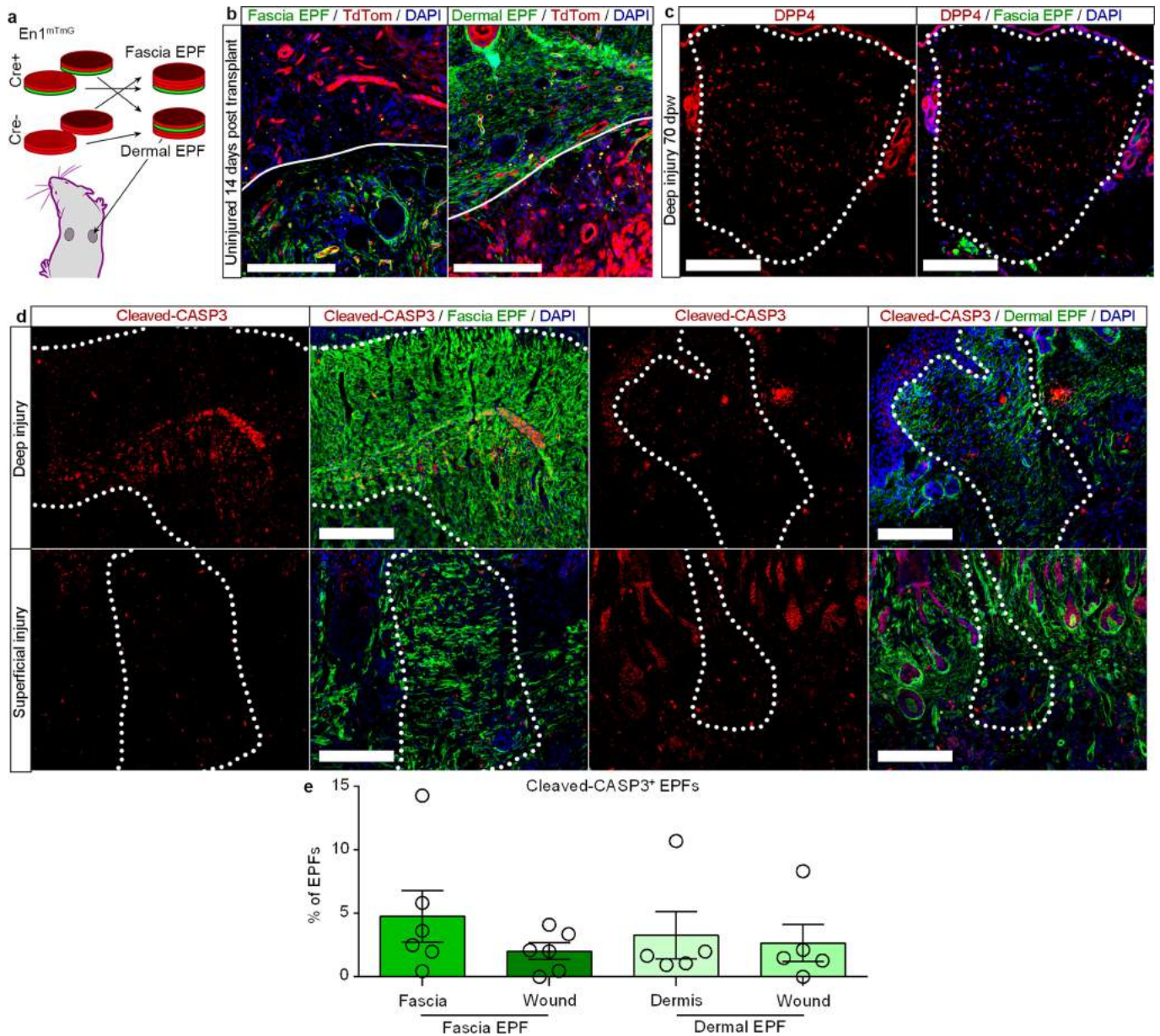
biological replicates. **d**, Immunolabelling (top) and fractions (bottom) of Dil-positive monocytes/macrophages (MOMA-2), lymphatic cells (LYVE1), endothelial cells (PECAM1) and nerve cells (TUBB3). Data are mean \pm s.e.m.; $n=5$ images analysed from 3 biological replicates. Lines delimit PC. The dotted line delimits the wound. Scale bars, 200 μ m.



Extended Data Fig. 2 | Fascia EPFs traverse PC. **a**, Gating strategy for fibroblasts analysis. **b**, Percentages of fibroblasts (Lin⁺) and lineage-positive cells in fascia and dermis. Data are mean \pm s.e.m.; $n = 4$ independent experiments. Unpaired two-tailed t -test, 95% CI. **c**, Scatter plots of EPFs (GFP⁺Lin⁻) and ENFs (TdTomato⁺Lin⁻) in fascia and dermis. Representative plots of three independent experiments. **d**, EPF and ENF fractions in fascia and dermis. Data are mean \pm s.e.m.; $n = 4$ independent experiments. Two-way ANOVA, multiple comparison Tukey's test, 95% CI. **e**, Endothelial cell (PECAM1⁺), lymphatic cell (LYVE1⁺), macrophages (F4/80⁺) and nerve cell (NGFR⁺) fractions in fascia and dermis. Data are mean \pm s.e.m.; $n = 3$ biological replicates. Two-way ANOVA, multiple comparison Tukey's test, 95% CI. **f-k**, Representative images

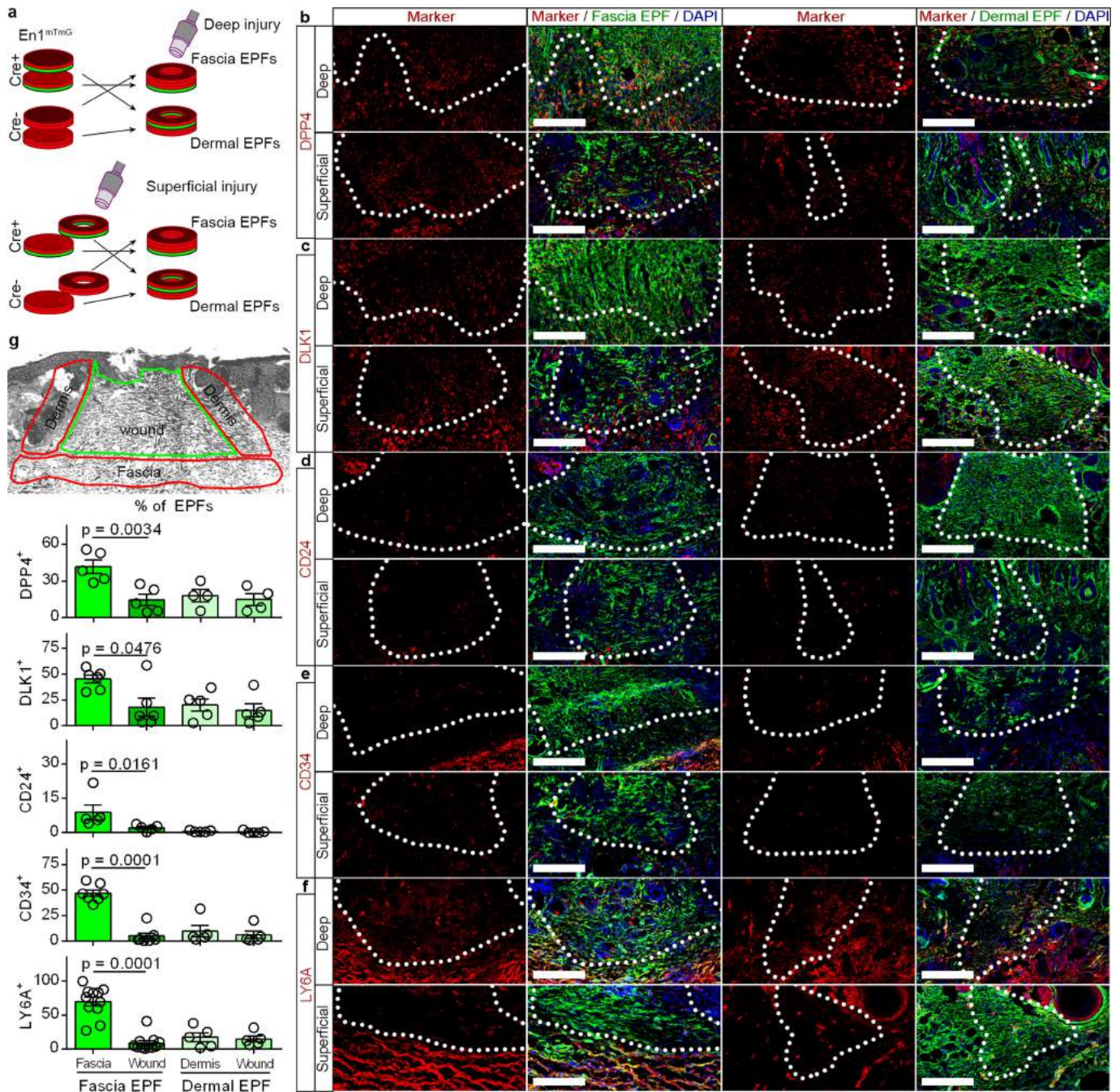
of 3D-rendered *En1^{cre};R26^{mTmG}* or *En1^{cre};R26^{VT2/Gk3}* back skin fascia from at least three biological replicates. **f**, Lateral view (left) and cross-sections (right) of adult fascia. **g**, Top view (ventral side up) of neonate back skin. **h**, Top side view (top) and lateral cross-section (bottom) at the forelimb junction showing EPF traversing the PC. **i**, Top view at a muscle breach showing EPFs in both locations. **j**, Top view at a muscle opening where nerves pass through and polyclones of EPFs reside (bottom) of an adult superficial wound (3 dpw). Broken lines delimit PC. Dotted lines delimit the epidermis. Scale bars, 1,500 μ m (**g**), 100 μ m (**f**, **i**, **j**) and 500 μ m (**k**); v, vessels; nb, nerve bundles.

Article



Extended Data Fig. 3 | Fascia EPFs maintain position in steady conditions and recede from wounds over time. **a**, Dermal versus fascia EPFs chimeras in uninjured conditions. **b**, Fascia (left) or dermal (right) EPFs-traced chimeras. Representative images of 3 biological replicates. **c**, Scars at 70 dpw from deep injuries of fascia EPF-traced chimeras immunolabelled for DPP4. Representative images of 3 biological replicates. **d**, Cleaved CASP3 expression

in wounds from fascia (left) or dermal (right) EPF-traced chimeras from deep (top) or superficial (bottom) injuries at 14 dpw. **e**, Fractions of fascia or dermal EPFs in the wound, dermis or fascia control regions positive for cleaved CASP3. Data are mean \pm s.e.m.; $n = 6$ and 5 (fascia and dermal EPF, respectively) images analysed from 5 biological replicates. Lines delimit the border between fascia and dermis. Dotted lines delimit the wound or scar. Scale bars, 200 μ m.



Extended Data Fig. 4 | Fascia EPFs express wound fibroblast markers.

a, Dermal versus fascia EPF-traced chimeras with two injury conditions.

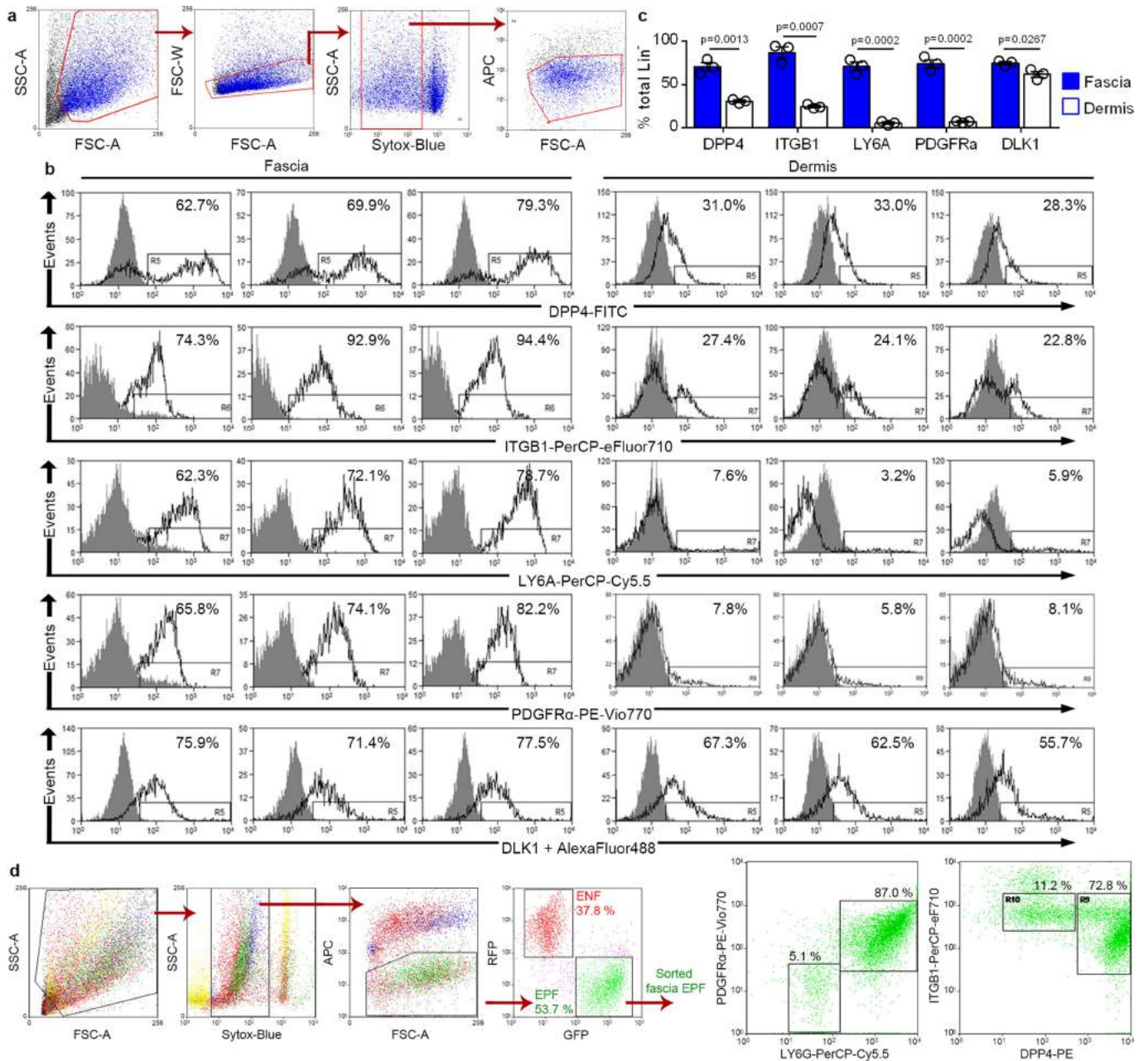
b-f, Representative immunolabelling for the fibroblast markers DPP4 (**b**), DLK1

(**c**), CD24 (**d**), CD34 (**e**) and LY6A (**f**) from 4 biological replicates. **g**, Areas

analysed (top) for marker-positive EPF quantification (bottom). Data are

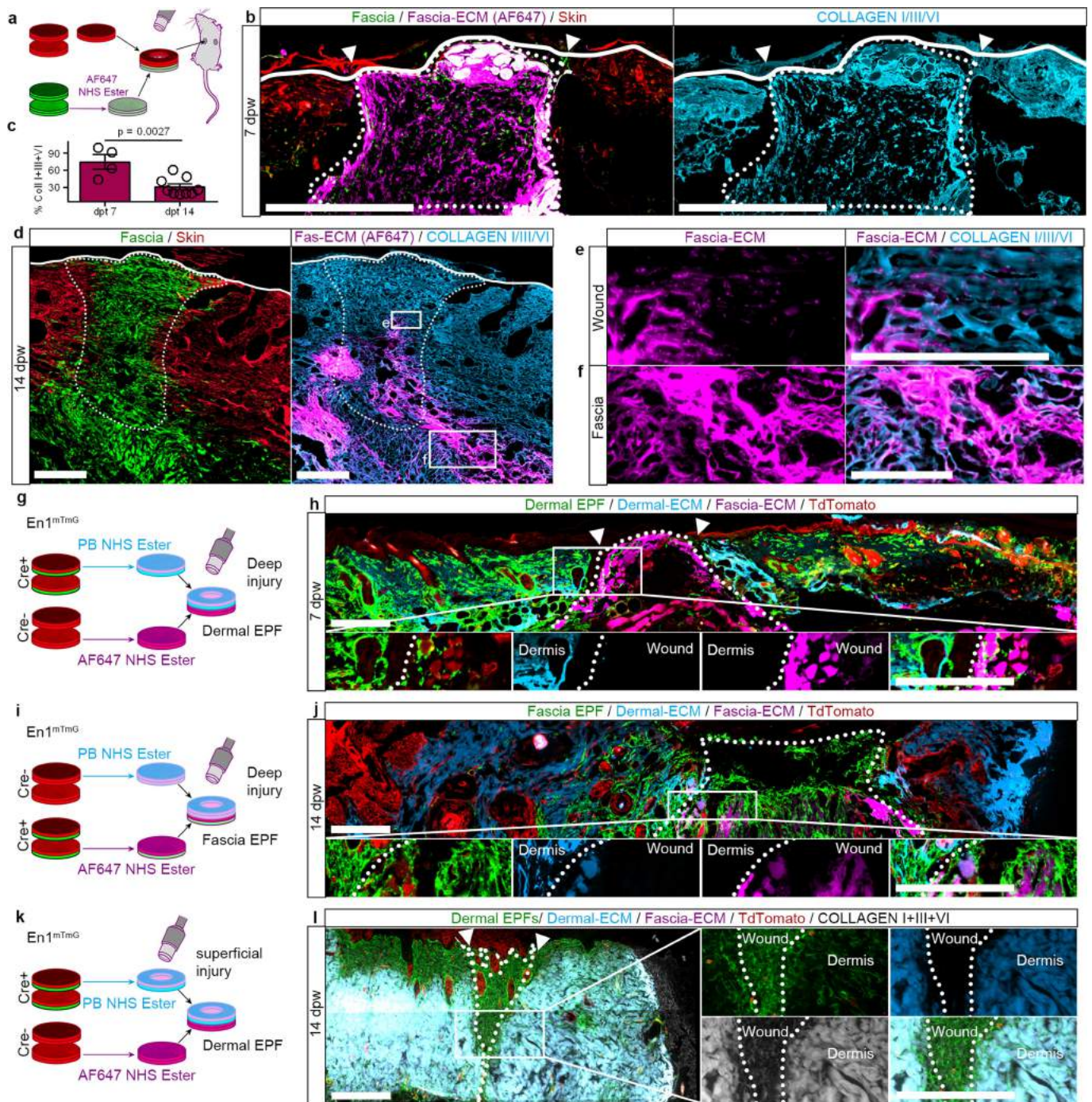
mean \pm s.e.m.; $n = 4$ (DPP4 in dermal EPFs), 5 (all markers in dermal EPFs with the

exception of DPP4 and all markers in fascia EPFs with the exception of DLK1, CD34 and LY6A), 6 (DLK1 in fascia EPFs), 7 (CD34 in fascia EPFs) or 11 (LY6A in fascia EPFs) images analysed from 4 biological replicates. One-way ANOVA, multiple comparison Tukey's test, 95% CI. Dotted lines delimit the wound bed. Scale bars, 200 μ m.



Extended Data Fig. 5 | Differential expression of classical markers on fascia and dermal fibroblasts. a. Gating strategy for fibroblast (Lin⁻) cytometry. **b.** Histogram plots of fibroblast-marker expression in fascia or dermis derived fibroblasts from three biological replicates. **c.** Fraction of marker-positive cells

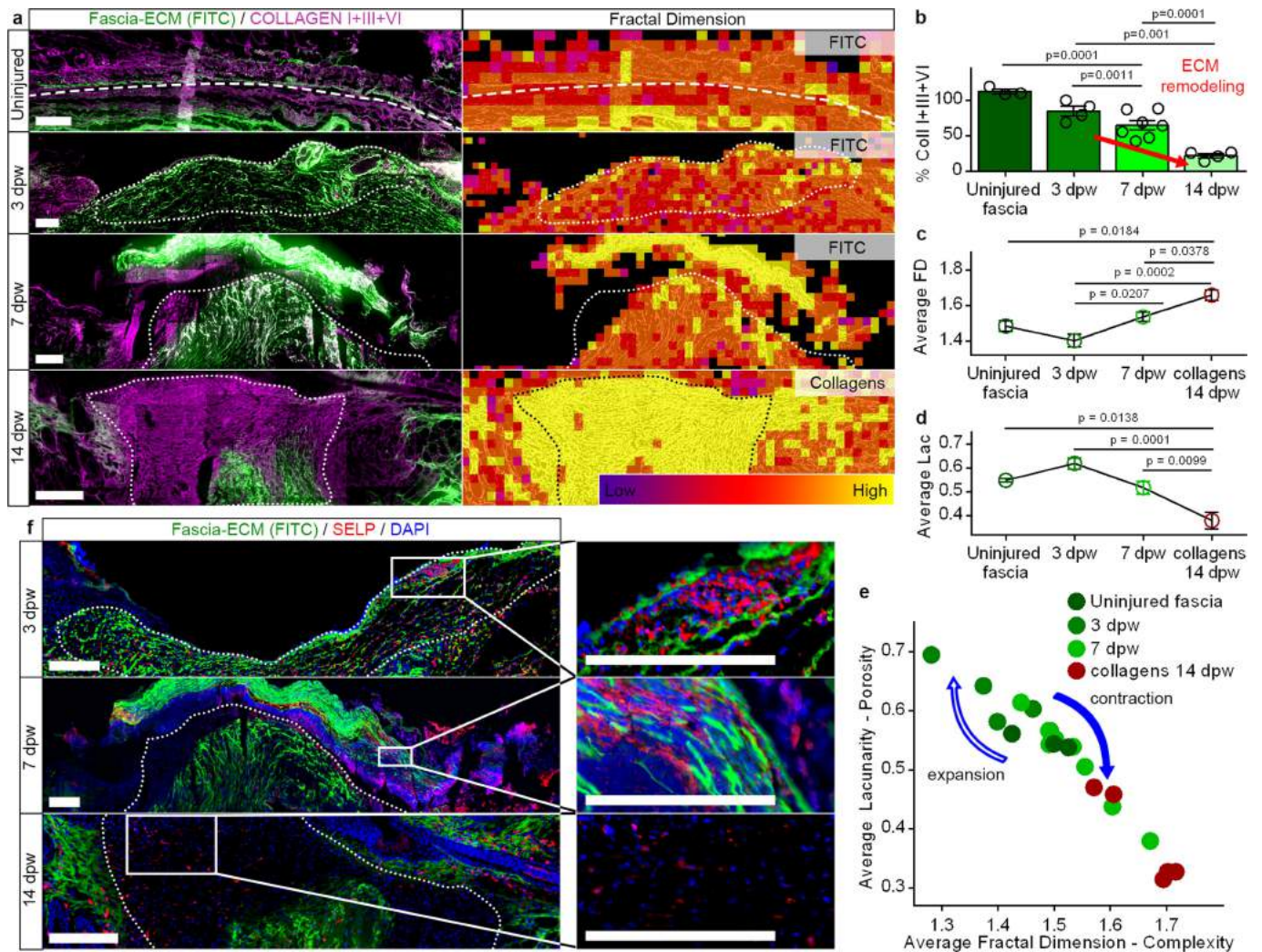
from total fibroblast population. Data are mean ± s.e.m.; n = 3 biological replicates. Unpaired two-tailed t-test, 95% CI. **d.** Gating strategy for fascia EPF (Lin⁻ GFP⁺) sorting and detection of LY6A, PDGFR1, DPP4 and ITGB1 expression. Representative plots of three biological replicates.



Extended Data Fig. 6 | Fascia but not dermal matrix steers into wounds.

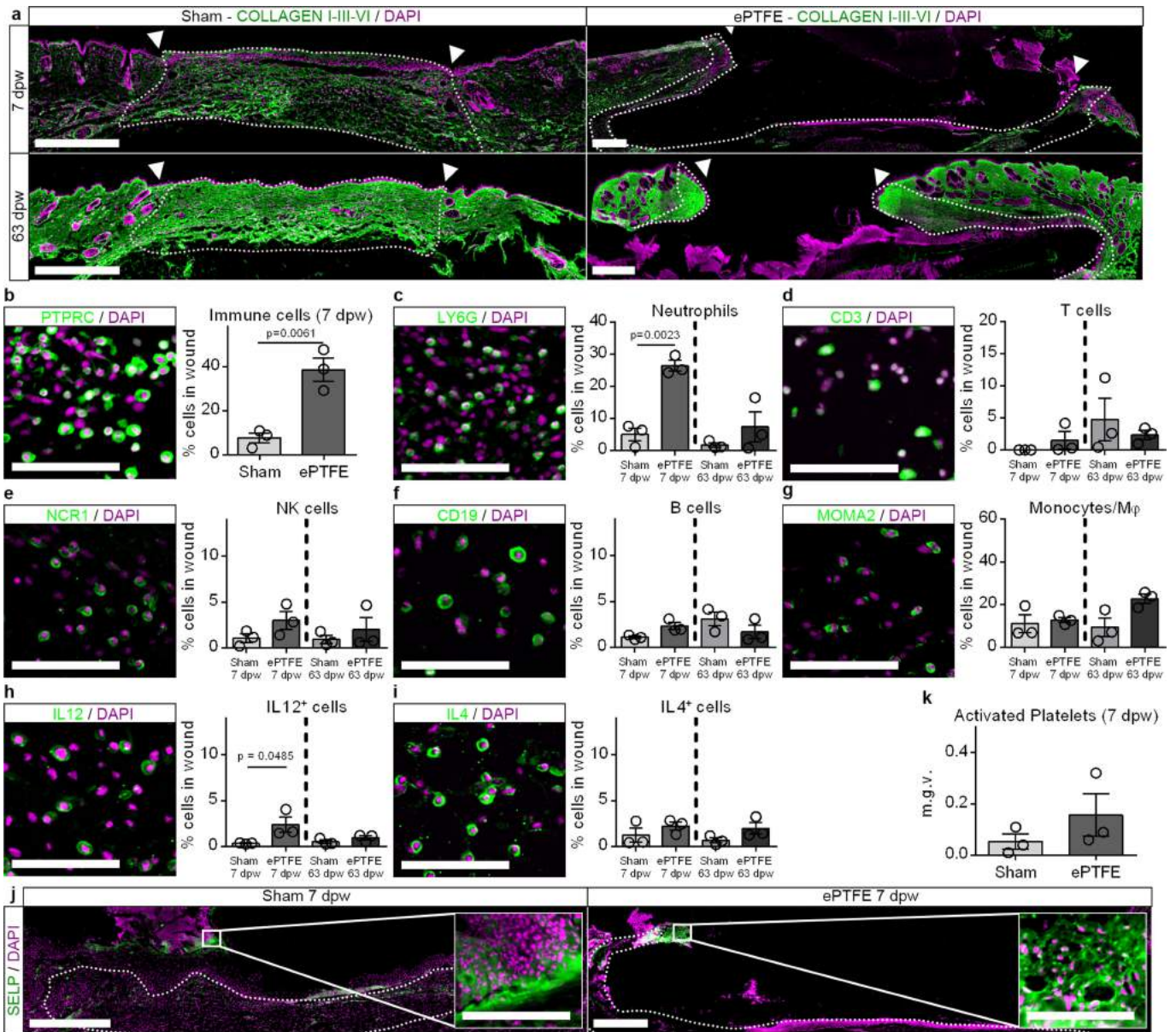
a, Matrix tracing in chimeric grafts. **b**, Grafts at 7 dpw immunolabelled for collagen I, III and VI. Representative image of three biological replicates. **c**, Label coverage fraction from total collagens in the wound at defined time points. Data are mean \pm s.e.m.; $n = 4$ (7 dpw) and 9 (14 dpw) sections analysed from 3 biological replicates. Unpaired two-tailed t -test, 95% CI. **d**, Wounds at 14 dpw immunolabelled for collagens. Representative images of three biological replicates. **e-f**, Higher magnification of the insets in **d.g**. **h**, Double matrix tracing in deep-injured dermal EPF-traced grafts at 7 dpw.

Representative image of three biological replicates. **i,j**, Double matrix tracing in deep-injured fascia EPF-traced grafts at 14 dpw. Representative image of three biological replicates. **k,l**, Double matrix labelling in superficial-injured dermal EPF-traced grafts at 14 dpw immunolabelled for collagens. Representative image of three biological replicates. Dotted lines delimit the wound. Arrowheads mark the original injury. Continuous lines delimit the epidermis dermis margin. Scale bars, 500 μ m (**b**), 100 μ m (**d-f**) and 200 μ m (**h,j,l**).



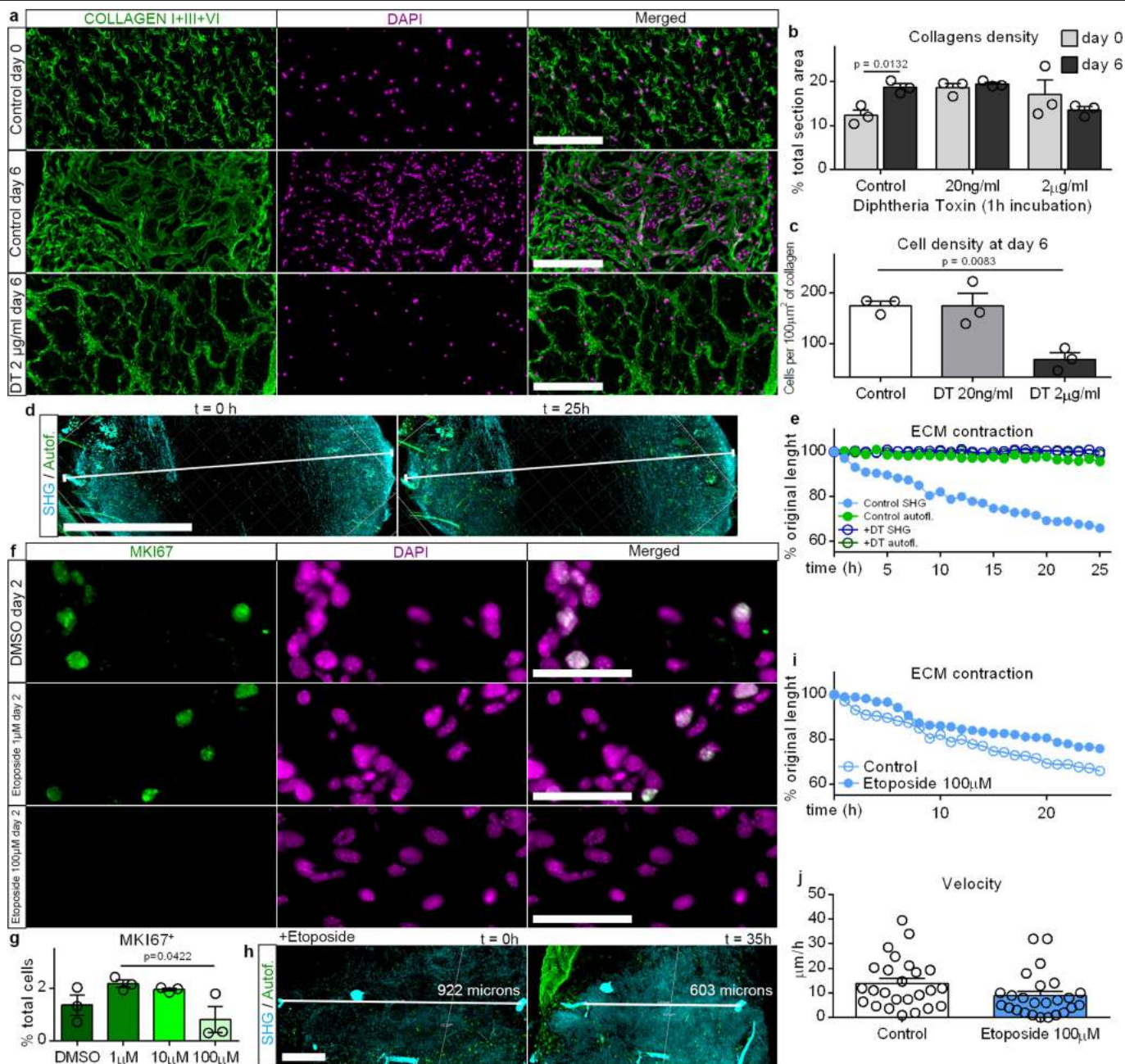
Extended Data Fig. 7 | Fascia matrix forms the eschar and is remodelled in the wound. a, Left, in situ matrix tracing and collagen I, III and VI immunolabelling at defined time points after wounding. Representative images of three biological replicates. Right, subsampled fractal dimension maps of the FITC signal of uninjured tissue and at 3 and 7 dpw, and the collagen signal at 14 dpw. **b**, Matrix label coverage from total collagen I, III and VI signal in the wound. Data are mean \pm s.e.m.; $n = 3$ (uninjured), 4 (3 dpw), 7 (7 dpw) and 4 (14 dpw) sections analysed from 3 biological replicates. One-way ANOVA,

Tukey's multiple comparisons. **c**, **d**, Average fractal dimension (**c**) and lacunarity (**d**) from subsampled maps. Data are mean \pm s.e.m.; $n = 5$ (uninjured), 5 (3 dpw), 8 (7 dpw) and 3 (14 dpw) images analysed from 3 biological replicates. One-way ANOVA, Tukey's test, 95% CI. **e**, Scatter plot of average fractal dimension and lacunarity values. **f**, In situ matrix tracing and SELP immunolabelling at defined time points after wounding. Representative images of three biological replicates. The broken line separates dermis from fascia. Dotted lines indicate the wound. Scale bars, 200 μ m.



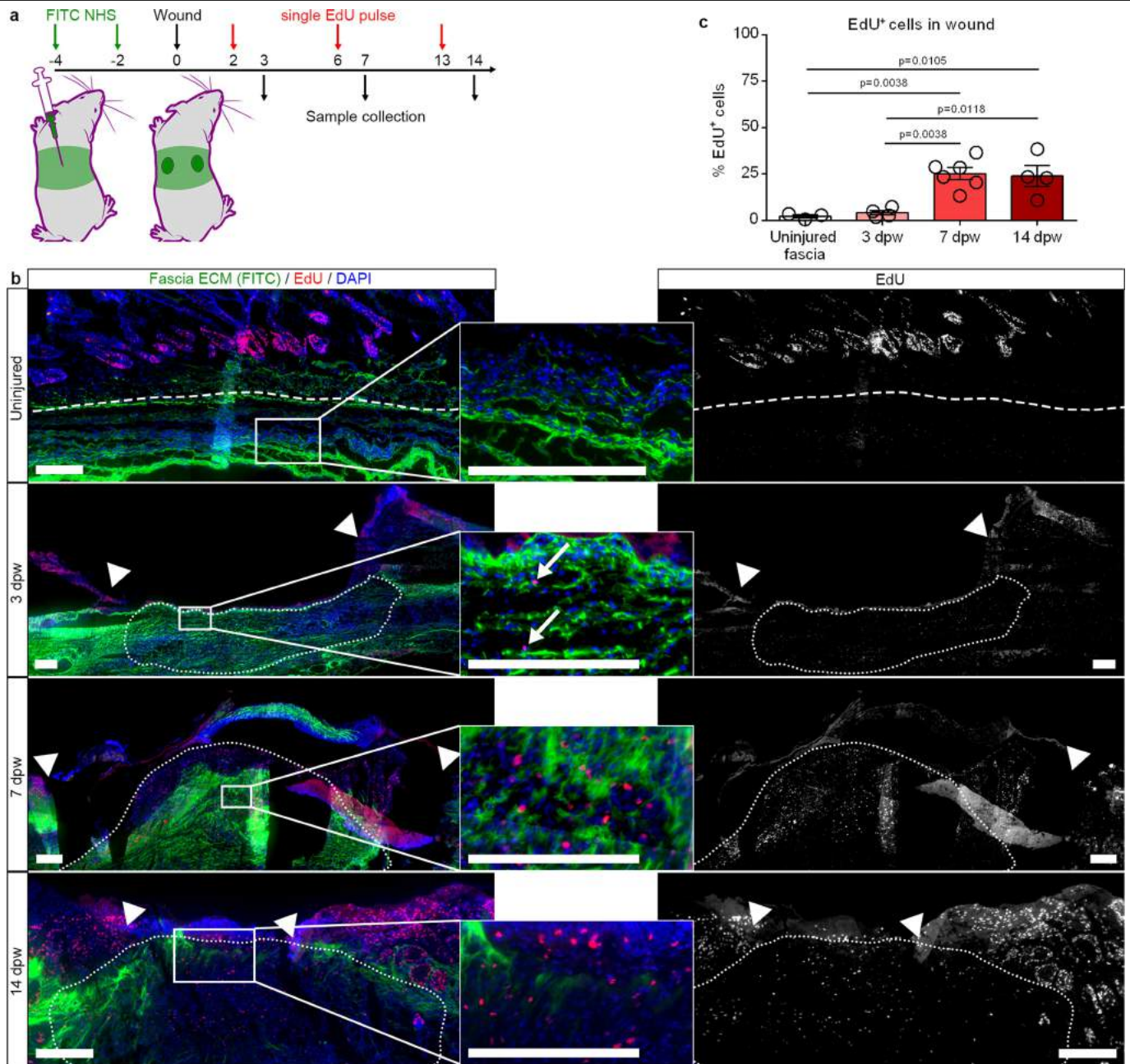
Extended Data Fig. 8 | Inflammation resolution and coagulation stay unaffected during fascia blocking. **a**, Sham (left) or ePTFE-implanted (right) wounds at 7 (top) or 63 dpw (bottom) immunolabelled for collagen I, III and VI. Representative images of three biological replicates. **b–i**, Immunolabellings (left) and fractions (right) of immune cells (PTPRC⁺; **b**), neutrophils (LY6G⁺; **c**), T cells (CD3⁺; **d**), NK cells (NCR1⁺; **e**), B cells (CD19⁺; **f**), macrophages and monocytes (MOMA2⁺; **g**) and cells expressing the pro- and anti-inflammatory cytokines (IL12⁺ (**h**) and IL4⁺ (**i**)). Mean with SEM, $n=3$ images analysed from 3

biological replicates. Unpaired two-tailed *t*-test, 95% CI (**b**). One-way ANOVA, Tukey's test, 95% CI (**c–i**). **j**, Activated platelets (SELP) in 7 dpw sham and ePTFE-implanted wounds. Representative images of 3 biological replicates. **k**, Mean grey value of SELP signal. Data are mean \pm s.e.m.; $n=3$ images analysed from 3 biological replicates. Two-tailed Student's *t*-test, 95% CI. Dotted lines delimit the wound area. Scale bars, 200 μ m (main images) and 100 μ m (magnified insets).



Extended Data Fig. 9 | EPFs steer matrix in vitro independently of proliferation. **a**, *En1^{Cre};R26^{DTR}* biopsies at day 0 and 6 after short treatment with DT or vehicle, immunolabelled for collagen I, III and VI. Representative images of three replicates. **b**, Collagens density. Data are mean ± s.e.m.; *n* = 3 images analysed from 3 biological replicates. Two-way ANOVA, multiple comparison Tukey's test, 95% CI. **c**, Cell density. Data are mean ± s.e.m.; *n* = 3 images analysed from 3 biological replicates. One-way ANOVA, multiple comparison Tukey's test, 95% CI. **d, e**, Time-lapse images (**d**) and contraction rate (**e**) of *En1^{Cre};R26^{DTR}* neonate fascia biopsy in culture treated with DT for 1h. Representative samples from three replicates. Contraction values obtained

from Supplementary Videos 4, 6. **f**, Fascia biopsies treated with etoposide and immunolabelled for MKI67. **g**, Fraction of MKI67⁺ cells. Data are mean ± s.e.m.; *n* = 3 images analysed from 3 biological replicates. One-way ANOVA, Dunnett's multiple comparisons, 95% CI. **h, i**, Time-lapse images (**h**) and contraction rate (**i**) of neonate fascia biopsy in culture treated with 100 μM etoposide. Representative samples from three replicates. Contraction values obtained from Supplementary Videos 4, 7. **j**, Mean (± s.e.m.) matrix contraction velocity during the first 25 h of imaging; *n* = 25 values from Supplementary Video 7. Two-tailed Student's *t*-test, 95% CI. Lines show the distance between two tracked points in the SHG channel. Scale bars, 50 μm (**f**), 200 μm (**a, h**) and 500 μm (**d**).



Extended Data Fig. 10 | Fascia matrix steering precedes proliferation in vivo.

a, In situ fascia matrix labelling and EdU pulses. **b**, EdU detection in sections at defined time points. **c**, Fraction of EdU⁺ cells in the wound from total EdU⁺ cells. Data are mean \pm s.e.m.; $n=3$ (uninjured), 4 (3 dpw), 6 (7 dpw) and 4 (14 dpw)

images analysed from 3 biological replicates. One-way ANOVA, Tukey's multiple comparisons. Arrows indicate EdU-positive nuclei. Arrowheads indicate the original injury site. Broken and dotted lines delimit fascia and wounds respectively. Scale bars, 200 μ m.

Acknowledgements

This thesis would not be possible without the support of many individuals whom I would like to acknowledge.

I would like to express my sincere gratitude towards my mentor and direct supervisor **Dr. Yuval Rinkevich** for his continued motivation, guidance and support throughout my thesis and beyond. I extend my gratitude to my principal university advisor at the LMU medical faculty and head of CPC research school **PD Dr. Claudia Staab-Weijnitz** for her constant support with my thesis. I thank her and the whole research school team for providing invaluable education with a range of CPC research school training programs. I am grateful for **Prof. Dr. Magdalena Götz** for her support as an external expert in my Thesis Advisory Committee.

I would like to thank my CPC support crew and coffee buddies Tim, Vijay, Aydan, Ashesh, Ceylan, Shruthi, Andy, Haifeng, Valeria, Arunima, Ania, Mahesh, Johannes, Tankut and Michal who cushioned this journey on a daily basis. I express my sincere gratitude towards the entire past and present members of the Rinkevich lab for their professional support- Dongsheng, Simon, Juan, Adrian, Juliane, Qing, Li, Martin, Shaohua, Ruoxuan, Young, Jiakuan, Donovan, Bikram, Christoph and Maria. I am extremely grateful to Sandra for her constant mental support and tasks beyond her duty in managing my contracts and business trips.

I would like to extend my gratitude towards **Dr. Steffen Dietzel and team** for providing an uninterrupted access to a range of state of the art microscopes at the LMU Bio-imaging core facility. I am grateful for Dr. Gerald Burgstaller (CPC), Prof. Carsten Marr (ICB), Falco and Nicolas (Leica), Tamara and Sebastian (Arivis) and the entire Network of European Bioimage Analysis (NEUBIAS) team for providing meaningful trainings and inputs which enabled me to contribute for publications and thesis.

Beyond the lab, I am indebted to my friends and my extended family in Munich in keeping me sane - Shanshank, Suhas, Gautham, Akash, Shankar, Krishna, Prateek, Akshay, Sonal, Sharada, Ashwath and Priyamvadha. I am indebted to Kavyaa who has been with me through thick and thin throughout my thesis and way beyond.

Needless to say, I would like to thank my family Shobha (amma), Ramesh (appa), Sudhanva (anna), Swasthi (attige) and my little nieces Aarabhi and Swara for motivating me to pursue science, supporting my dreams, decisions, teaching me the ways and core values of life. Amma`s mental strength and endurance along with Appa`s support solely enabled me to focus on my thesis.

I dedicate my thesis to them.